Microstructural Characterization and Corrosion Behavior of Al 7075 Alloys Using X-ray Synchrotron Tomography

by

Sudhanshu Shekhar Singh

A Dissertation Presented in Partial Fulfillment
of the Requirements for the Degree
Doctor of Philosophy

Approved August 2015 by the
Graduate Supervisory Committee:

Nikhilesh Chawla, Chair
Terry Alford
Kiran Solanki
Jay Oswald

ARIZONA STATE UNIVERSITY

December 2015

ABSTRACT

Al 7075 alloys are used in a variety of structural applications, such as aircraft wings, automotive components, fuselage, spacecraft, missiles, etc. The mechanical and corrosion behavior of these alloys are dependent on their microstructure and the environment. Therefore, a comprehensive study on microstructural characterization and stress-environment interaction is necessary. Traditionally, 2D techniques have been used to characterize microstructure, which are inaccurate and inadequate since the research has shown that the results obtained in the bulk are different from those obtained on the surface. There now exist several techniques in 3D, which can be used to characterize the microstructure.

Al 7075 alloys contain second phase particles which can be classified as Fe-bearing inclusions, Si-bearing inclusions and precipitates. The variation in mechanical and corrosion properties of aluminum alloys has been attributed to the size, shape, distribution, corrosion properties and mechanical behavior of these precipitates and constituent particles. Therefore, in order to understand the performance of Al 7075 alloys, it is critical to investigate the size and distribution of inclusions and precipitates in the alloys along with their mechanical properties, such as Young's modulus, hardness and stress-strain behavior. X-ray tomography and FIB tomography were used to visualize and quantify the microstructure of constituent particles (inclusions) and precipitates, respectively. Microscale mechanical characterization techniques, such as nanoindentation and micropillar compression, were used to obtain mechanical properties of inclusions.

Over the years, studies have used surface measurements to understand corrosion behavior of materials. More recently, *in situ* mechanical testing has become more

attractive and advantageous, as it enables visualization and quantification of microstructural changes as a function of time (4D). In this study, *in situ* X-ray synchrotron tomography was used to study the SCC behavior of Al 7075 alloys in moisture and deionized water. Furthermore, experiments were performed in EXCO solution to study the effect of applied stress on exfoliation behavior in 3D. Contrary to 2D measurements made at the surface which suggest non-uniform crack growth rates, three dimensional measurements of the crack length led to a much more accurate measurement of crack growth rates.

DEDICATION

I dedicate this dissertation to my parents for their continued support and encouragement throughout my life.

ACKNOWLEDGMENTS

I would like to thank my advisor, Prof. Nikhilesh Chawla, for his guidance, support, patience, and encouragement throughout my studies at ASU. I have been fortunate enough to have an advisor like him who has always trusted me and allowed me to work independently, improved my writing, has given me opportunities to substitute him for his classes, and much more. I wish that one day I can become as good an advisor to my students as Prof. Chawla has been to me.

I wish to thank the members of my dissertation committee: Prof. Terry Alford, Prof. Kiran Solanki, and Prof. Jay Oswald. A special thanks to Dr. Jason Williams who has constantly provided me with technical advice throughout my PhD and has helped me in designing experiments. I am grateful for financial support from the Office of Naval Research (Dr. A. K. Vasudevan and Dr. W. Mullins, program nanagers, Contract No. N00014-10-1-0350) to carry out this research work. I gratefully acknowledge the use of facilities within the Center for Solid State Science at Arizona State University. I would also like to thank Dr. F. De Carlo and Dr. X. Xiao at Argonne National Laboratory for assistance with X-ray synchrotron tomography to perform this work. Use of the Advanced Photon Source was supported by the U.S. Department of Energy, Office of Science, Office of Basic Energy Sciences, under Contract No. DE-AC02-06CH11357. Finally, I would also like to thank:

- Members of Chawla Research Group for their useful suggestions and providing a friendly and collegial environment in the lab.

- All my friends especially Dr. Nilesh Badwe, Mrs. Priyanka Bagade, Dr. Somilkumar Rathi, Dr. Mehul Bhatia, Dr. Ilaksh Adlakha, and Mr. Vipin Agrawal for their constant support.
- My family for their wonderful encouragement.

TABLE OF CONTENTS

Page

LIST OF TABLES

LIST OF FIGURES

Figure Page

Figure Page

Figure Page

Figure Page

Figure Page

Figure Page

Figure Page

CHAPTER 1

INTRODUCTION

Structural metallic materials are routinely subjected to mechanical stresses and strains in a variety of environments. Such materials possess complex microstructures spanning a wide spectrum of length scales, which determine their macroscopic properties and performance. The growing demands in global sustainability, national security, and energy have raised great challenges in the development of these materials that can achieve optimal performance under extreme conditions. 7075 Aluminum alloys, in particular, are used in a variety of structural applications, such as automotive components, aircraft wings, fuselage, spacecraft, missiles, etc. (Starke and Staley 1996; Bucci, Warren, and Starke 2000). These alloys are often subjected to stress in aggressive corrosive environments, e.g., salt water and moisture. The mechanical and corrosion behavior of 7075 aluminum alloys is controlled by a variety of factors, such as microstructure, and environment (Speidel 1975; Holroyd and Scamans 2011; Suresh 1998; Bonakdar et al. 2012; Birbilis and Buchheit 2008a) etc. Thus, a comprehensive understanding of the microstructure, along with combined effects of stress and the environment, is necessary.

Traditionally, the study of material structure has been limited by two dimensional (2D) imaging techniques. This approach is often inaccurate or inadequate for solving many cutting-edge problems. It is also often laborious and time-consuming. Advances in experimental methods, analytical techniques, and computational approaches, have now enabled the development of three dimensional (3D) analyses. The study of 3D microstructures under an external stimulus (e.g., stress, temperature, environment) as a

function of time (4D) is particularly exciting. X-ray tomography is an excellent imaging technique that eliminates the need for cross-sectioning and allows for superior spatial and temporal resolutions with minimal sample preparation (Salvo et al. 2003; Eric Maire et al. 2001; Buffiere et al. 2010). 3D visualization and quantification of heterogeneous microstructures by X-ray tomography has been successfully performed in metal matrix composites (Laurent Babout et al. 2001; Hruby et al. 2014; E. Maire et al. 2001), Sn-rich alloys (Padilla et al. 2012; Ling Jiang et al. 2011), and aluminum alloys (Knight, Salagaras, and Trueman 2011; Ludwig et al. 2003; Terzi et al., others 2009).

The microstructure of 7075 aluminum alloys contain second phase particles, such as inclusions and precipitates (Starke and Staley 1996). The variation in mechanical and corrosion properties of aluminum alloys have been attributed to the size, shape, distribution, corrosion potential and mechanical properties of precipitates and constituent particles (Goswami et al. 2013; Birbilis and Buchheit 2008a; Birbilis and Buchheit 2008b; V. K. Gupta and Agnew 2011; Patton et al. 1998; Bozek et al., others 2008). Therefore, in order to understand the mechanical and corrosion behavior of Al 7075 alloys, it is critical to investigate the size and distribution of inclusions and precipitates along with their mechanical properties, such as Young's modulus, hardness and stress-strain behavior. Nanoindentation and micropillar compression can be used to obtain mechanical properties of microstructural constituents. X-ray tomography and FIB tomography can be used to obtain microstructure of constituent particles and precipitates, respectively.

It is well known that 7075 aluminum alloys are susceptible to corrosion in moisture and liquid environments (water, NaCl, EXCO solution etc.) and show stress

corrosion cracking (SCC), fatigue corrosion and exfoliation corrosion behavior. Till now, most of the studies aimed at understanding the underlying mechanisms involved in these phenomena have been performed in 2D. As we understand that the corrosion and cracking is actually a 3D process, it is required to perform experiments using 3D techniques, such as X-ray synchrotron tomography. Moreover, the experiments should be performed *in situ* to obtain the change in microstructure with time (4D).

This dissertation focuses on the use of X-ray synchrotron tomography to characterize the microstructure and understand the mechanical or corrosion properties of 7075 aluminum alloys in 3D/4D. Visualization and quantification of second phase particles along with their mechanical properties will be instrumental in understanding the bulk deformation behavior of these materials. The use of *in situ* X-ray synchrotron tomography provides a new insight in understanding SCC, fatigue corrosion, exfoliation corrosion behavior of aluminum alloys.

.

CHAPTER 2

LITERATURE REVIEW

2.1 Aluminum Alloys

Aluminum alloys are used in structural applications due to their high strength to weight ratio. Pure aluminum has very low strength and therefore alloying elements are added to it to increase its strength. The main alloying elements in aluminum are copper (Cu), zinc (Zn), magnesium (Mg), manganese (Mn), and silicon (Si). Depending upon the alloying content, the wrought aluminum alloys are divided into 1xxx (no alloying elements), 2xxx (Al-Cu-Mg), 3xxx (Al-Mn), 4xxx (Al-Si), 5xxx (Al-Mg), 6xxx (Al-Mg-Si), and 7xxx (Al-Zn-Mg-Cu). Among them, 2xxx, 6xxx and 7xxx are heat treatable alloys and others are non-heat treatable alloys. Strengthening in 7075 aluminum alloys comes from precipitation hardening where precipitates provide strength.

2.1.1 Second Phase Particles in 7075 Aluminum Alloys

Second phase particles in 7075 aluminum alloys can be divided into three categories (Starke and Staley 1996):

a) Constituent particles
b) Precipitates
c) Dispersoids

Constituent particles (also called inclusions) are formed from the impurities present in the alloys, primarily iron and silicon. These particles form during casting by liquid-solid eutectic reactions and do not dissolve in further thermomechanical

processing. Rolling and extrusion tend to break-up and align constituent particles into bands within the alloy (V. K. Gupta and Agnew 2011). Dispersoids are formed during ingot preheating by precipitation of the transition elements, such as chromium, manganese or zirconium. Dispersoids are formed by design to control grain structure and degree of recrystallization (Starke and Staley 1996). They remain stable after preheating of ingot unless heat treatment is performed well above the conventional solutionization temperature.

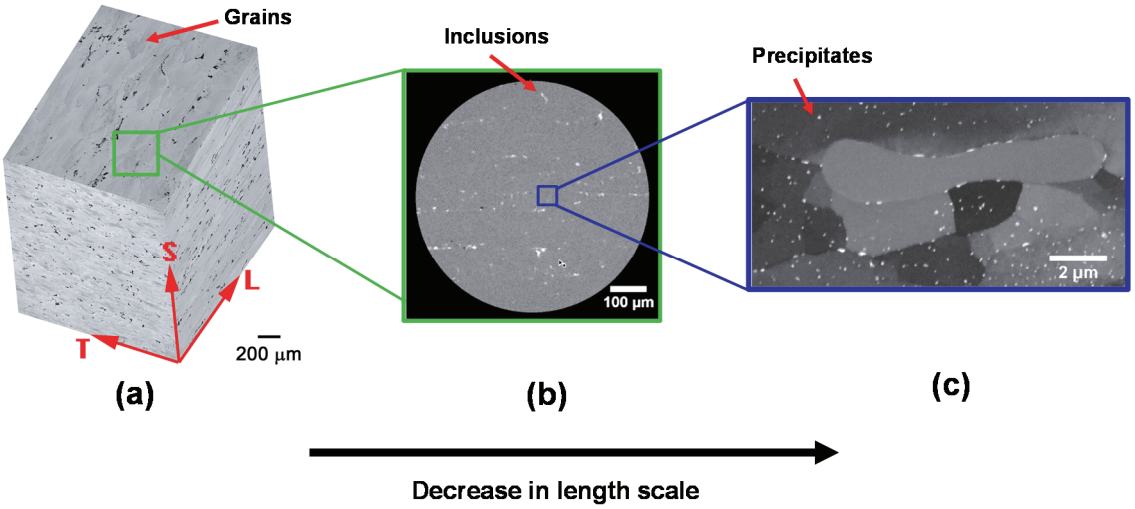

Figure 1. Microstructure of Al 7075 alloys in decreasing length scale (a) optical surface image showing grains, (b) X-ray tomography image (2D virtual slice of 3D volume) showing inclusions, and (c) grains and nanoscale precipitates visible in FIB-SEM slice

Nanoscale precipitates are formed when the alloy is either natural aged or artificially aged following solution heat treatment. The precipitation in AA7075 occurs in the following sequence: supersaturated solid solution → GP zones → η' → η (Viana et al. 1999; Garcia-Garcia et al. 2014). Figure 1 shows the microstructure of Al7075 alloys

with decreasing length scale. Figure 1a shows large elongated grains along the rolling direction (L). Figure 1b shows inclusions (white particles) and Figure 1c shows precipitates (small white particles) along with small recrystallized grains.

2.2 Microstructural Characterization of Second Phase Particles

Several studies have looked into the size distribution of second phase particles in two dimensions using SEM or optical microscopy. However, the microstructure in three dimensions (3D) would be completely different from the surface and therefore three dimensional (3D) techniques are required for microstructural characterization. Experimental techniques for 3D microstructural characterization include atom probe tomography (APT) (Miller and Kenik 2004), electron tomography (Midgley and Dunin-Borkowski 2009), serial sectioning using focused ion beam (FIB) (Bansal et al. 2006; D. R. P. Singh, Chawla, and Shen 2010; Yazzie et al. 2012), mechanical polishing followed by optical microscopy (Sidhu and Chawla 2004), and X-ray tomography (Stock 1999). Among them, X-ray tomography and FIB tomography have gained popularity in recent years since they provide a combination of optimum resolution and statistical information.

X-ray tomography follows Beer-Lambert law, which is given by (Yazzie et al. 2012):

$$I = I_0 e^{(-\mu/\rho)\rho x} \quad (1)$$

Where I_0 is the original intensity of X-rays from the source, I is the intensity of the beam when it has traveled a distance x into the material, μ is the attenuation coefficient, and ρ is the density of the material. The sample is rotated by an angle of 180^o or 360^o in an

increment of fixed predefined angle and for each angular increment an image (also called projection) of the object is obtained. These projections are then reconstructed using algorithms, such as filtered back projection algorithm, to obtain the 3D microstructure of the object. In FIB (focused ion beam) tomography, the sample is tilted by 52^{o} so that the surface of the sample is perpendicular to the Ga^{+} ions. The material is removed layer by layer using Ga^{+} ions and electron beam is used to obtain image of each layer after its removal, as shown in Figure 2. In this way, a stack of images is obtained in 3D, which can be analyzed using image analysis softwares.

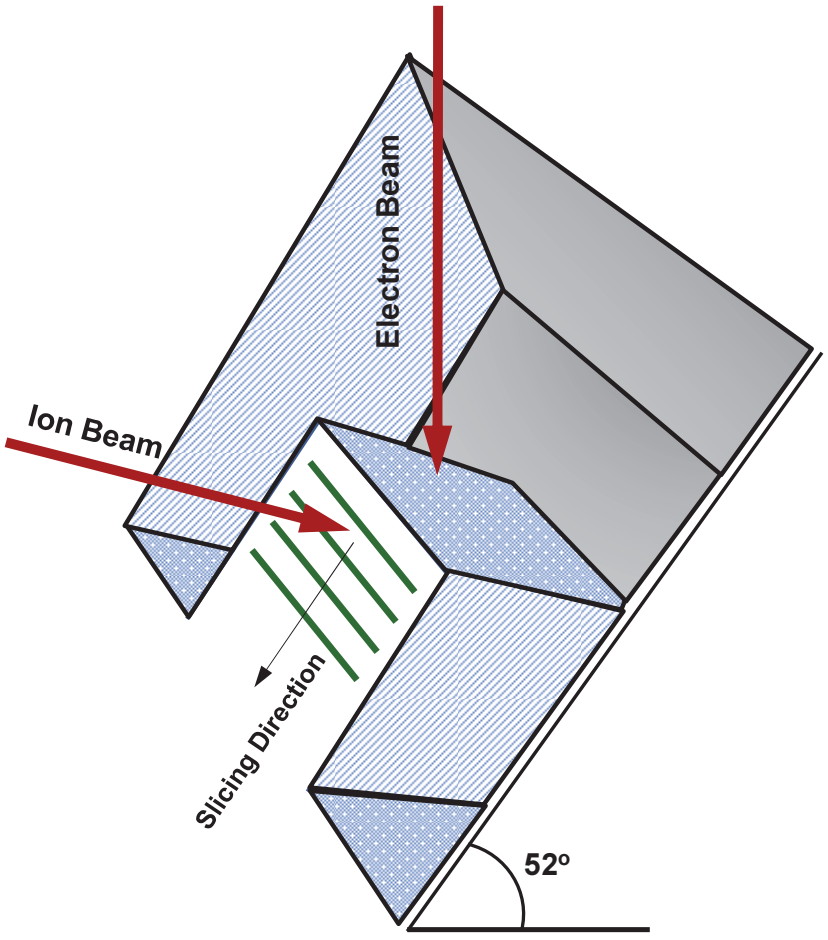

Figure 2. Schematic of FIB tomography

Very few studies have been performed to characterize the microstructure of constituent particles in three dimensions. Maire et al. used X-ray synchrotron tomography to observe the extent of particles breakage in Al-Mg alloys in different stage of rolling and were able to observe the reduction in size of the particles and an increase in number of porosity (Eric Maire et al. 2006). Using X-ray tomography, Kastner et al. were able to visualize different phases in several cast aluminum alloys (Kastner, Harrer, and Degischer 2011). In AA 5182, Moulin et al. analyzed breaking of Fe-rich particles statistically and by a mechanical FEA-based model. They were able to classify iron-rich particles based on their shape (Moulin et al. 2010). Several studies have been performed on size and distribution of precipitates in Al alloys (Garcia-Garcia et al. 2014; Goswami et al. 2013; Gjønnes and Simensen 1970; Ringer and Hono 2000). Till date, the characterization of precipitates in AA7075 has been performed only in two dimensions (2D). Most of the studies have used transmission electron microscope (TEM), which provides very high resolution images but lack in statistics, since very small area is considered.

2.3 Mechanical Properties of Second Phase Particles

Mechanical properties of microconstituents can be obtained using nanoindentation and micropillar compression. Many studies have been performed to obtain mechanical properties of microconstituents in different materials using nanoindentation (Xie and Chawla 2013; Dudek and Chawla 2010; Deng et al. 2004; Bozek et al., others 2008; Oswald 2003; Patton et al. 1998) and micropillar compression (L. Jiang and Chawla 2010; Guo, Xie, et al. 2014; Stewart et al. 2012; H. Ghassemi-Armaki et al. 2014; Ling

Jiang, Jiang, and Chawla 2012; J. J. Williams, Walters, et al. 2013; Okamoto et al. 2013; Okamoto et al. 2014).

Over the years, nanoindentation has emerged as an excellent technique to obtain mechanical properties at small length scale (X. Li and Bhushan 2002; Warren C. Oliver and Pharr 2004). Using this technique, one can measure the hardness and elastic modulus of a material from indentation load-displacement data obtained during one cycle of loading and unloading. The typical load-displacement curve obtained from nanoindentation is shown in Figure 3. The deformation during loading is assumed to be both elastic and plastic in nature; however, only elastic displacements are recovered during unloading. The stiffness (S) is given by slope of the unloading curve (dP/dh), i.e., S = dP/dh. Reduced modulus (E_r) and elastic modulus (E) of a material can be obtained from the following equations (Hay 2009):

$$E_r = \frac{\sqrt{\pi}}{2\beta}\frac{S}{\sqrt{A}} \tag{2}$$

$$\frac{1}{E_r} = \frac{1-\nu^2}{E} + \frac{1-\nu_i^2}{E_i} \tag{3}$$

Where E and υ are Young's modulus and Poisson's ratio of the material and E_i and υ_i are for the indenter. A is the contact area and β is the indenter geometry factor. Hardness (H) is calculated as the ratio of load to contact area, i.e., H = P/A, where P is the load at maximum displacement.

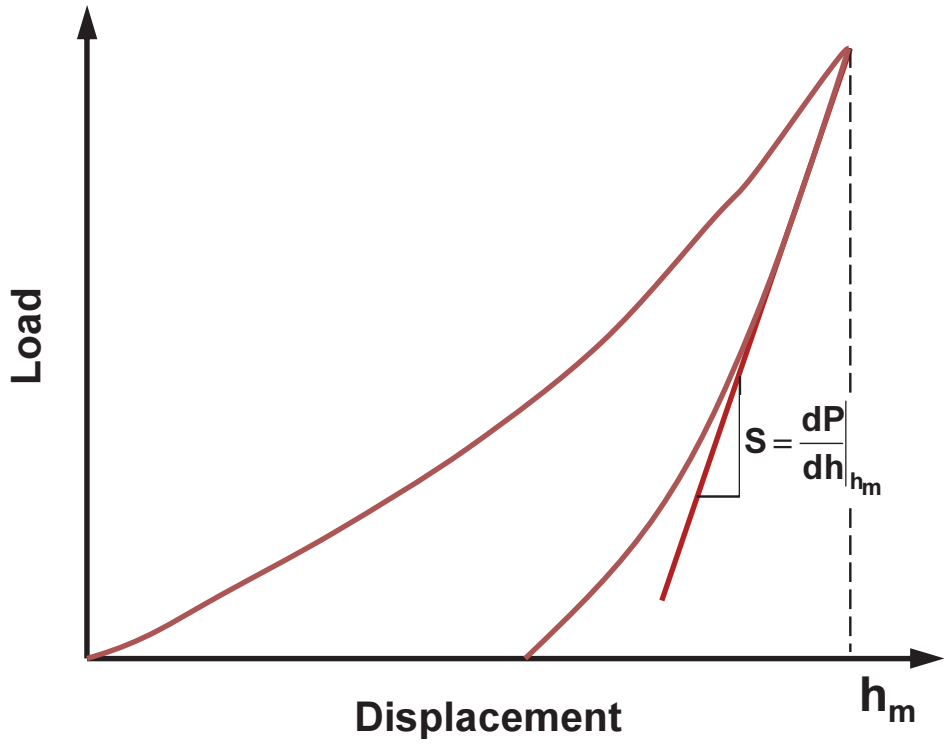

Figure 3. Typical load-displacement curve obtained from nanoindentation

Recently, CSM (continuous stiffness measurement) has emerged as a better technique than the method mentioned above. In CSM technique, along with the applied load, an oscillating force with a small amplitude (significantly smaller than the nominal load) is concurrently superimposed, as shown in Figure 4. Using a frequency-specific amplifier, an accurate measurement of contact stiffness at all indentation depths is provided by separating the in-phase and out-of-phase components of the load-displacement data (Hay, Agee, and Herbert 2010; X. Li and Bhushan 2002). The advantage of CSM over the common Oliver and Pharr's method is that the modulus and hardness can be obtained with displacement and therefore multiple indentations are not required. The contact stiffness in the case of CSM is given by:

$$S = \left[\left(\frac{1}{\frac{F_o}{z_o}cos\phi - (K_s - m\omega^2)}\right) - \left(\frac{1}{K_f}\right)\right]^{-1} \quad (4)$$

Where, F_o is force amplitude, h_o is displacement amplitude, ω is the frequency of oscillation, Φ is the phase angle between displacement and the force, K_f is the frame stiffness, K_s is the spring constant of leaf springs supporting the indenter, and m is the mass of the indenter. The values of the force amplitude, displacement amplitude and phase angle are continuously measured and then contact stiffness is calculated. From the contact stiffness values, the reduced modulus and the Young's modulus can be obtained from equations 2 and 3.

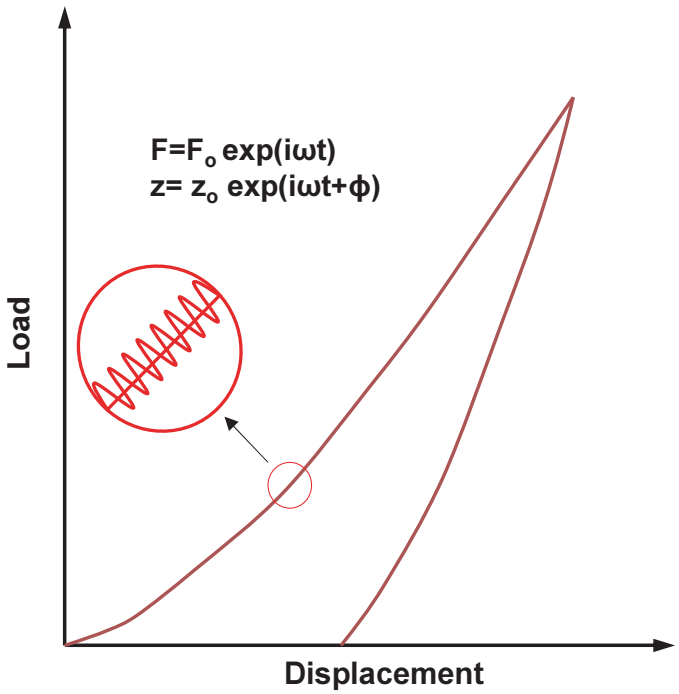

Figure 4. Schematic of CSM technique. A small harmonic load is superimposed (X. Li and Bhushan 2002)

Although, nanoindentation is an excellent technique, it can only provide elastic modulus and hardness of the materials and doesn't provide information on the stress-strain behavior of the materials. With focused ion beam (FIB) technology becoming more widely available, pillar compression is becoming an increasingly popular technique to understand deformation behavior at small length scale (Uchic, Shade, and Dimiduk 2009a; Greer, Oliver, and Nix 2005; Dubach et al. 2009; Howie, Korte, and Clegg 2012; Shin et al. 2012). In micropillar compression technique, small pillars are fabricated using FIB and then compressed in a nanoindenter using a flat punch, as shown in Figure 5. Although sample preparation time is a concern, pillar compression is superior to nanoindentation in that the stress state is uniaxial and provides stress-strain curves, similar to bulk compression tests.

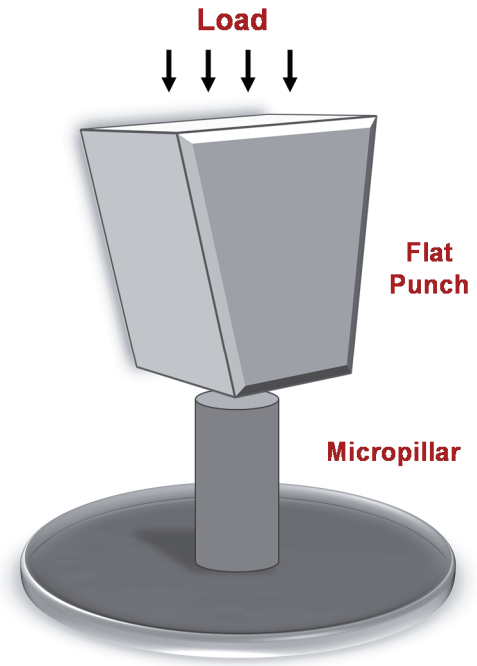

Figure 5. Schematic showing the compression of a pillar

Several studies have been performed to obtained mechanical properties of constituent particles using nanoindentation (Bozek et al., others 2008; Oswald 2003; Patton et al. 1998), however, no study has been performed to obtain stress-strain behavior. The modulus and hardness values of these studies show a great deal of variability, with modulus values ranging between 130-169 GPa for Fe-bearing inclusions and 44–97 GPa for Si-bearing inclusions. Patton et al. (Patton et al. 1998) reported the modulus values of 132-167 GPa for Al_7Cu_2Fe and 82.3-99.4 GPa for Mg_2Si. Oswald (Oswald 2003) reported mean modulus value of 133.6 GPa for Fe-bearing inclusions and 50.1 GPa for Si-bearing inclusions, whereas Bozek et al. (Bozek et al., others 2008) reported a mean value of 160.9 GPa for Fe-bearing inclusion. Therefore, it is necessary to obtain the accurate Young's modulus values, along with the stress-strain behavior of these inclusions, to better understand and model their effect on the damage behavior of aluminum 7075 alloys.

2.4 Corrosion Behavior of 7075 Aluminum Alloys

Several studies have been performed to understand the mechanisms of stress corrosion cracking (SCC) in aluminum alloys. Basically, two mechanisms have been proposed for 7075 aluminum alloys:

1) Anodic dissolution
2) Hydrogen embrittlement

Probably, anodic dissolution mechanism was first explained by Dix in 1940 (Dix 1940). In 7075 aluminum alloys, the precipitates at the grain boundaries are anodic with respect to the alloy matrix which leads to the localized corrosion along grain boundaries.

These anodic precipitates dissolve rapidly in presence of the corrosive fluid which result in intergranular crack propagation, until passivation occurs. The stress field at the crack tip results in rupture of the passive film. Rupturing of passive film again exposes the anodic precipitates to the corrosive fluid and crack continues to propagate (Braun 2007). The mechanism of anodic dissolution is illustrated in Figure 6.

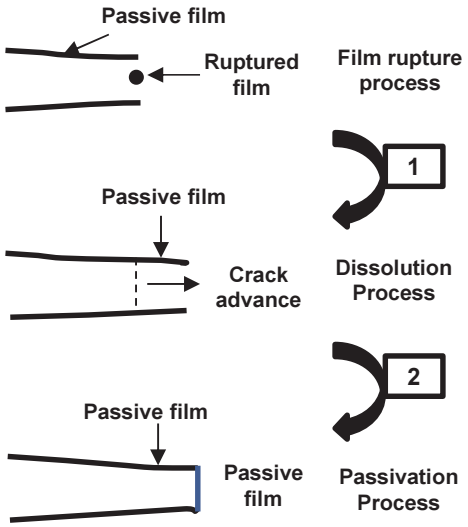

Figure 6. Anodic dissolution mechanism for stress corrosion cracking (Braun 2007)

The presence of hydrogen in aluminum alloys also results in premature failure of the alloys. Hydrogen embrittlement mechanisms can be broadly classified into three categories: (a) hydrogen-enhanced decohesion (HEDE) mechanism (Oriani 1972; Hänninen 2003), (b) hydrogen-enhanced localized plasticity (HELP) mechanism (Birnbaum and Sofronis 1994; Robertson 2001), and (c) adsorption-induced dislocation-emission (AIDE) mechanism (Lynch 2013; Lynch 1988). The steps for hydrogen embrittlement is illustrated in Figure 7. HEDE mechanism is based on the presence of

hydrogen at or ahead of the crack tip that leads to weakening of the interatomic forces and easier crack propagation. In the HELP mechanism, dislocation activity is increased due to the presence of hydrogen, which shields the elastic interaction between dislocations. Finally, AIDE is attributed to dislocation emission due to weakening of metal-metal bonds by H atoms adsorbed at the crack tip. It appears that different mechanisms are predominant depending on the combinations of microstructure, stress, and environment.

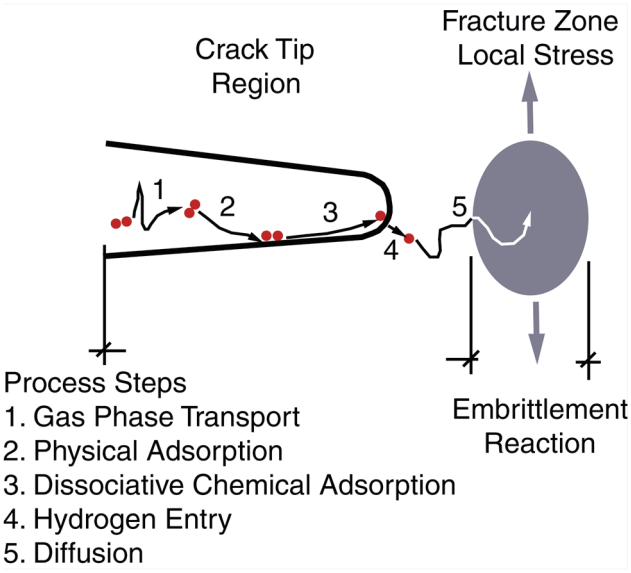

Figure 7. Steps for Hydrogen embrittlement mechanisms

During crack propagation stage, the stress corrosion cracking rate can be divided into three regions (region I, II and III), as shown in Figure 8 (Speidel 1975). K_{ISCC} is defined as threshold stress intensity factor below which crack growth is very slow to be visible. When the stress intensity is higher than the threshold value, the crack growth rate depends upon both the stress intensity factor and the environment. In stage I, crack growth rate has large stress intensity dependence and can be approximated by an

exponential function. In stage II, the crack growth rate remains approximately same (also called “plateau”) and is independent of the applied stress intensity factor. There are many other factors that can affect this “plateau” crack propagation rate, such as loading mode (Mode I or Mode III), chemistry of the corrosive solution, electrochemical potential, and relative humidity (J. Gao 2011). At very high stress intensity values, such as in stage III, the crack growth rate is again stress intensity dependent and cracking is more related to mechanical fracture.

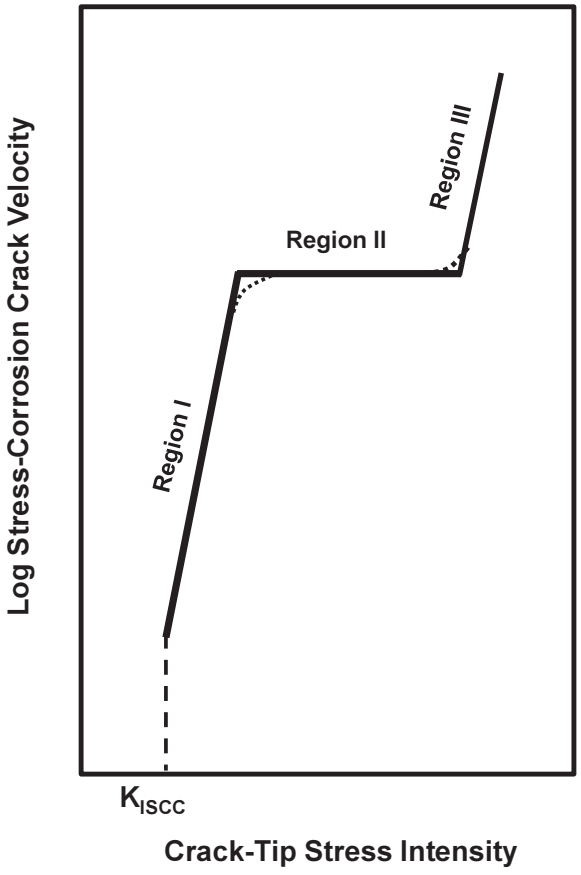

Figure 8. Stages of crack growth rates in SCC (Speidel 1975)

SCC of aluminum alloys has been studied for decades; however, most of the studies have been performed in 2D. Studies on the use of X-ray tomography to understand the stress corrosion cracking behavior started very recently. Probably, the first study was performed by Connolly et al. in 2006 and they were able to capture stress corrosion cracks using X-ray tomography (B. J. Connolly et al., others 2006). Marrow et al. provided evidence for bridging ligaments in sensitized 302 stainless steel (Marrow et al. 2006; Marrow et al. 2004). Later, Horner et al. showed the evolution of stress corrosion cracks from corrosion pits in turbine disc steels (Horner et al. 2011).

Discontinuous surface cracks have been observed during stress corrosion cracking of aluminum alloys (J. Zhang et al. 2011) and steel (Masuda 2007; Qiao et al. 2011). Figures 9a (our study) and 9b (J. Zhang et al. 2011) show the discontinuous cracks on the surface of aluminum alloys in moisture and NaCl environments, respectively. It was postulated that a new crack nucleates in front of the main crack and then combines with the main cracks. However, no studies have been performed to confirm this. Moreover, the measurement of crack length becomes difficult due to discontinuities in their growth and therefore might lead to a significant error in crack growth rate measurements using 2D studies.

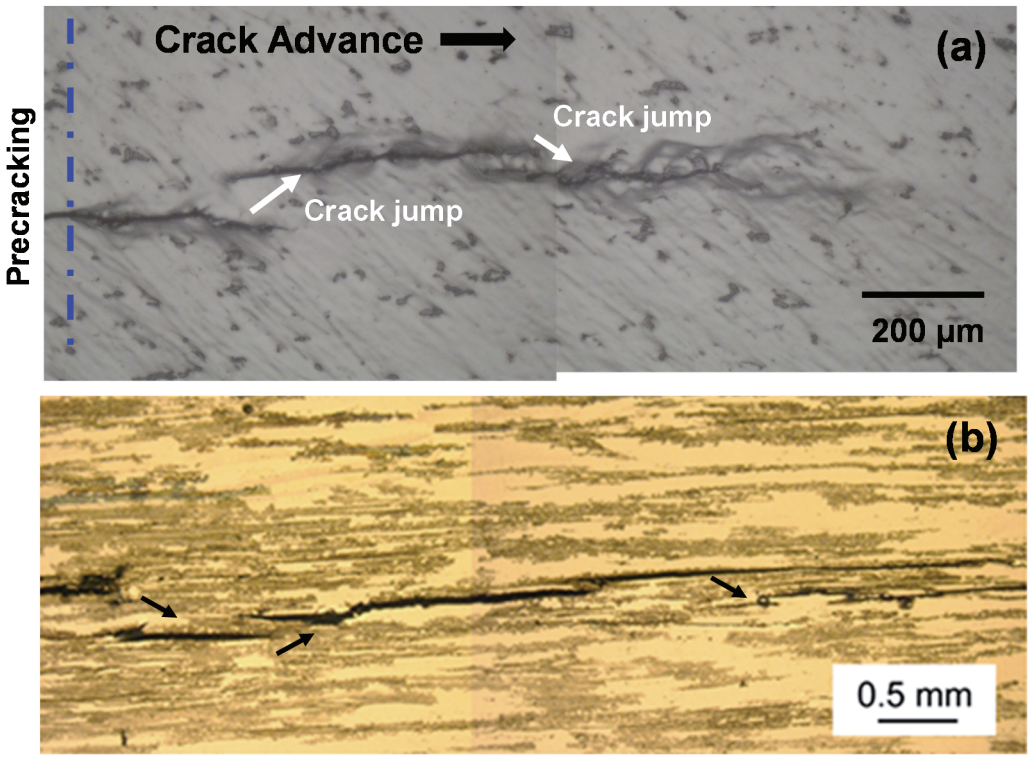

Figure 9. Discontinuous cracks (crack jumps) observed in aluminum alloys (a) in moisture (our study), and (b) in NaCl solution (J. Zhang et al. 2011)

Corrosion rates can be measured by weight loss measurement, hydrogen evolution technique, optical measurement, Tafel extrapolation of polarization curves, and electrochemical impedance spectroscopy (Davis 1999; Ezuber, El-Houd, and El-Shawesh 2008; Shi, Liu, and Atrens 2010; Hassan and Zaafarany 2013; Atrens et al. 2013). All of these methods are either 2D in nature or provide bulk measurement of corrosion. Very few studies have been performed to measure localized corrosion rates (Knight, Salagaras, and Trueman 2011; Knight et al. 2010; X. Liu et al. 2006) using X-ray tomography. Hydrogen evolution technique can provide information on corrosion rate by measuring the volume of evolved hydrogen gasses; however, the measured corrosion rate would be related to bulk. The constituent particles present in 7075 aluminum alloys show different

electrochemistry behavior than the matrix and can be either cathodic or anodic with respect to the matrix (Birbilis and Buchheit 2008b; Birbilis et al. 2005). If the particles are cathodic with respect to the matrix, such as Fe-bearing particles, the matrix around the particles dissolves (also called "trenching"), as shown in Figure 10a. In contrast, anodic particles tend to dissolve in the solution, such as Mg_2Si. It has been shown that magnesium preferentially dissolves in the solution (similar to dealloying process), as shown in Figure 10b. Both these phenomena lead to the formation of pits and thereby release hydrogen gases in neutral and acidic medium as part of cathodic reactions. Continuous measurement (4D) of these hydrogen gasses can provide the information about localized corrosion rate.

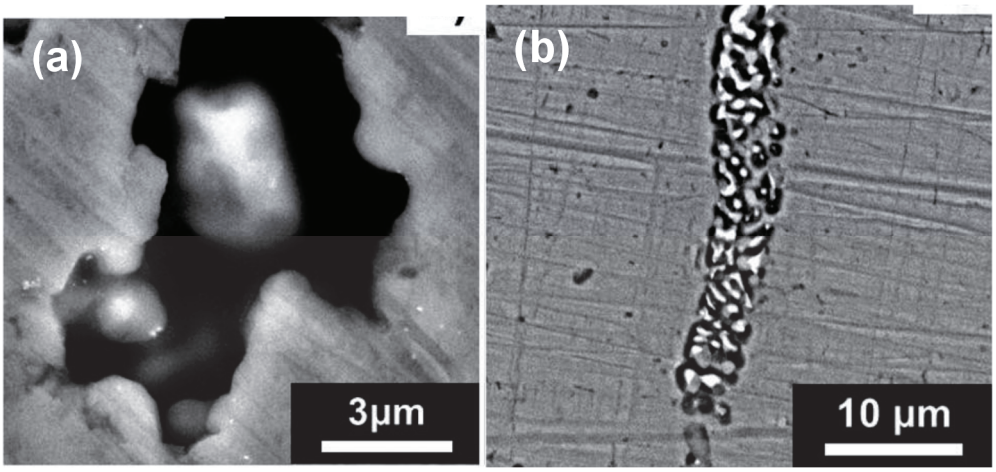

Figure 10. (a) Trenching around Fe-bearing particles, and (b) dealloying of Mg_2Si particles (R. K. Gupta et al. 2012)

Under very aggressive environments, such as the EXCO solution, exfoliation corrosion has been observed. Over the years, exfoliation corrosion has been studied using different techniques, such as immersion test (Robinson and Jackson 1999),

electrochemical impedance spectroscopy (EIS) (Keddam et al. 1997), and electrochemical transients (Marlaud et al. 2011). All these techniques were coupled with optical microscopy/SEM to understand the mechanisms of exfoliation. These techniques are either 2D in nature (immersion tests, optical/SEM) or provide bulk information of corrosion leading to speculation of the exact exfoliation corrosion mechanisms. To date, anodic dissolution of the precipitates along the grain boundaries has been thought to be the main mechanism of exfoliation corrosion (Robinson and Jackson 1999; McNaughtan, Worsfold, and Robinson 2003). According to this mechanism, the corrosion along the grain boundary (intergranular corrosion) leads to the formation of corrosion products of higher specific volume, which in turns generate large compressive stresses and lift the surface grains out from the alloy. SCC and exfoliation corrosion have been considered related to each other, with exfoliation corrosion propagating through intergranular stress corrosion cracking (McNaughtan, Worsfold, and Robinson 2003). However, recently exfoliation corrosion was proposed as an outcome of hydrogen embrittlement with volumetric effects of corrosion product playing a minor role (Marlaud et al. 2011). It was postulated that segregated hydrogen at or close to grain boundaries recombine and generate enough pressure to cause grain boundary fracture. Recently, X-ray tomography in Al-Mg-Si alloy (Eckermann et al. 2008) has shown that exfoliation corrosion is not necessarily intergranular in nature and also the role of constituent particles is not significant in initiation; in contradiction with other studies (Andreatta, Terryn, and De Wit 2004). The mechanisms of initiation and subsequent propagation of exfoliation corrosion are not really well-defined and need further investigation. Moreover, the effect of stress (both cyclic and static) is also not clear. The synergy between stress and

exfoliation is quite interesting since it provides an insight into the combined effects of exfoliation and SCC mechanisms.

Based on the literature review, the objectives of the research are:

1) Perform three dimensional (3D) visualization and quantification of second phase particles (mainly inclusions and precipitates) in Al 7075 using X-ray tomography and FIB tomography (Chapter 3 and Chapter 5).
2) Obtain mechanical properties of inclusions (constituent particles) using nanoindentation and micropillar compression. Nanoindentation is to be used to obtain Young's modulus and hardness. Micropillar compression will be used to obtain stress-strain curves (Chapter 3 and Chapter 4).
3) Using *in situ* X-ray synchrotron tomography, study the three dimensional crack growth behavior of Al alloys in SCC with time (4D). Understand the reasons behind the discontinuous surface cracks and then compare the 3D crack growth rates to that of 2D crack growth rates (Chapter 6).
4) Design experiments to perform *in situ* testing in liquid environments using X-ray synchrotron tomography. Study the effect of inclusions on the initiation of exfoliation corrosion of 7075 aluminum alloys. Study the effect of load (both static and cyclic) on the exfoliation corrosion behavior of 7075 aluminum alloys in 3D. Measure the localized corrosion rates by measuring the volume of hydrogen bubbles (Chapter 7).

CHAPTER 3

3D MICROSTRUCTURAL CHARACTERIZATION AND MECHANICAL PROPERTIES OF CONSTITUENT PARTICLES IN AL 7075 ALLOYS USING X-RAY SYNCHROTRON TOMOGRAPHY AND NANOINDENTATION

3.1 Introduction

7075 aluminum alloys are used extensively due to their high strength-to-weight ratio (AlHazaa, Khan, and Haq 2010), (Cepeda-Jiménez et al. 2011). 7075 aluminum alloys contain Fe-bearing and Si-bearing inclusions, also known as constituent particles (Payne et al. 2010; Xue et al. 2007; M. Gao, Feng, and Wei 1998). The origin of such inclusions is largely from impurities formed during the manufacturing process. These particles are formed during the initial casting and do not get dissolved during subsequent thermo-mechanical processing. Mechanical processing, such as rolling and extrusion, tends to break-up and re-distribute these constituent particles (Starke and Staley 1996; V. K. Gupta and Agnew 2011).

The inclusions can be particularly detrimental from a fatigue standpoint since small fatigue cracks in high strength aluminum alloys have been observed to initiate from these particles (V. K. Gupta and Agnew 2011; J.C. Grosskreutz, G.G. Shaw 1969; Pearson 1975; Weiland et al. 2009). Pile-up of dislocations in slip-bands that impinge upon constituent particle interfaces, can lead to initiation and growth of small cracks (V. K. Gupta and Agnew 2011). These cracks initiate either by debonding of the interface between the matrix and inclusions (J.C. Grosskreutz, G.G. Shaw 1969) or by fracture of

the inclusions themselves (Payne et al. 2010; Pearson 1975). Therefore, in order to understand the fatigue performance of Al 7075 alloys, it is critical to investigate the size and distribution of inclusions and porosity in the material along with their mechanical properties, such as Young's modulus and hardness.

X-ray tomography is an excellent imaging technique that eliminates the need for cross sectioning and allows for superior resolution and image quality with minimal sample preparation. 3D visualization and quantification of heterogeneous microstructures by X-ray tomography has been successfully performed in metal matrix composites (de Andrade Silva et al. 2010; N. Chawla, Sidhu, and Ganesh 2006), Sn-rich alloys (Ling Jiang et al. 2011; Sidhu and Chawla 2006; Padilla et al. 2012), aluminum alloys (Parra-Denis, Ducottet, and Jeulin 2009; Kastner, Harrer, and Degischer 2011), and powder metallurgy steels (Nikhilesh Chawla et al. 2009). In addition to visualization, such microstructural data sets can be incorporated into finite element models to elucidate the effect of microstructure on bulk deformation behavior (Sidhu and Chawla 2006; Padilla et al. 2012; J. J. Williams et al. 2010; J. J. Williams et al. 2011). In order to perform microstructure-based modeling, one of the important inputs is Young's modulus of the microstructural constituents. Nanoindentation is a particularly attractive technique for extracting Young's moduli and hardness of these intermetallics because of the relatively small volume being tested (Deng et al. 2004; Dudek and Chawla 2010). Very few studies have focused on determination of the Young's modulus and hardness of these constituent particles. The limited data on these inclusions using nanoindentation show a great deal of variability, with modulus values ranging between 130-169 GPa for Fe-bearing inclusions and 44–97 GPa for Si-bearing inclusions (Bozek et al., others 2008; Patton et al. 1998;

Oswald 2003). Thus, there is a pressing need to combine 3D microstructural data on size, morphology, and distribution of the inclusions, coupled with microscopic mechanical property data of the inclusions themselves.

In this work, we have obtained the 3D microstructure of Al 7075 alloys by X-ray synchrotron tomography. The volume, size, and distribution of pores, Fe-bearing and Si-bearing inclusions were visualized and quantified. Nanoindentation was used to accurately measure the Young's modulus and hardness of the constituent particles in the Al 7075 alloy. Knowledge of the individual mechanical properties of these constituent particles combined with the 3D microstructure, will allow us to better understand the overall mechanical performance of the alloys, and to more accurately model their behavior.

3.2 Materials and Experimental Procedure

The material used in this study was a commercially available 7075-T651 aluminum alloy rolled to a 2.5 cm thickness (Alcan rolled product, supplied by Dix Metals Inc). Specimens were polished to a 1 μm diamond finish and then to a final finish of 0.05 μm colloidal silica. Microstructural characterization was performed by scanning electron microscopy (SEM) (FEI-XL30). Energy dispersive spectroscopy (EDS) was used to obtain the composition of the inclusions and the matrix.

Specimens of 7075-T651 alloy were machined by electro discharge machining (EDM) to dimensions of 10 mm (along the longitudinal direction) x 1 mm (along transverse) x 0.7 mm (along short transverse) for 3D microstructural characterization using X-ray synchrotron tomography. In rolling technology of sheets and plates, the

longitudinal direction is referred as the rolling direction, the transverse direction is along the width of the sheets/plates, and the thickness is called the short transverse direction. X-ray tomography was performed at the 2-BM beamline of the Advanced Photon Source (APS) at Argonne National Laboratory. The details of the tomography system at 2-BM have been described elsewhere (J. J. Williams et al. 2010; De Carlo and Tieman 2004). The X-ray beam energy was approximately 24 keV. A 100 μm LuAG:Ce scintillator screen was used to convert the transmitted X-rays to visible light. This was coupled with an objective lens and a CoolSnap K4 CCD camera to achieve a specimen pixel size of about 0.74 μm. 2D projections were collected at angular increments of 0.125^{o} over a range of 180^{o}. These 2D projections were then reconstructed in 3D using Gridrec algorithm, which is based on Fast Fourier Transforms (FFT) method. It uses an innovative gridding technique to produce high-quality reconstructions. The details of the Gridrec algorithm can be found elsewhere (Marone and Stampanoni 2012; Dowd et al. 1999; Rivers 2012).

The stack of grayscale images were analyzed using conventional image analysis software (ImageJ, Bethesda, MD). For segmentation of the microconstituents, a large volume (592 μm x 690 μm x 370 μm) was cropped from the total scanned volume. The background noise in the images was removed using an anisotropic diffusion filter. The segmentation of the inclusions and the pores was performed using a combination of conventional thresholding (ImageJ, Bethesda, MD) and 3D region growing (MIMICS, Materialise, Ann Arbor, MI). The segmented images were imported into Avizo® Fire (VSG, Burlington, MA) for 3D reconstruction and visualization. Quantitative analysis of

the volume and size of the micro constituents was performed using the image processing toolbox in Matlab.

Nanoindentation was conducted on the inclusions, as well as on the 7075 matrix using a commercial nanoindenter (Nanoindenter XP-II, Agilent). The indentation experiments in the matrix were performed both on peak-aged (T651, PA) and over-aged (T73, OA) conditions. The heat treatment to obtain an over-aged microstructure is shown in Table 1. The specimens were polished to a 1 μm diamond finish and then to a final finish of 0.05 μm colloidal silica. Samples were mounted on aluminum stubs for nanoindentation testing using a mounting adhesive (Crystalbond^{TM}, West Chester, PA). The specimens were mounted at the flow temperature of the crystalbond (~ 135^{o}C) for a few seconds. This short duration of heating did not lead to any significant change in the microstructure of the matrix or inclusions. Nanoindentation was carried out on at least 30 inclusions for each type and matrix locations. To reduce the possible effect of the surrounding matrix on indentation of inclusions, large inclusions were selected and the center of each inclusion was indented. The nanoindenter was first calibrated by measuring Young's modulus and hardness of a silica standard. Tests were conducted in strain rate control with a strain rate target of 0.05 s^{-1}. A continuous stiffness measurement (CSM) technique was used during indentation, where a load is applied to the indenter tip to drive the indenter into the specimen surface while concurrently superimposing an oscillating force with a small amplitude (significantly smaller than the nominal load). An accurate measurement of contact stiffness at all indentation depths is provided by separating the in-phase and out-of-phase components of the load-displacement data (Fischer-Cripps 2004). The advantage of CSM is that an instantaneous measurement of

modulus and hardness can be obtained during indentation. Thus, multiple indentations at different depths are not necessary. Indentation was carried out using a Berkovich tip to a depth of 1000 nm per indentation. Young's modulus and hardness for an individual indentation were measured as the average value over a depth range where both modulus and hardness were independent of depth. SEM (scanning electron microscope) was used after the experiments to ensure that indentations were located well inside the inclusions and energy dispersive spectroscopy (EDS) was used to identify the composition of the inclusions.

Table 1. Heat treatment regimes to obtain Al 7075-T73 (OA)

	Solution Treatment	Quenching Medium	Aging condition
Over aged (T73)	475^{o}C for 2h	water	107^{o}C for 6 h 163^{o}C for 40 h

3.3 Results and Discussion

3.3.1 Scanning Electron Microscopy and Energy Dispersive Spectroscopy

Figure 11 shows the secondary electron and backscattered electron images of the 7075 alloys. Three types of inclusions were found: bright white (inside rectangle), gray (inside ellipse), and black (inside hexagon). These inclusions are clearly differentiated in the BSE image (Figure 11b) due to the difference in atomic number.

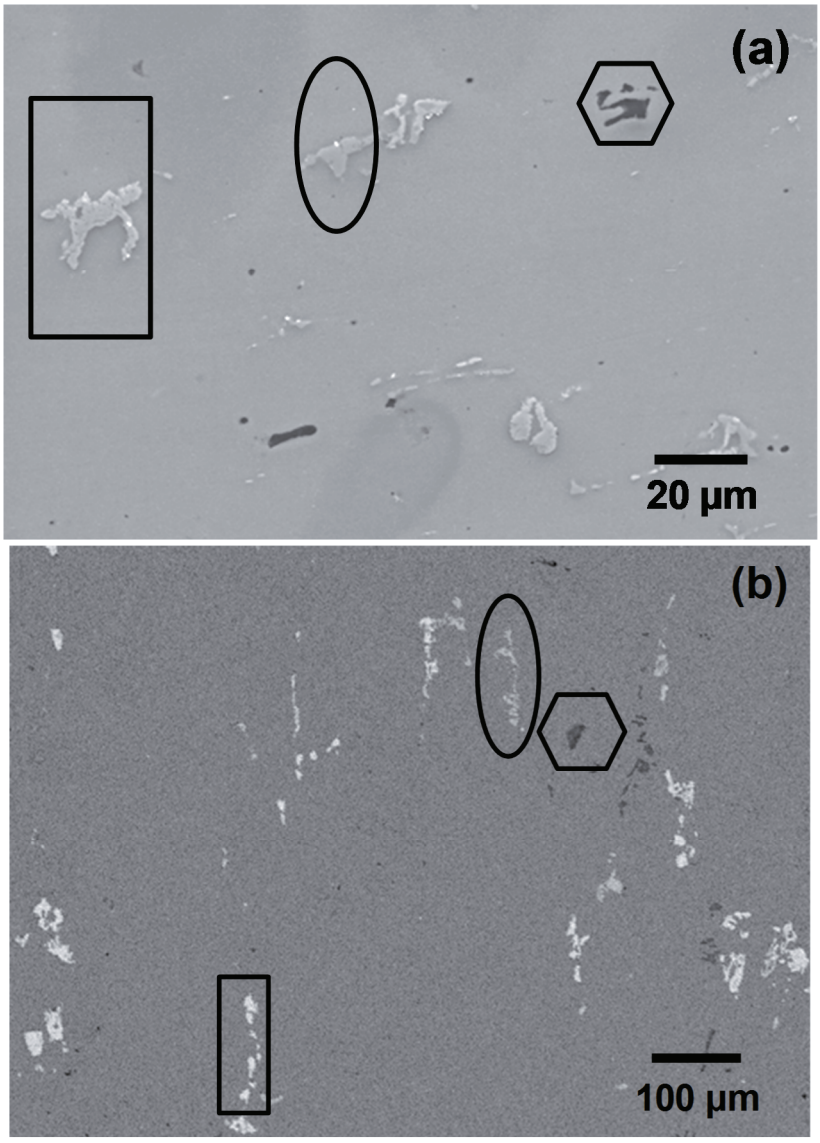

Figure 11. (a) Scanning electron micrograph, and (b) backscattered image of the microstructure. Different types of inclusions are marked: bright inclusions (inside rectangle), gray inclusions (inside ellipse), and dark inclusions (inside hexagon)

Energy Dispersive Spectroscopy (EDS) analysis of the sample was conducted, over a representative area (3-4 mm^2), to obtain chemical compositions of these inclusions and matrix as shown in Figure 12. The results of EDS analysis are summarized in Table 2.

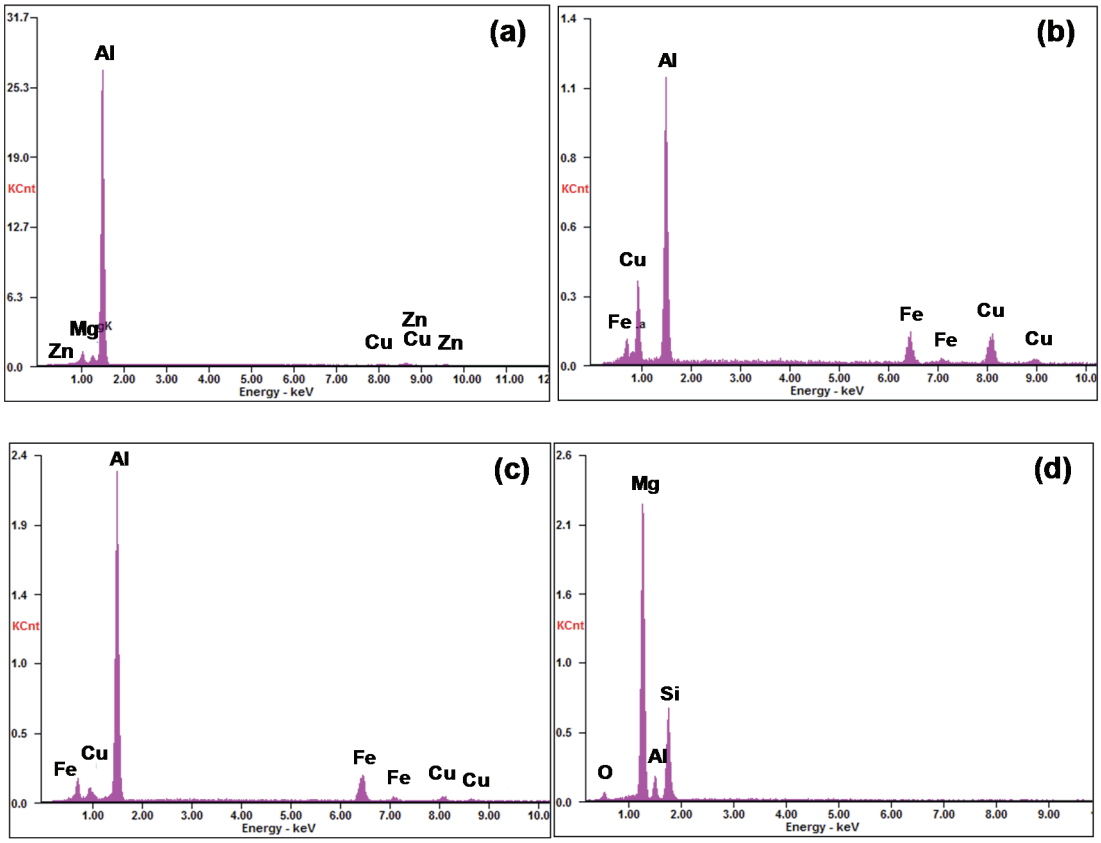

Figure 12. EDS spots scan results on (a) Al 7075 matrix, (b) bright white inclusions (Fe-bearing), (c) gray inclusions (Fe-bearing), and (d) black inclusions (Si-bearing inclusions)

It is usual to find the high values of standard deviation in the case of inclusions than that of the matrix since inclusions are formed from the impurities and the compositions may vary from one place to another. The bright white inclusions contain aluminum, copper, and iron as primary elements with an approximate atomic ratio of 7:2:1, indicating inclusions to likely be Al_7Cu_2Fe. The gray inclusions had an approximate atomic ratio of Al, Fe, and Cu as 23:4:1, indicating that these inclusions are most likely $Al_{23}Fe_4Cu$. Since both inclusions contain iron, these inclusions will be referred as Fe-bearing inclusions. The third type of inclusion had magnesium and silicon

as major elements with an approximate atomic ratio of 2:1, indicating that this is most probably Mg_2Si. These inclusions will be referred to as Si-bearing inclusions. These three types of inclusions have been reported previously for 7xxx alloys: Al_7Cu_2Fe (Payne et al. 2010; Xue et al. 2007; Starke and Staley 1996; V. K. Gupta and Agnew 2011; Bozek et al., others 2008; Patton et al. 1998; Oswald 2003), $Al_{23}Fe_4Cu$ (M. Gao, Feng, and Wei 1998; Yue et al. 2005), and Mg_2Si (Payne et al. 2010; Xue et al. 2007; Starke and Staley 1996; V. K. Gupta and Agnew 2011; Patton et al. 1998; Oswald 2003). The crystal structures of Mg_2Si, Al_7Cu_2Fe, and $Al_{23}Fe_4Cu$ are anti-fluorite type (Birbilis et al. 2005), tetragonal (Moulin et al. 2010), and orthorhombic (V. K. Gupta and Agnew 2011) respectively.

Table 2. EDS analysis of the matrix and inclusions in Al 7075 alloys

Al7075 Matrix		Bright inclusions		Gray inclusions		dark inclusions	
El.	at%	El.	at%	El.	at%	El.	at %
Al	93.7 ± 0.2	Al	71.6 ± 0.9	Al	82.8 ± 0.6	Mg	57.8 ± 5.6
Zn	2.5 ± 0.02	Cu	18.9 ± 0.9	Fe	13.6 ± 0.6	Si	29.6 ± 1.2
Mg	3.2 ± 0.2	Fe	9.5 ± 0.4	Cu	3.6 ± 0.2	O	8.0 ± 3.3
Cu	0.6 ± 0.02					Al	4.6 ± 3.5

3.3.2 X-ray Tomography

X-ray synchrotron tomography can show both absorption contrast and phase contrast (J. J. Williams et al. 2010). Absorption contrast exists when the attenuation of incident X-rays is proportional to mass density; and therefore, Fe-bearing inclusions (high mass density) appear bright and pores (low mass density) appear dark in the reconstructed images. Phase contrast occurs when X-rays are refracted by specimen interfaces. This changes the phase of the propagating wave, causing interference patterns between the incident and refracted waves (J. J. Williams et al. 2010). The proportion of phase contrast and absorption contrast depends upon the distance between the sample and the X-ray detector (e.g. scintillator), with smaller distances yielding less phase contrast relative to absorption contrast. A distance of 30 mm between the specimen and detector was used in this study. After an absorption-based reconstruction using Gridrec, microstructural features were distinguishable primarily through absorption contrast; however, near-field phase contrast fringes (mainly first order interference fringes) were also present at pore and inclusion surfaces.

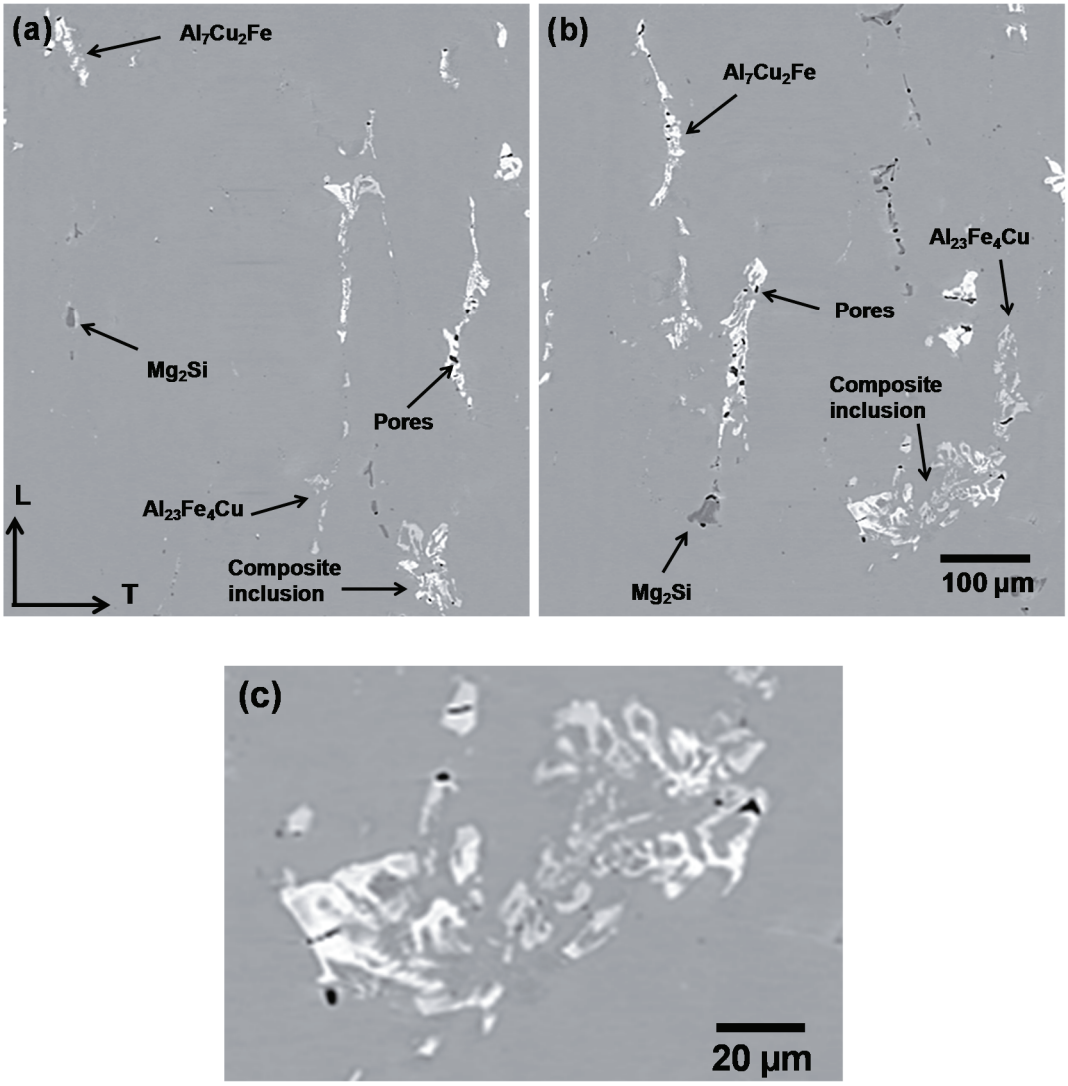

Figure 13. (a), (b) are 2D X-ray tomography slices showing Fe-bearing inclusions (Al_7Cu_2Fe, $Al_{23}Fe_4Cu$, and composite inclusion), Si-bearing inclusions (Mg_2Si), and pores, and (c) blown up of a composite inclusion from Fig. 13b

The 2D X-ray tomography slices after reconstruction are shown in Figures 13a and 13b. The microstructure consists of pores, Fe-bearing and Si-bearing inclusions. The pores are black, Al_7Cu_2Fe (bright white), $Al_{23}Fe_4Cu$ (light white) and Mg_2Si (gray). At some places, it is difficult to distinguish between Al_7Cu_2Fe and $Al_{23}Fe_4Cu$, because the two intermetallics are combined in a single particle, as shown in Figure 13a and 13b

(referred as composite inclusions). This can be clearly seen in Figure 13c, which shows a detailed view of one of the composite inclusions in Figure 13b.

Due to near-field phase contrast fringes, the gray values of the periphery of Fe-bearing inclusions had nearly the same gray value of Si-bearing inclusions, whereas the boundaries of the pores and Si-bearing inclusions had the same gray values as Fe-bearing inclusions, as shown in Figure 14. Therefore, selection of any of the microstructural constituents using conventional thresholding led to selection of unwanted shadows (fringes) at the boundaries of other constituents. To separate the microstructural constituents from unwanted boundaries, a 3D region growing segmentation technique was used (MIMICS, Materialise, Ann Arbor, MI) on the segmented black and white images. In the 3D region growing technique, a single pixel (or voxel) is selected within the inclusion in a 2D slice from the stack. The algorithm searches for voxels adjacent to that selected voxel of the same gray value. Additional adjacent voxels subsequently get selected until the entire volume of connected voxels is selected. The region growth stops when a voxel of different grey value (say the matrix) is reached. The result is the selection of a three dimensional object (in this case an inclusion) of voxels, each connected to another by a face, edge, or a corner. The schematic of a 3D region growing technique is shown in Figure 15.

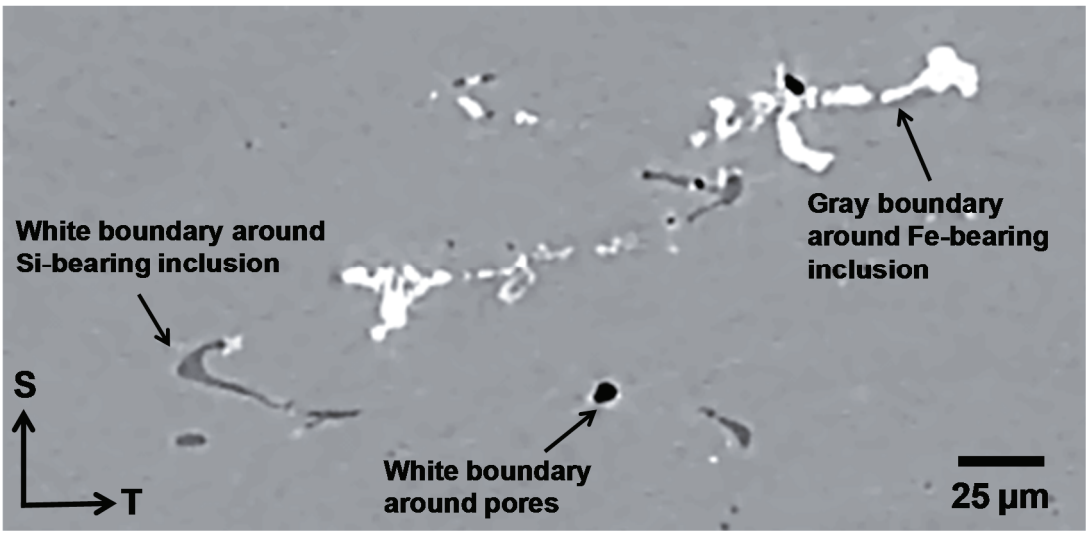

Figure 14. A 2D X-ray tomography slice showing the near-field phase contrast fringes. The periphery of the Si-bearing inclusions and pores are white (gray scale values nearly same as Fe-bearing inclusions), and Fe-bearing inclusions periphery have gray boundary (gray scale values nearly same as Si-bearing inclusions)

Figure 16 shows the steps involved in the segmentation process of Si-bearing inclusions. The steps involve conventional thresholding of inclusions in ImageJ, selection of inclusions using a 3D region growing technique in MIMICS and then final segmentation of particles in ImageJ. It can be seen that the unwanted boundaries (Figure 16b) around Fe-bearing inclusions due to thresholding of Si-bearing inclusions were not selected in the final segmentation (Figure 16d). The same steps were followed for the initial segmentation of Fe-bearing inclusions. To separate the different types of Fe-bearing inclusions (Al_7Cu_2Fe, $Al_{23}Fe_4Cu$ and composite inclusions) from the initial segmented images, a 3D region growing technique was again used as shown in Figure 17. Pores were segmented using conventional thresholding in ImageJ. The flow chart of the sequence of segmentation and volume rendering is shown in Figure 18.

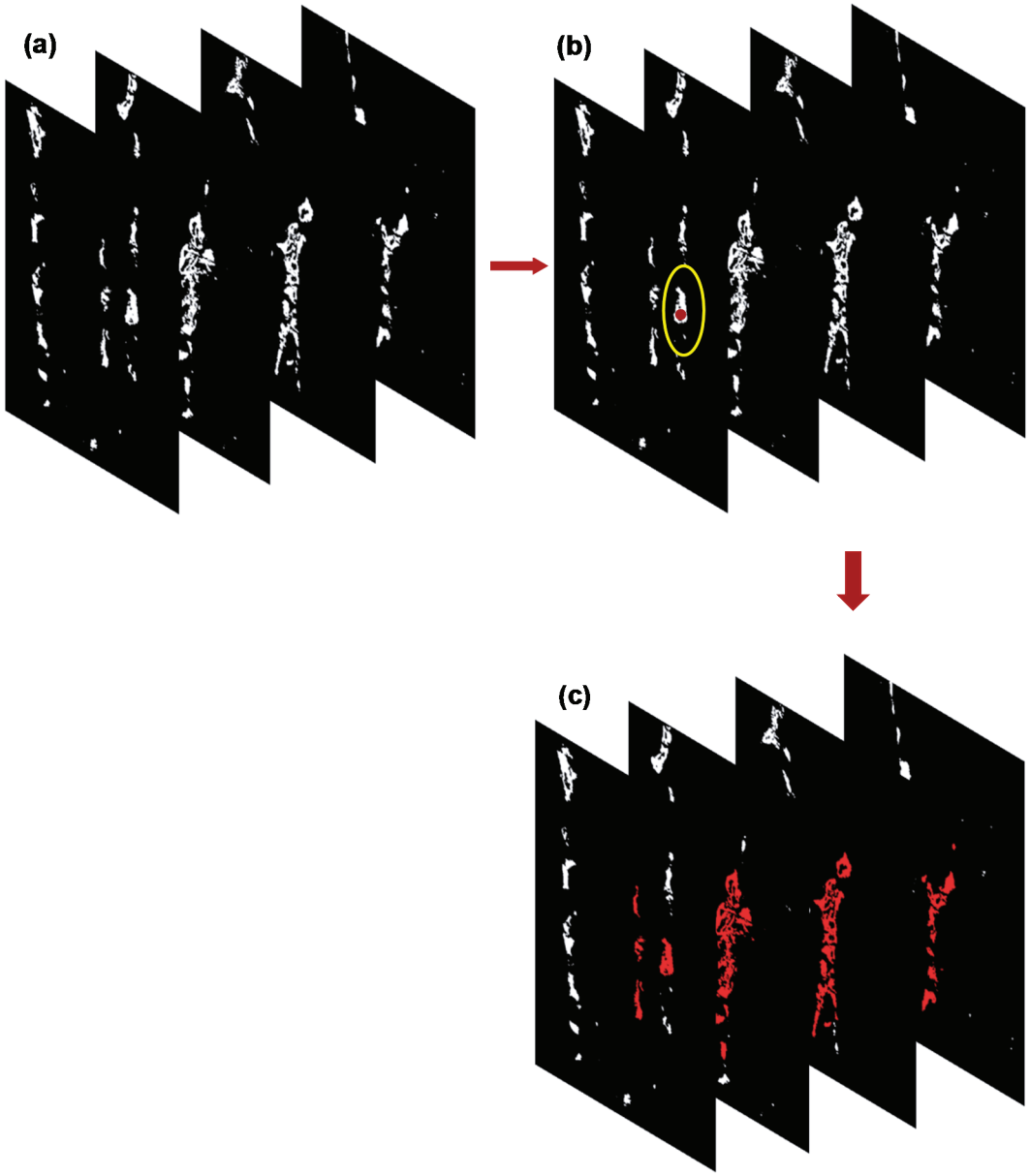

Figure 15. Schematic of a 3D region growing segmentation technique (a) black and white image after conventional thresholding, (b) selection of a pixel/voxel of the inclusion, shown as red dot inside the circle, and (c) selection of all voxels touching the selected voxel in 3D (26 connected)

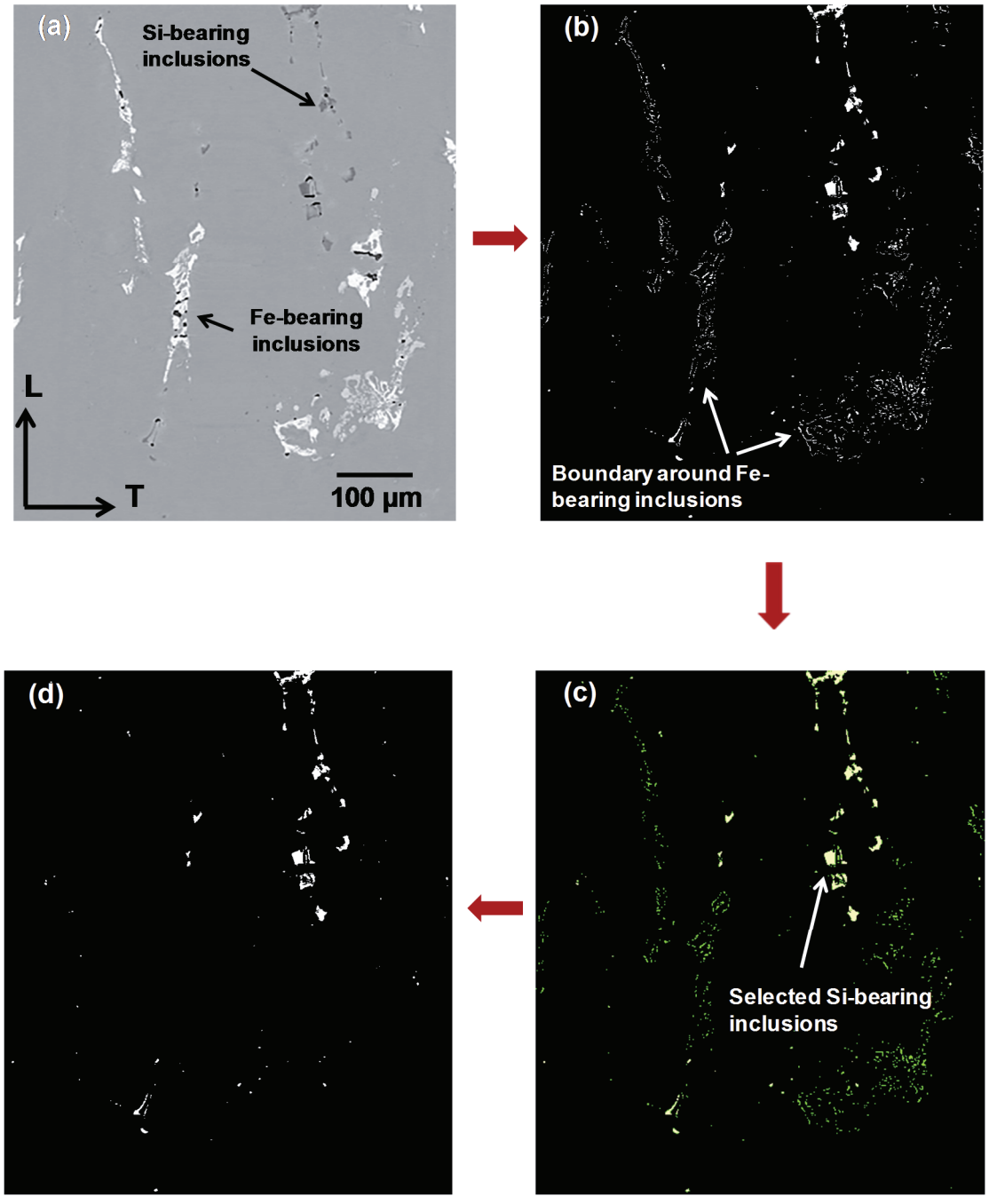

Figure 16. Step wise segmentation of Si-bearing inclusions (Mg_2Si) (a) gray scale image, (b) binary white and black image from thresholding in ImageJ, (c) selection of inclusions in MIMICS (indicated in yellow), and (d) final segmented image with only Si-bearing inclusions. Note that the unwanted boundaries around Fe-bearing inclusions in Fig. 16c (in green) are not selected

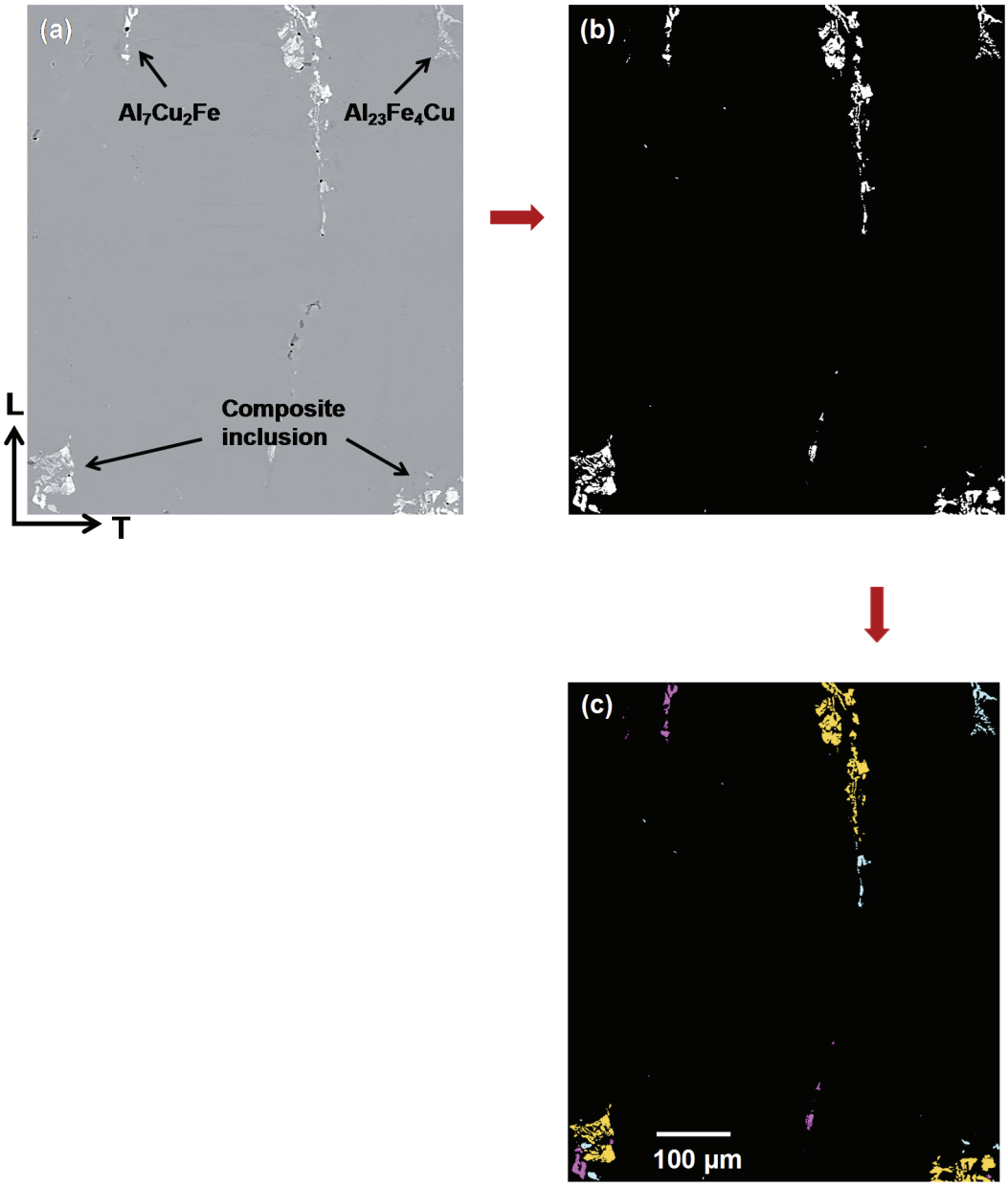

Figure 17. Segmentation of Fe-bearing inclusions (a) raw image showing different types of Fe-bearing inclusions, (b) initial segmentation of inclusions using thresholding followed by region growing as mentioned in Figure 16, and (c) Selection of different types of inclusions using region grow segmentation. Pink: Al_7Cu_2Fe, Blue: $Al_{23}Fe_4Cu$, and yellow: composite inclusions

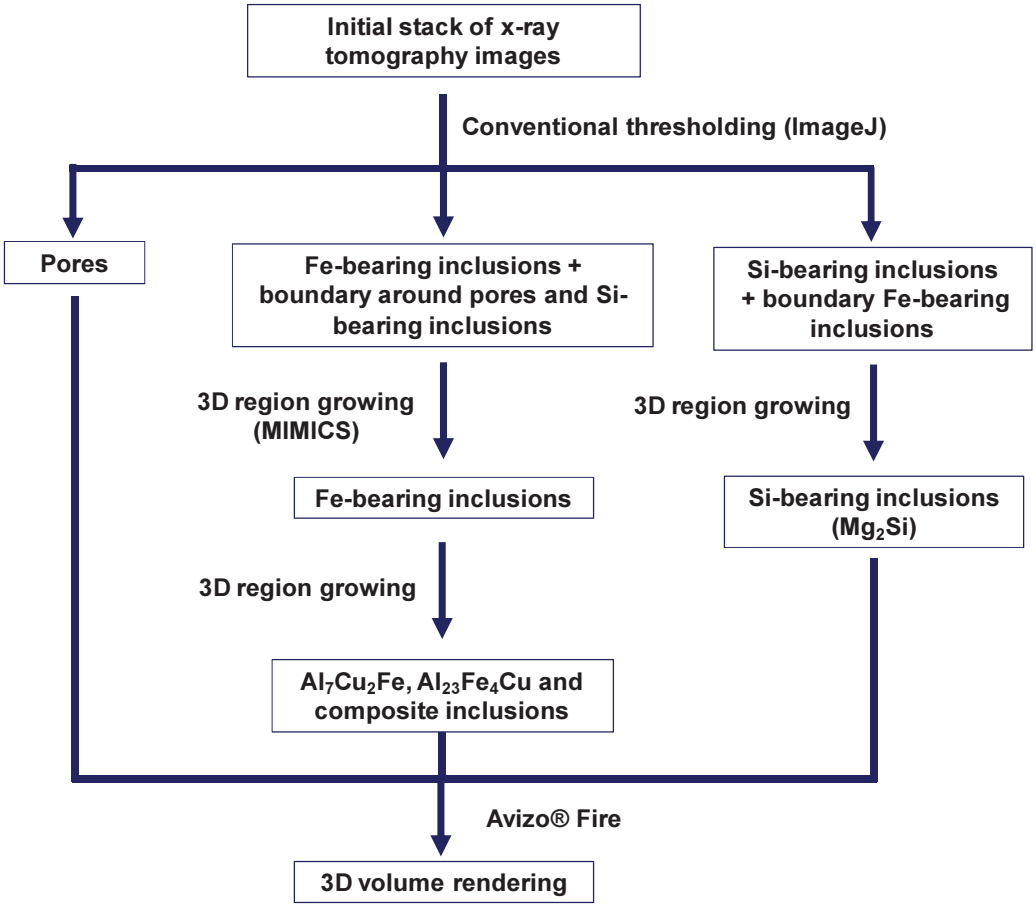

Figure 18. Flow chart of the segmentation of Fe-bearing inclusions (Al_7Cu_2Fe, $Al_{23}Fe_4Cu$ and composite inclusions), Si-bearing inclusions (Mg_2Si), and the pores

Figure 19 shows a 3D rendering of (a) Fe bearing inclusions, (b) Si bearing inclusions, (c) pores, and (d) all constituents. It can be seen that a uniform distribution of pores and both types of inclusions are present. Figure 20 shows the 3D rendering of Al_7Cu_2Fe, $Al_{23}Fe_4Cu$ and the composite inclusions separated from the initial segmented Fe-bearing inclusions.

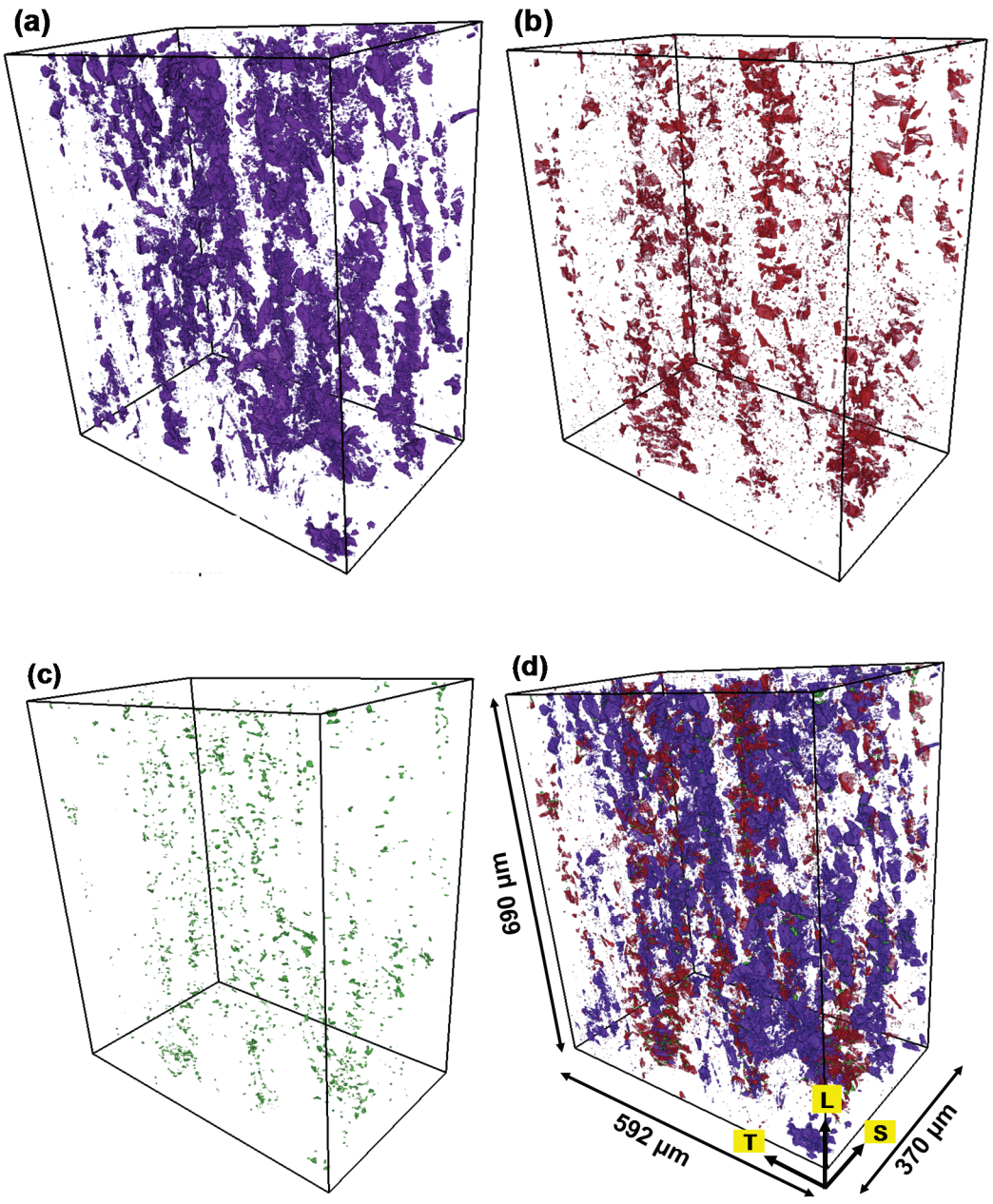

Figure 19. 3D volume distribution of (a) all Fe-bearing inclusions, (b) Si-bearing Inclusions, (c) pores, and (d) all. The dimensions and orientations are shown in Fig. d

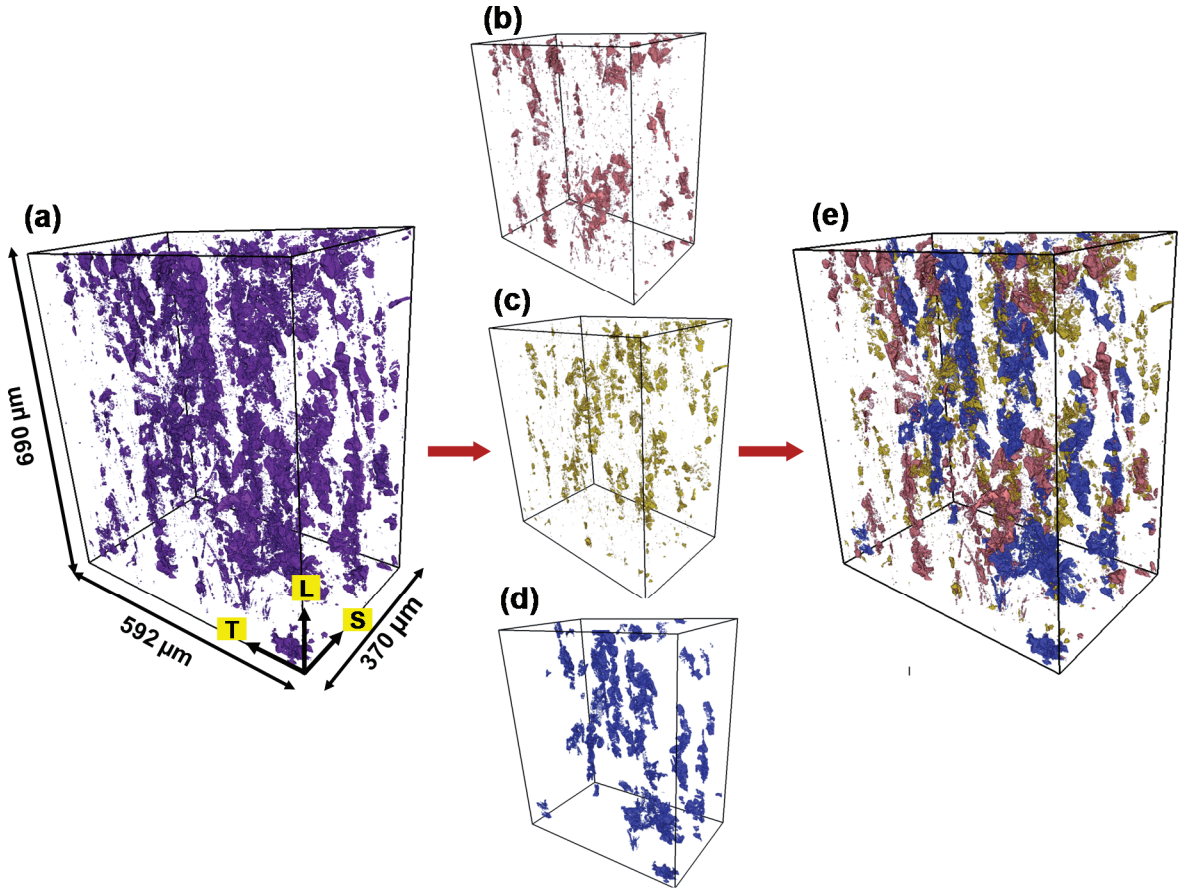

Figure 20. 3D volume distribution of (a) all Fe-bearing inclusions from initial segmentation (same as Fig. 19a), (b) Al_7Cu_2Fe, (c) $Al_{23}Fe_4Cu$, (d) composite inclusions (Al_7Cu_2Fe+$Al_{23}Fe_4Cu$), and (e) combination of b, c, and d

A very small volume of Figure 19d is shown in Figure 21. The small inclusions (small volume) appear to be spherical whereas the shape becomes irregular as the volume of the inclusion increases. This has also been reported for inclusions in AA 5182 by Moulin et al (Moulin et al. 2010). It is also interesting to note that the pores are associated with the inclusions, which is also clear from the 2D slices in Figure 13. These pores appear to be formed during the rolling process (Moulin et al. 2010; B. J. Connolly et al., others 2006). It is possible that the presence of the hard inclusions induces a triaxial state of stress and constraint in the matrix that would contribute to the formation of pores or voids in the matrix. It is also possible that a few of these pores may have formed during solidification. ImageJ was used to quantify the proportion of pores associated with the inclusions in the original volume (whole volume). About 99.05% pores were associated with the inclusions. Out of which 44.77% of the pores were associated with Fe-bearing inclusions, 49.41% with Si-bearing inclusions and 4.87 % pores were common to both the inclusions.

Quantitative analysis was performed to characterize the volume and size of the pores, Fe-bearing and Si-bearing inclusions, and is shown in Tables 3 and 4. The features having a volume of greater than 3.24 μm^3 (corresponding to 8 voxels) were taken into account for the measurements since inclusions with very small size (<1 μm) were on the order of the resolution of the technique, and do not play an important role in damage behavior of Al alloys (Eric Maire et al. 2006).

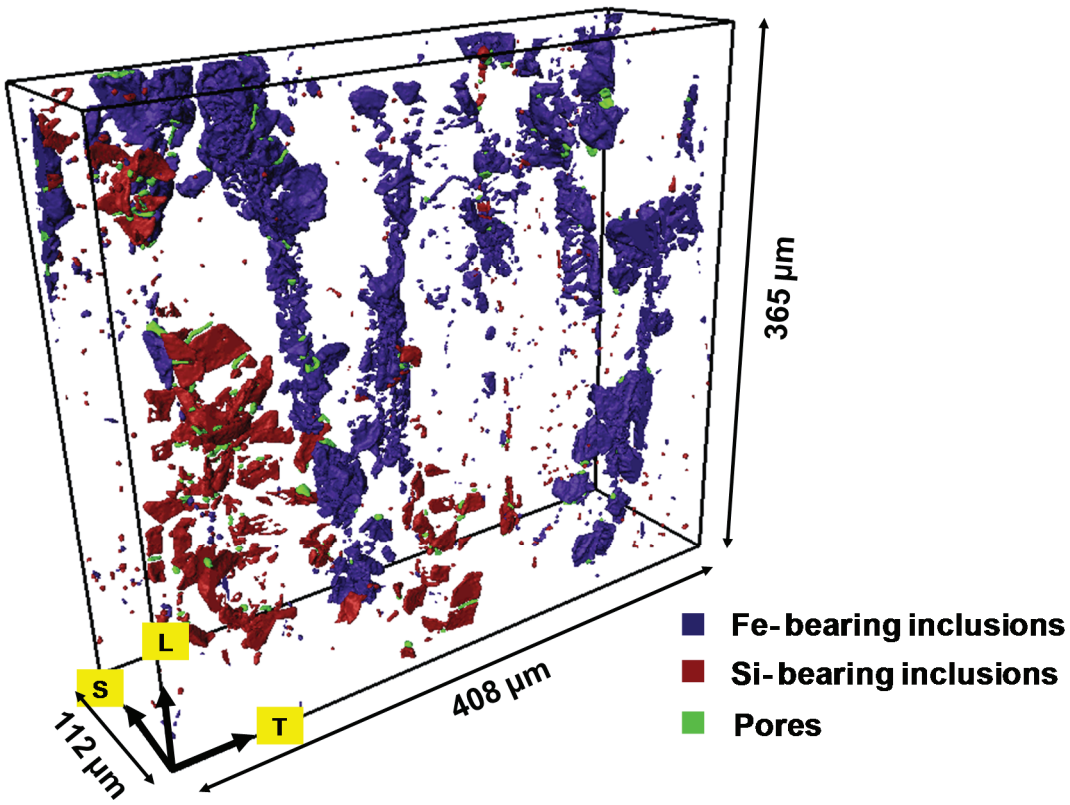

Figure 21. Small volume of the total volume (Fig. 19d). The inclusions with small volume are spherical in nature, whereas inclusions with high volume are irregular. Pores are always associated with inclusions

Table 3. Quantitative Analysis of Fe-bearing inclusions, Si-bearing inclusions and pores in Al 7075 alloys

Feature	Volume (%)	Number of particles in sampled volume	Avg. Size (μm^3)	Max. Size (μm^3)	Skewness
Al_7Cu_2Fe	0.43	2137	289	58,274	16.2
$Al_{23}Fe_4Cu$	0.27	3144	124	15,727	11.6
Composite inclusions	0.58	89	9,852	69,250	2.1
Mg_2Si	0.35	6897	74	13,510	14.5
Pores	0.06	1360	64	1,569	5.7

Table 4. Comparison of bounding box dimensions of inclusions and pores along 3 orthogonal directions (L-longitudinal direction, T-transverse direction, and S-short transverse direction)

Features	Average of highest 25% volume			Average of lowest 25% volume		
	L (μm)	T (μm)	S (μm)	L (μm)	T (μm)	S (μm)
Al_7Cu_2Fe	13.2	10.9	6.5	2.0	2.6	2.2
$Al_{23}Fe_4Cu$	12.3	11.7	6.1	1.9	2.4	1.9
Composite inclusions	146.7	82.2	40.2	4.5	5.4	3.1
Mg_2Si	9.1	9.8	5.8	1.6	2.3	2.3
Pores	8.5	11.7	8.9	2.3	3.3	2.9

The volume fraction of the pores and all inclusions were measured as 0.06 % and 1.63 %, respectively. Out of the 1.63%, the volume contribution of Si-bearing inclusions (Mg_2Si) is much less (~ 21%) than the Fe-bearing inclusions (~ 79%). In Fe-bearing

inclusions, the volume fraction of Al_7Cu_2Fe, $Al_{23}Fe_4Cu$ and the composite inclusions were 34.07 %, 20.82 % and 45.10 % respectively. As mentioned earlier, these constituent particles are formed during casting. Based on the ternary phase diagram of Al-Cu-Fe (Boettinger et al. 2006; V.S. Zolotorevsky, N.A. Belov, M.V. Glazoff, 2007), aluminum can exist in equilibrium with both types of Fe-bearing inclusions and they are formed at a range of temperature and composition. We believe that the local changes in temperature and compositions of the melt during casting often lead to the formation of both inclusions (Al_7Cu_2Fe and $Al_{23}Fe_4Cu$) in one particle, i.e. the composite inclusions. It is interesting to note that among the Fe-bearing inclusions, the mean volume of the composite inclusions is the highest although the count is the lowest. This indicates that the most of the large inclusions (with high volume) are associated with composite inclusions, whereas the Al_7Cu_2Fe and $Al_{23}Fe_4Cu$ with higher frequency distribution are mostly of smaller size. The same can be seen in the 3D rendering (Figure 20) and also in the volume distribution curves (Figure 22). A very high frequency of volume below 50 μm^3 was observed for Al_7Cu_2Fe and $Al_{23}Fe_4Cu$ (~82%, with skewness value of >10), whereas the composite inclusions exhibit a less skewed distribution (skewness of 2.1) with only about 25% volume below 250 μm^3 (Figure 22b). Skewness is a measure of the degree of asymmetry in a statistical distribution. Positive values of skewness indicate that the mean is higher than the median, while negative skewness values indicate the median is higher than the mean. The Si-bearing inclusions (Mg_2Si) and pores also show the high frequency of volume below 50 μm^3 with skewness values of 14.5 and 5.7 respectively. The high frequency of particles with relatively low volume fraction can be attributed to processing. Moulin et. al. (Moulin et al. 2010) and Maire et. al. (Eric Maire et al. 2006) performed X-

ray tomography on AA5182 and they showed that large and complex shaped inclusions formed during casting tend to break during hot rolling, leading to a higher frequency of smaller particles. To calculate the error in volume during thresholding, 27 Fe-bearing inclusions were selected. The error was calculated by increasing the threshold level (overestimation) from the actual threshold level, until it was visually found that the thresholding level can't be increased more. The same process was applied while decreasing the threshold level (underestimation). The average errors of the selected particles in both underestimation and overestimation were found to be only ~ 10%.

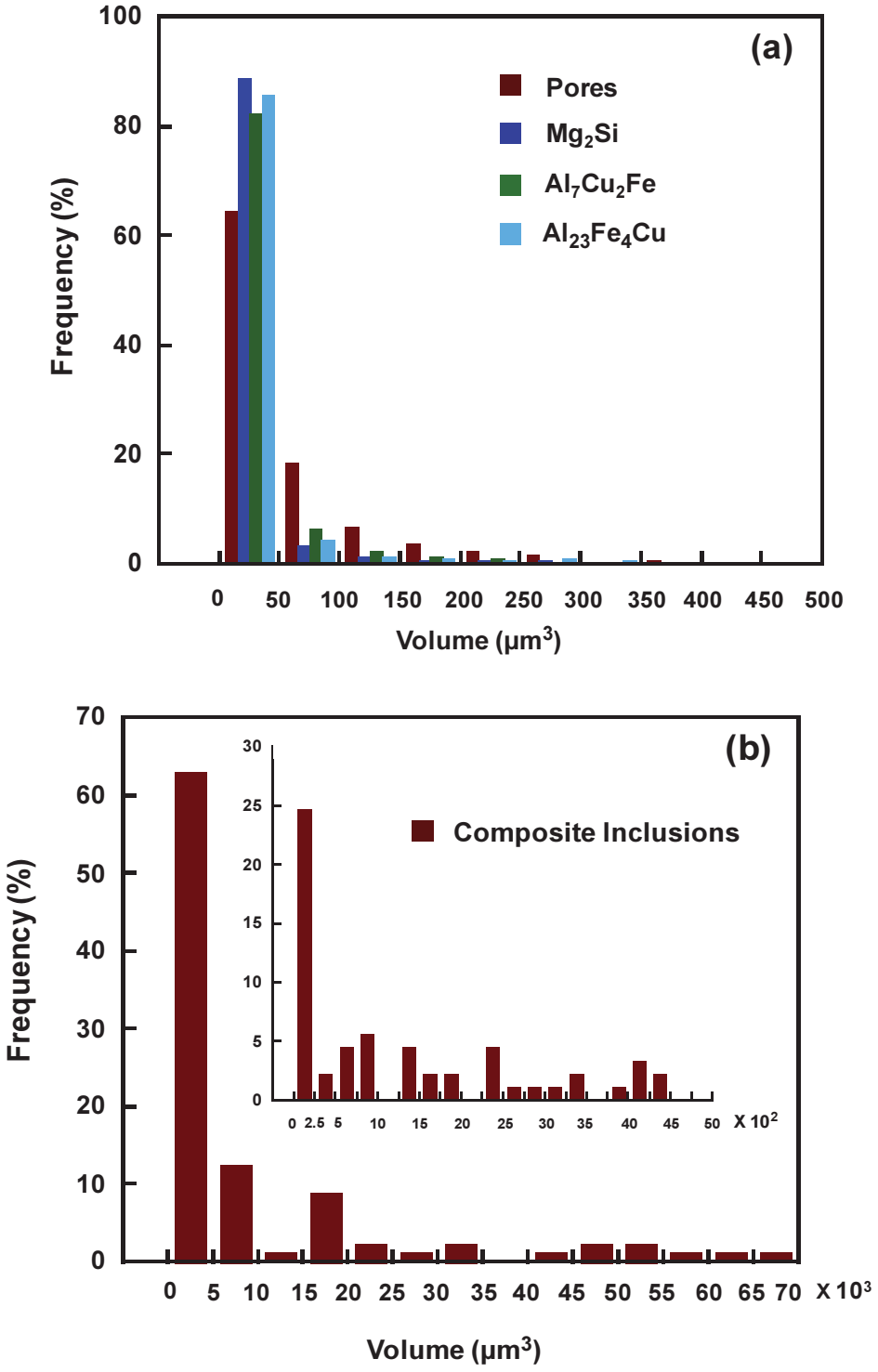

Figure 22. Frequency distribution of (a) pores, Mg_2Si, Al_7Cu_2Fe, $Al_{23}Fe_4Cu$, and (b) the composite inclusions

The size of the microconstituents along L, T and S was calculated from the dimensions of a bounding box (Table 4) using Matlab. Bounding box is defined as the smallest box which can fit a given particle. The average sizes of the inclusions and pores with the highest and lowest 25% volume have been summarized in Table 4. For small features (when the volume is small), the dimensions along the orthogonal directions are approximately the same, indicating the shape of the microconstituents to be nearly spherical, also shown in Figure 21. However, as the volume of the inclusions increases, the length along L and T gets larger than along S direction. The composite inclusions are longest along L and shortest along S directions indicating that the inclusions with high volume are significantly more elongated along rolling direction. Rollett et al. obtained 2D orthogonal optical micrographs and simulated the 3D microstructure of the constituent particles in Al 7075 alloys using pair correlation functions (Rollett, Campman, and Saylor 2006). They also showed that inclusions get aligned along the rolling direction during hot rolling process. The Si-bearing inclusions with high volume have a “pancake structure”, where the dimension along the S direction is smaller than L and T. The pores with high volumes are long along T direction, which is related to the higher dimension along T direction since pores are always associated with inclusions and form during rolling. The knowledge of the 3D microstructure of Al 7075 alloys, as obtained in this study, is very important since these inclusions act as a source of stress concentration during fatigue loading which leads to fatigue crack initiation (V. K. Gupta and Agnew 2011; Weiland et al. 2009; Rollett, Campman, and Saylor 2006). The 3D microstructure dataset can be incorporated into finite element models, along with the mechanical properties (obtained in next section), to understand the bulk deformation behavior.

3.3.3 Nanoindentation

Figure 23 shows representative load–displacement curves to an indentation depth of 1000 nm for the matrix and inclusions. All inclusions have higher loads than the matrix at the same indentation depth. Both Fe-bearing inclusions show the higher load than the Si-bearing inclusions. Representative Young's modulus and hardness curves as a function of the depth for the matrix and inclusions are shown in Figures 24(a) and (b), respectively. Young's modulus of a material can be calculated from the reduced modulus from equation 3 (Warren Carl Oliver and Pharr 1992). Since the Poisson's ratios of the inclusions are unknown, they were assumed to be 0.3. A Poisson's ratio of 0.33 was assumed for the matrix.

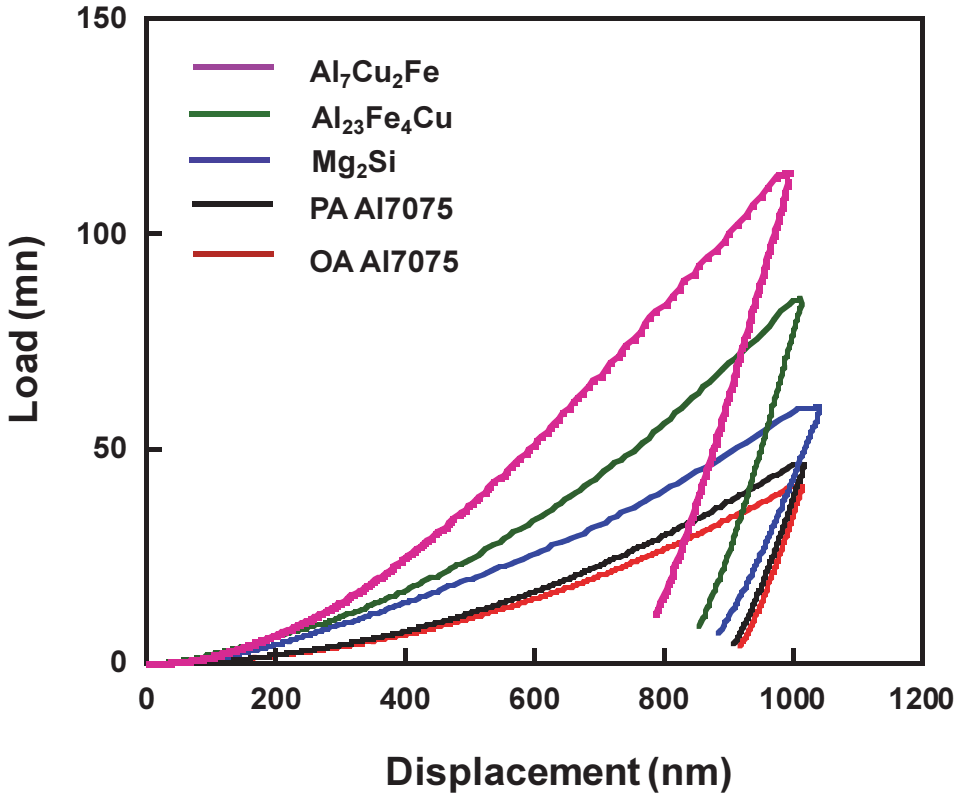

Figure 23. Representative load vs. displacement curves for matrix, Fe-bearing inclusions (Al_7Cu_2Fe, $Al_{23}Fe_4Cu$), and Si-bearing inclusions (Mg_2Si) indented to a depth up to 1000 nm

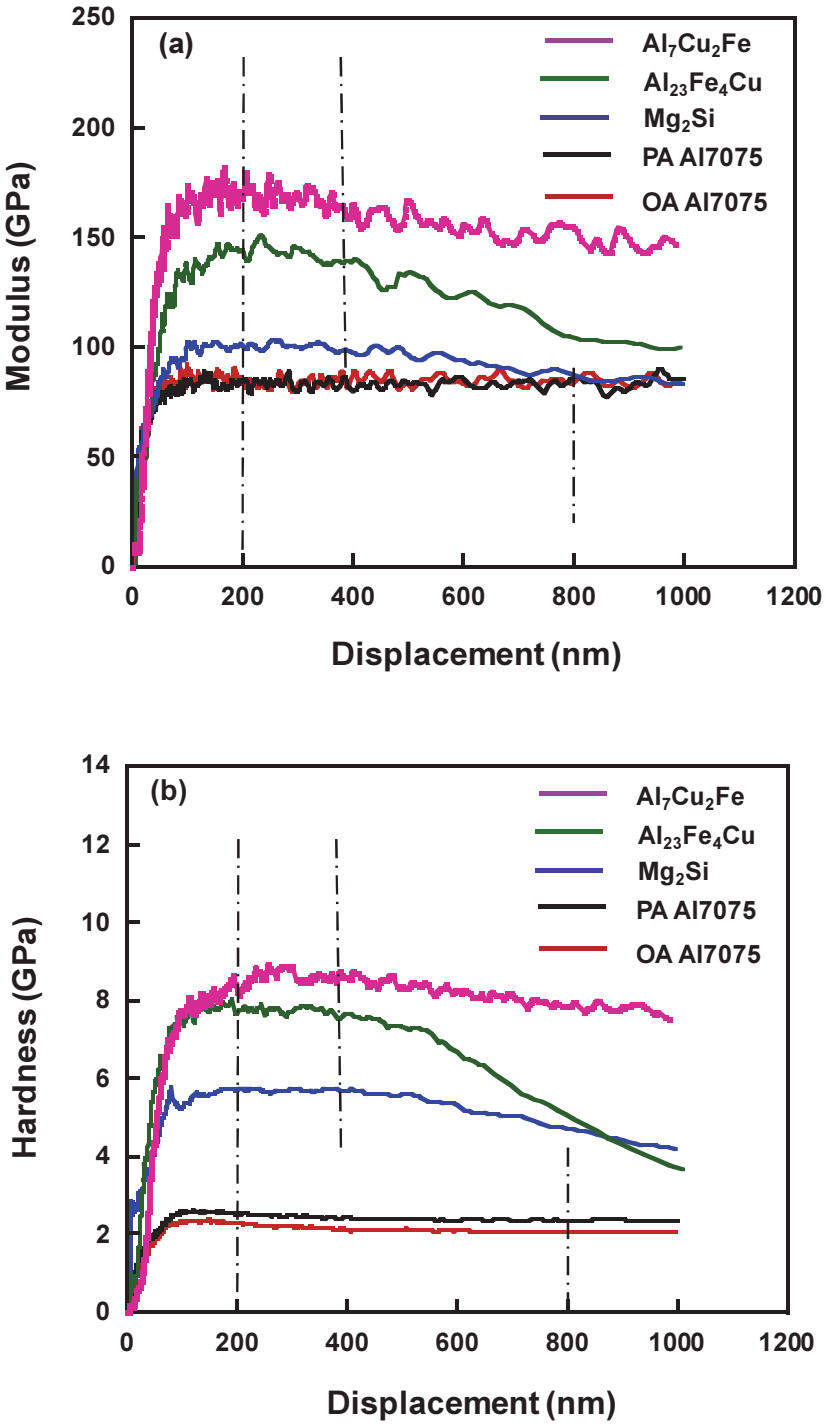

Figure 24. Nanoindentation behavior of Al 7075 matrix, Fe-bearing inclusions, and Si-bearing inclusions (a) Young's modulus-displacement curve, and (b) hardness-displacement curve. Young's modulus and hardness value were averaged from the plateau between 200-400 nm for inclusions and 200-800 nm for Al 7075 matrix

For Fe-bearing and Si-bearing inclusions, the Young's modulus and hardness was observed to be constant with respect to depth (plateau region) between approximately 200-400 nm. The gradual decrease in values of Young's modulus and hardness at the later depths may be attributed to the effect of the compliant matrix due to small size of the inclusions, also known as the substrate effect in nanoindentation. The Young's modulus and hardness of OA and PA 7075 matrix remains constant from around 200 nm until the total depth of the indentation i.e. 1000 nm. The Young's modulus and the hardness values for indentations were taken as the average values in the plateau region. Therefore, Young's modulus and hardness for inclusions was averaged between 200 and 400 nm, whereas, 200 to 800 nm was used for the Al 7075 matrix. Table 5 summarizes the measured Young's modulus and hardness for the matrix (PA and OA), both types of Fe-bearing inclusions and Si-bearing inclusions. It can be seen that the Fe-bearing inclusions are stiffer and harder than the Si-bearing inclusions and matrix, with the matrix having the lowest modulus and hardness value. The Young's modulus value for Al 7075 varies in between 70-80 GPa (Kumar, Rao, and Selvaraj 2011; Uvaraja and Natarajan 2012). It can be seen that both OA and PA alloys have similar Young's modulus values, reinforcing the fact that heat treatment doesn't affect Young's modulus of Al7075 alloys. The hardness value of PA is greater than OA, which is due to the interaction of dislocations with semi-coherent precipitates in PA alloys rather than by-pass of larger, incoherent precipitates in OA alloys (M. Meyers, K. K. Chawla 2008).

Table 5. Young's moduli and hardness of Al 7075 matrix, Fe-bearing inclusions and Si-bearing inclusions

	Al7075 (OA)	Al7075 (PA)	Al_7Cu_2Fe	$Al_{23}Fe_4Cu$	Mg_2Si
Modulus (GPa)	83.5 ± 1.2	84.3 ± 1.7	160.2 ± 10.9	139.5 ± 3.7	94.8 ± 7.5
Hardness (GPa)	2.06 ± 0.06	2.41 ± 0.08	8.8 ± 0.9	7.5 ± 0.8	5.2 ± 0.5

Young's moduli values of constituent particles from the literature (Bozek et al., others 2008; Patton et al. 1998; Oswald 2003) are listed down for comparison in Table 6. As shown in Table 6, the earlier reported values of Young's modulus show a significant amount of variability from 115.2-169 GPa for Al_7Cu_2Fe and 44.9-99.4 GPa for Mg_2Si, whereas, the values for $Al_{23}Fe_4Cu$ have not been reported yet. Since the size of the constituent particles vary, it is difficult to know the depth of indentation required to get the reliable measurement of modulus and hardness from the slope of the unloading curve due to the effect of the matrix. It should be noted here that all authors (Bozek et al., others 2008; Patton et al. 1998; Oswald 2003) have used the Oliver and Pharr method, i.e., they used the slope of unloading curve (Warren Carl Oliver and Pharr 1992), instead of CSM technique utilized in this work, where the modulus and hardness can be obtained with depth, leading to the accurate measurement of Young's modulus and hardness. Patton et al. (Patton et al. 1998) reported the modulus values of 132-167 GPa for Al_7Cu_2Fe and 82.3-99.4 GPa for Mg_2Si. The Young's modulus value monotonically decreased as load was increased in their experiments (no plateau region). This might be due to the small size of inclusions leading to effect from soft matrix. Due to variability in

results, they reported high variability over varying loads. Oswald (Oswald 2003) obtained mean modulus values of 133.6 GPa for Fe-bearing inclusions and 50.1 GPa for Si-bearing inclusions, which are much lower than the values reported by us. This lower value of modulus for both inclusions might be attributed to a matrix effect and different composition of the inclusion. In their study, indentation was made only on a single inclusion and the author also agreed that more indentations are required for statistical representation of the entire population of microstructural features. Bozek et al. (Bozek et al., others 2008) reported a mean value of 160.9 GPa for Fe-bearing inclusion, same as us, however the testing technique and sample's condition has not been given in detail. As mentioned before, the stoichiometry of Si-bearing inclusions is similar to Mg_2Si, therefore the modulus should be close to Young's modulus of Mg_2Si i.e. 120 GPa (Asano and Yoneda 2008; Wang et al. 2007). The modulus and hardness values for $Al_{23}Fe_4Cu$ are about 139 GPa and 7.5 GPa. The lower modulus and hardness of $Al_{23}Fe_4Cu$ from Al_7Cu_2Fe are due to the higher amount of aluminum present in the inclusions.

Table 6. Comparison of Young's moduli and hardness of Fe-bearing and Si-bearing inclusions from literature

	Modulus (GPa)	Hardness (GPa)
Si-bearing inclusions (Mg_2Si)	94.8 ± 7.5 [This study] 82.3 - 99.4 [25] 44.9 – 55.3 [26]	5.2 ± 0.5 [This Study] 4.1 – 5.9 [25] 1.56 – 3.44 [26]
Fe-bearing inclusions (Al_7Cu_2Fe)	160.2 ± 10.9 [This Study] 153.34 – 168.46 [24] 132 – 167 [25] 115.2 – 154.8 [26]	8.8 ± 0.9 [This Study] 8.5-12.4 [25] 5.2 – 8 [26]
Fe-bearing inclusions ($Al_{23}Fe_4Cu$)	139.5 ± 3.7 [This study]	7.5 ± 0.8 [This study]

Scanning electron microscope images of indentations are shown in Figure 25. Some pile-up can be seen around the matrix indentation, whereas little evidence of pile-up or sink-in is present in the indentation micrographs for Fe-bearing and Si-bearing inclusions. However, with CSM the Young's modulus and hardness are measured at relatively low depths, where the values do not change with depth, so the influence of pile-up at lower depths should be less significant.

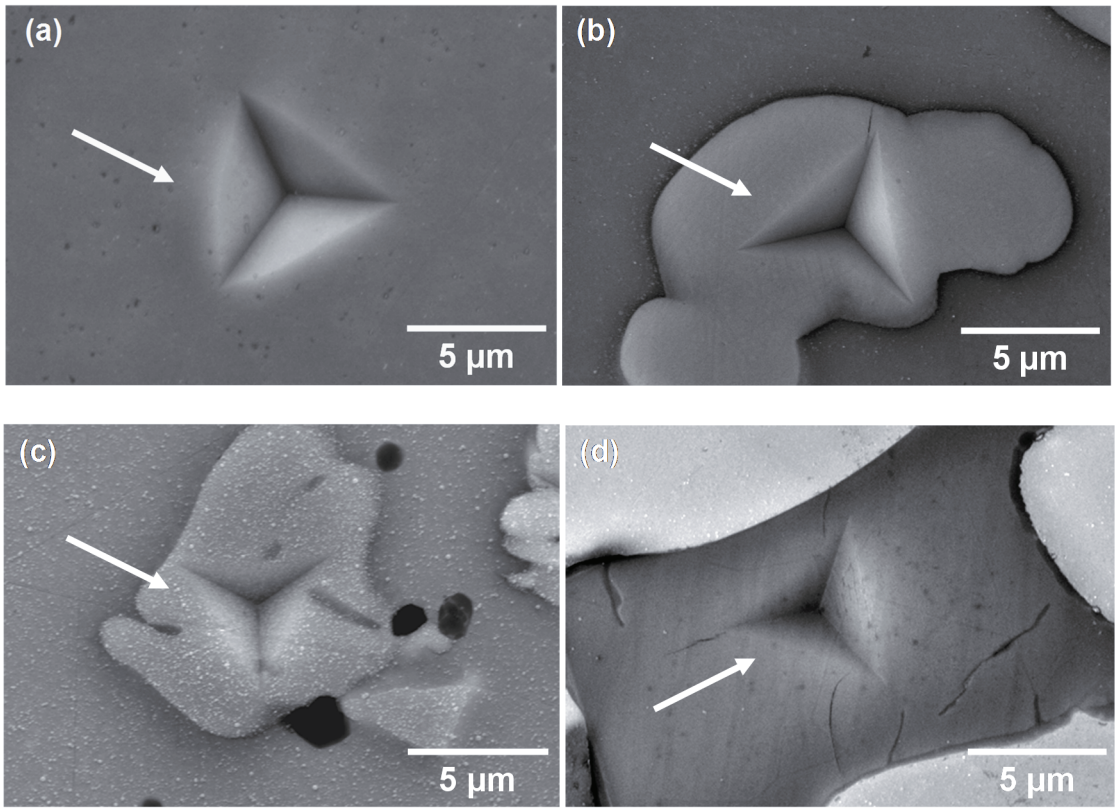

Figure 25. Scanning electron micrographs of indentations in (a) Al 7075 matrix, (b) Fe-bearing inclusion (Al_7Cu_2Fe), (c) Fe-bearing inclusion ($Al_{23}Fe_4Cu$), and (d) Si-bearing inclusion (Mg_2Si). Pile-up can be seen around the indentation edge in Al matrix

3.4 Summary

The 3D microstructure and mechanical properties of the constituent particles present in Al 7075 alloys were obtained using X-ray synchrotron tomography and nanoindentation. 3D visualization showed that the constituent particles and pores are uniformly distributed and all pores are associated with the inclusions. The total volume fraction of the inclusions was much higher (1.63 %) than that of the porosity (0.06 %). Of the inclusions, the highest volume fraction of particles were composite inclusions of Al_7Cu_2Fe and $Al_{23}Fe_4Cu$ (0.58%). Quantitative analysis showed that the inclusions with

small volume were spherical in nature. However, as the volume of the inclusions increased, the lengths along L and T increased much more than along the S direction. Nanoindentation with continuous stiffness measurement (CSM) was used to accurately measure the Young's modulus and hardness values of inclusions in the Al 7075 alloy. The Young's modulus values of Al_7Cu_2Fe, $Al_{23}Fe_4Cu$, and Mg_2Si were measured to be 160.2 ± 10.9, 139.5 ± 3.7, and 94.8 ± 7.5 GPa respectively. Values of hardness of Al_7Cu_2Fe, $Al_{23}Fe_4Cu$, and Mg_2Si were 8.8 ± 0.9, 7.5 ± 0.8, and 5.2 ± 0.5 GPa respectively. We believe that the 3D microstructure combined with the accurate measurement of mechanical properties of the constituent particles in Al7075 alloys will be instrumental in understanding the bulk deformation behavior of these materials.

CHAPTER 4

MECHANICAL PROPERTIES OF INTERMETALLIC INCLUSIONS IN Al 7075 ALLOYS BY MICROPILLAR COMPRESSION

4.1 Introduction

Al 7075 alloys are used extensively in structural applications due to their high strength-to-weight ratio (Bucci, Warren, and Starke 2000; Starke and Staley 1996). In commercial Al 7075 alloys, the predominant types of inclusions are Al_7Cu_2Fe and Mg_2Si (Starke and Staley 1996; Payne et al. 2010; Xue et al. 2007). These inclusions (also known as constituent particles) are formed from impurities and alloying elements reacting during the casting process. These particles are not dissolved in subsequent thermo-mechanical rolling and/or extrusion, although fracture and redistribution has been shown to take place (V. K. Gupta and Agnew 2011).

Constituent particles (Mg_2Si and Al_7Cu_2Fe) play very important roles in fatigue and tensile behavior of aluminum alloys since small cracks have been observed to nucleate from these particles (V. K. Gupta and Agnew 2011; Pearson 1975; Weiland et al. 2009; Eric Maire et al. 2011; Lugo et al. 2011). These cracks initiate either by the debonding of the interface between the matrix and inclusions or by cracking of the inclusion itself (Payne et al. 2010; Weiland et al. 2009; Harlow, Nardiello, and Payne 2010). Damage begins with cracking of the constituent particles followed by growth of voids and then void coalescence (Harris 2005). Therefore, in order to understand the overall mechanical behavior of Al 7075 alloys, a thorough understanding of mechanical properties of these constituent particles is necessary.

Bulk Al_7Cu_2Fe and Mg_2Si intermetallics have been fabricated, but mostly by powder metallurgy route (L. Guillaume 2011; Laplanche et al. 2014; Wang et al. 2007; Xiong, Qin, and Wang 2007). Intermetallics fabricated by powder metallurgy would be significantly different from the actual constituent particles formed during casting of Al alloys in terms of porosity, oxidation, etc. Indeed, the Young's modulus and hardness values of the bulk Mg_2Si and Al_7Cu_2Fe and the constituent particles in Al alloys show large variability at room temperature (Laplanche et al. 2014; Wang et al. 2007). Therefore, the mechanical properties of the actual constituent particles in Al alloys need to be evaluated, which is a challenge due to the small size of these particles (typically only a few micrometers in size).

Nanoindentation is an excellent technique to obtain mechanical properties of microstructural constituents (Xie and Chawla 2013; Dudek and Chawla 2010). However, only Young's modulus and hardness can be extracted from nanoindentation. In chapter 3, Young's modulus and hardness of these inclusions were accurately obtained using continuous stiffness measurement (CSM) in nanoindentation. Micropillar compression is an attractive technique to quantify uniaxial mechanical properties, such as stress-strain behavior, at small-length scales (Greer and De Hosson 2011; Guo, Xie, et al. 2014; L. Jiang and Chawla 2010). This technique involves the fabrication of pillars of micron scale, followed by compression using a nanoindenter with a flat punch (Uchic, Shade, and Dimiduk 2009b; Greer, Oliver, and Nix 2005; Stewart et al. 2012). Furthermore, individual mechanical properties of these microstructural constituents, along with the alloy microstructure, can then be incorporated into finite element models to accurately

predict the bulk deformation behavior of the alloy (Padilla et al. 2012; Guo, Singh, et al. 2014).

In this work, micropillar compression was employed to quantify the deformation behavior of constituent particles and the matrix in Al 7075 alloys. To the best of our knowledge, this is the first time the stress-strain behaviors of actual inclusions in the alloy have been obtained experimentally.

4.2 Materials and Experimental Procedure

The material used in this study was a 7075-T73 aluminum alloy. The commercially available 7075-T651 aluminum alloy (2.5 cm thick, Alcan rolled product, supplied by Dix Metals Inc.) was solution treated at 475^{o}C for 2 hours, quenched in water, and annealed at 107^{o}C for 6 hours followed by annealing at 163^{o}C for 40 hours to obtain over-aged condition (T73). The specimens were polished to a 1 μm diamond finish and then to a final finish using 0.05 μm colloidal silica.

A dual-beam focused ion beam (FIB) with scanning electron microscope (SEM) (Nova 200 NanoLab FEGSEM/ FIB, FEI Co, Oregon) was used to fabricate the micropillars. Energy dispersive spectroscopy (EDS) analysis was performed before fabrication of micropillars to identify the inclusions. Due to the small size of the inclusions, pillars of smaller volume had to be fabricated on inclusions. For comparison, pillars of similar dimensions were fabricated in the matrix as well. Initially, a beam of Ga^{+} ions accelerated at 30 KeV with a current of 5nA was used to mill out a circular trench of diameter ~25 μm, providing enough clearance for the flat punch, and a coarse pillar of 7 μm diameter at the center. This was followed by milling the pillar to a

diameter of 3.5 μm by using a lower current value of 1 nA. Finally, a very small current of 0.1 nA was used to obtain pillars with a nominal top diameter of 1.3-1.5 μm. The aspect ratio (length/ diameter) of the pillars was typically between 2.7 to 3.4 in Si-bearing inclusions, Fe-bearing inclusions, and Al 7075 matrix. The use of low current (100 pA) led to a taper angle of less than 3°. After fabrication of pillars, EDS was again performed at the base of the pillar to confirm that the base of the pillar was the same as that of the pillar itself.

The micropillars were compressed using a nanoindenter (MTS XP, Agilent Technologies, AZ). A Berkovich (three-sided pyramid) diamond indenter tip with a flat triangular cross-section (10 μm side) was used for compression. Samples were mounted on aluminum stubs for pillar compression testing using a mounting adhesive (Crystalbond™, West Chester, PA). The specimens were mounted at the flow temperature of the crystalbond (135° C) for a few seconds. This short duration of heating did not lead to any significant change in the microstructure of the matrix or inclusions. The displacement rate was changed (4.5–6 nm/s) according to the height of the pillars to maintain a constant strain rate of $\sim 10^{-3}$ s^{-1}. All tests were carried out with a thermal drift value of less than 0.05 nm/s. Sneddon's correction criterion was used to obtain the actual displacement of the pillars (Fei et al. 2012; Frick et al. 2008). The top diameter of the pillar was used to calculate stress values. The top diameter was used since it is straightforward to define. It should be mentioned that the pillars fabricated using FIB have some taper and therefore the stress measured using the top diameter represents the upper bound stress. For comparison, stress values using diameter at the middle height of

the pillars were also calculated. After compression, deformation of the pillars was observed using a scanning electron microscope (SEM).

4.3 Results and Discussion

Figure 26 shows the microstructure of the Al7075-T73 used in this study. The two types of constituents particles can be clearly seen in the SEM image: One brighter than the matrix and the other darker than the matrix. Energy Dispersive Spectroscopy (EDS) analysis was conducted to obtain chemical compositions of these inclusions. The bright inclusions contain aluminum, copper, and iron as primary elements with an approximate atomic ratio of 7:2:1, indicating that inclusions are probably Al_7Cu_2Fe (Fe-bearing inclusions). The darker inclusions have magnesium and silicon as major elements with an approximate atomic ratio of 2:1, along with small amount of oxygen and aluminum, indicating these to be Mg_2Si (Si-bearing inclusions).

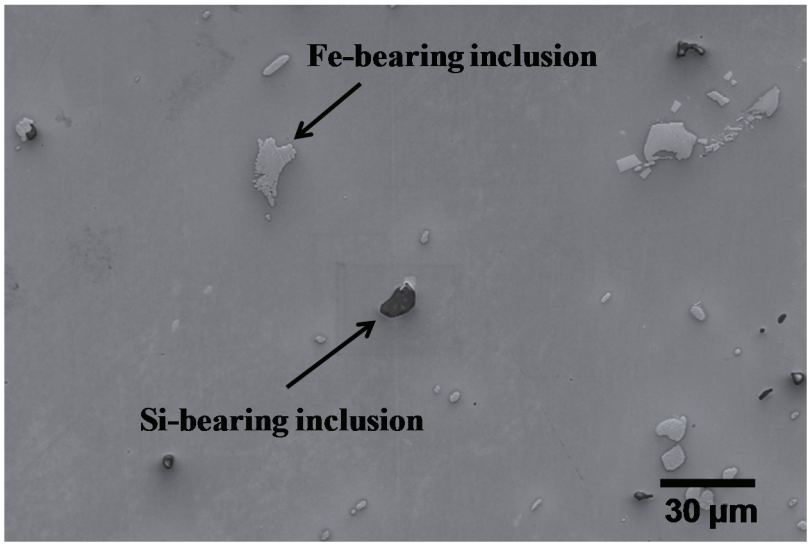

Figure 26. Scanning electron microscopy (SEM) image showing Fe-bearing and Si-bearing inclusions in Al7075 alloys

Figure 27 shows low magnification SEM images of micropillars on both inclusions and the matrix fabricated using FIB. The images were taken at low magnification to show the clear boundary between the inclusion and the matrix, and that the pillars were made at the center of the inclusions. Figure 28 shows the higher magnification SEM images of micropillars on inclusions (Figure 28a for Fe-bearing inclusions, Figure 28b for Si-bearing inclusions, and on matrix Figure 28c).

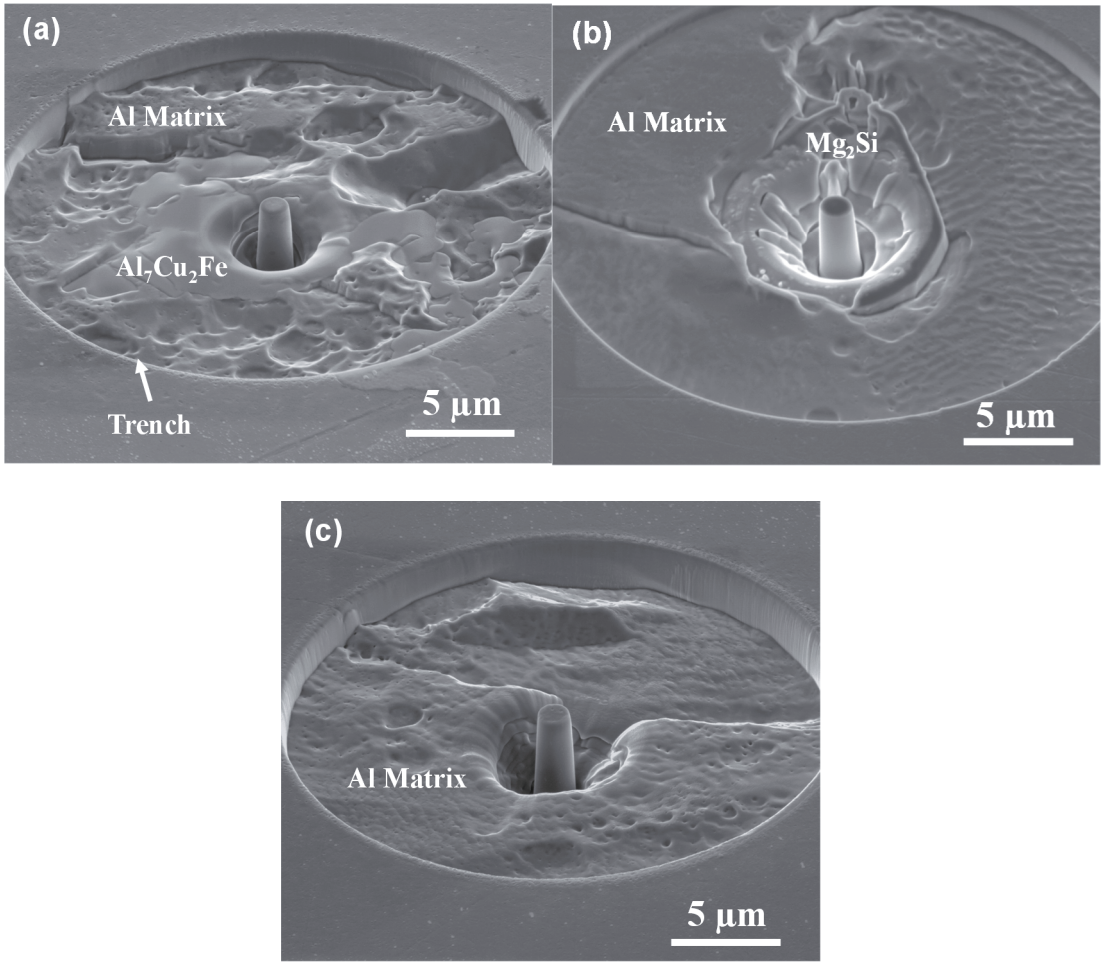

Figure 27. SEM images of micropillars fabricated using FIB (a) Fe-bearing inclusion (Al_7Cu_2Fe) (b) Si-bearing inclusion (Mg_2Si) and (c) Al 7075 Matrix. The boundary of inclusions can clearly be seen in (a) and (b). (a, c) were taken at an angle of 52°, and (b) at 40°

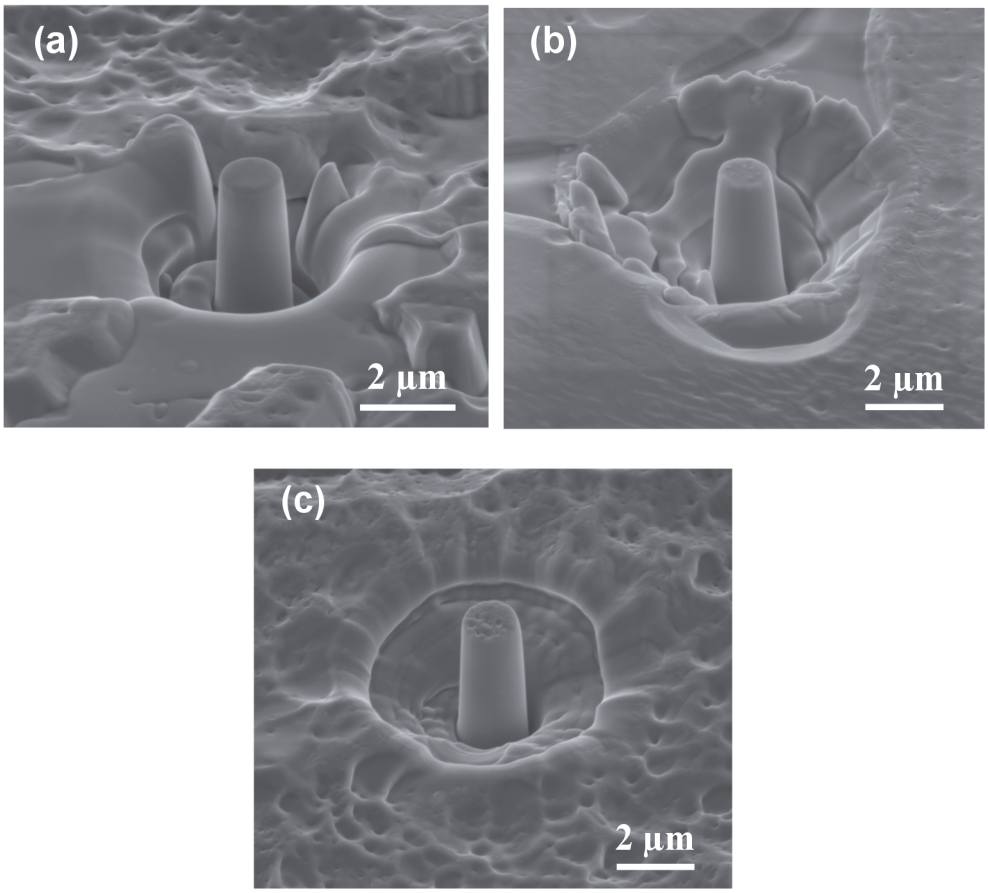

Figure 28. Representative SEM images of fabricated pillars on (a) Al_7Cu_2Fe, (b) Mg_2Si, and (c) Al 7075 matrix. Images were taken at an angle of 52° for (a, b), and 42° for (c)

Figure 29 and Figure 30 show the stress-strain behavior (using the top diameter) and SEM images after pillar compression, respectively. The stress-strain curves of all repeat tests in the same microconstituent showed similar signatures, indicating small experimental variations from pillar to pillar. In the case of Al_7Cu_2Fe, the stress-strain curves (Figure 29a) are linear until the catastrophic failure of the pillars at about 2% strain. The absence of plastic deformation indicates that Fe-bearing inclusions are quite brittle in nature. Observation of the compressed pillars (Figure 30a) indicate that the pillars fractured by cleavage along certain planes, as shown with arrows. The

compressive failure strength value of Fe-bearing inclusions was measured to be 2.5 ± 0.2 GPa. The failure strength for brittle Al_7Cu_2Fe was defined as the stress value where the large strain burst occurred. The pillars on Mg_2Si showed a strain burst after the linear region (Figure 29b) and then the stress values increased with strain, showing significant strain hardening. Apart from the role of dislocations, taper of the pillars might have contributed to the strain hardening (Haitao Zhang et al. 2006; Kiener, Motz, and Dehm 2009). As shown in Figure 30b, we believe that the strain burst after the linear region relates to slip band formation due to yielding, as marked in arrow. The compressive yield strength of Si-bearing inclusions was calculated to be 1.8 ± 0.1 GPa (corresponding to the first strain burst). The pillars on Al 7075 matrix exhibited large plasticity as shown in Figure 29c. Strain bursts observed on the stress-strain curves are possibly due to the formation of slip bands during compression, which are commonly observed in the compression of face centered cubic (F.C.C) micropillars (Uchic, Shade, and Dimiduk 2009a). The observed compliance during the initial loading segment in the stress-strain curves might be attributed to slight misalignments between the micropillar surface and the flat punch and roughness of the top surface of the pillars (Frick et al. 2008; Soler et al. 2012). Figure 29d shows the stress-strain curves of all the pillars for comparison. It is evident that the strength of Fe-bearing inclusions is the highest followed by Si-bearing inclusions, and then the 7075 matrix. In general, it has been shown that a higher value of hardness relates to higher yield and tensile strength in the materials (P. Zhang, Li, and Zhang 2011). The strength values here qualitatively agree with the hardness results obtained by nanoindentation in chapter 3, i.e., highest hardness values seen in the Fe-bearing inclusions followed by that of Si-bearing inclusions and then Al 7075 matrix. The

compressive failure strength and yield strength of Al_7Cu_2Fe and Mg_2Si using the diameter at the middle of pillar height were measured to be 1.9 ± 0.2 GPa and 1.3 ± 0.05 GPa, respectively. The values are ~24% and ~28% lower for Al_7Cu_2Fe and Mg_2Si, respectively, than the stress values measured using the top diameter.

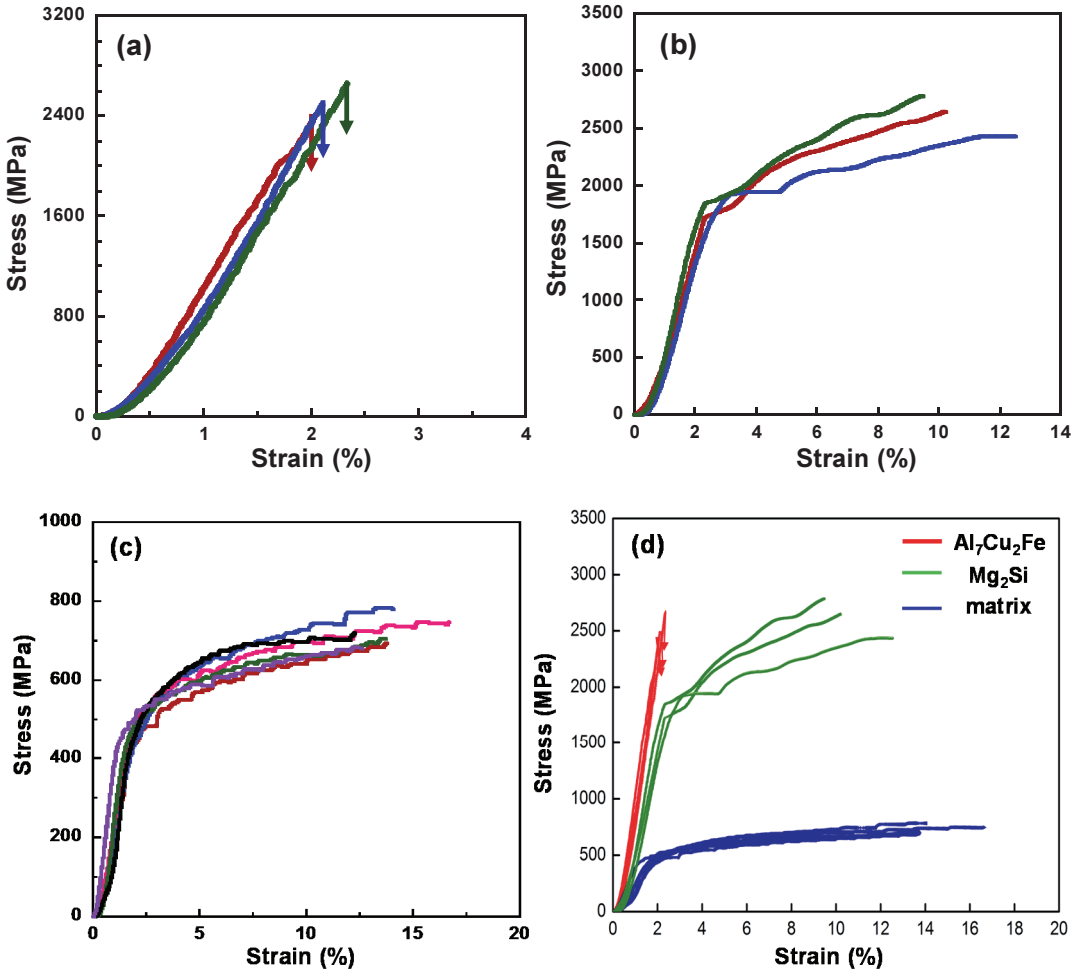

Figure 29. Stress-strain curves (a) Fe-bearing inclusions, (b) Si-bearing inclusions, (c) Al 7075 matrix, and (d) combination of inclusions and the matrix

Several studies have been conducted on the synthesis and mechanical properties of bulk Al_7Cu_2Fe and Mg_2Si. Most of these have used a power metallurgy route to fabricate bulk samples (L. Guillaume 2011; Laplanche et al. 2014; Wang et al. 2007;

Xiong, Qin, and Wang 2007). Our tests were conducted on Al_7Cu_2Fe and Mg_2Si particles formed during casting of Al 7075 alloys, and therefore represent the true composition and corresponding mechanical properties of constituent particles. Al_7Cu_2Fe is an intermetallic with a complex tetragonal crystal structure (Space group: P4/mnc, parameters a = 0.6336 nm and c = 1.487 nm) (L. Guillaume 2011). It has been shown that Al_7Cu_2Fe is brittle at room temperature and shows plasticity at high temperature, although powder metallurgy was used for fabrication of the bulk samples (L. Guillaume 2011; Laplanche et al. 2014).

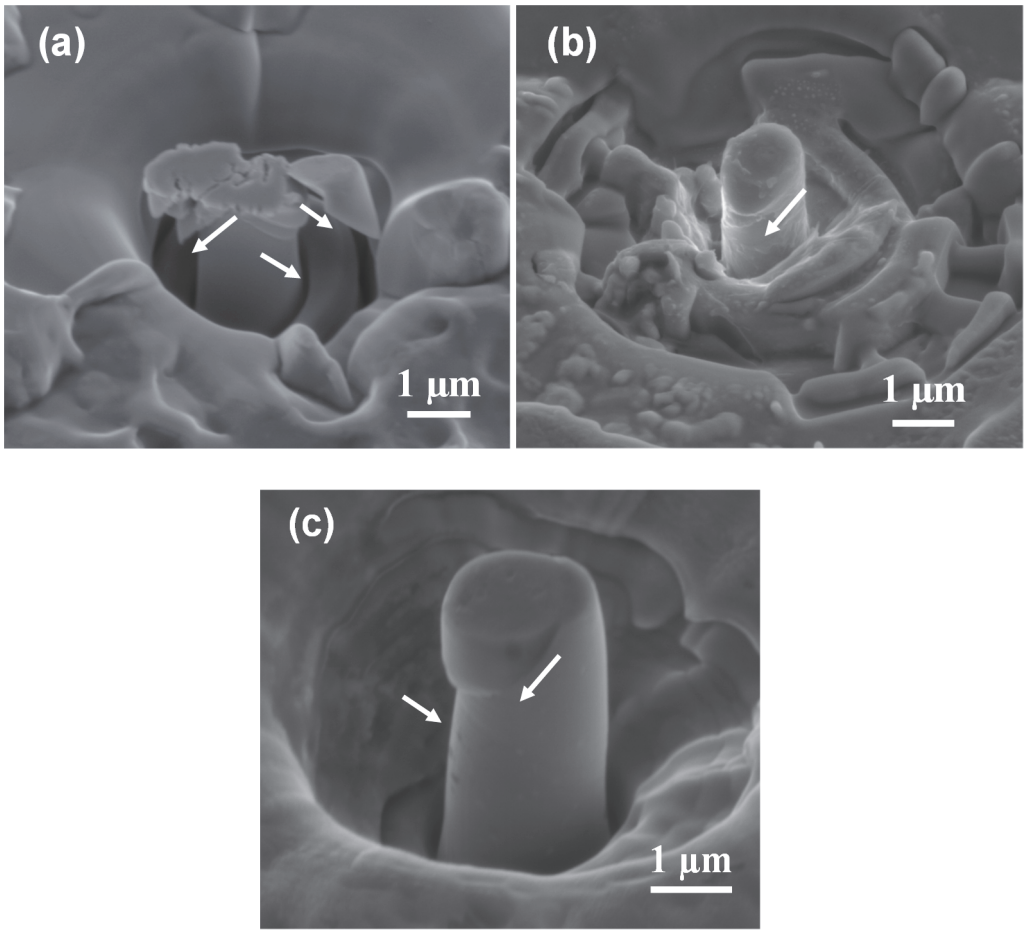

Figure 30. Representative SEM images of pillars after deformation: (a-b) Al_7Cu_2Fe, (c-d) Mg_2Si, and (e-f) Al matrix. Arrows in the images show the slip directions during compression. Images were taken at angle of ~42°

Bulk Mg_2Si has been found to be brittle at room temperature (Wang et al. 2007; Muñoz-Palos, Cristina, and Adeva 1996; Takeuchi, Hashimoto, and Suzuki 1996), as opposed to the limited plasticity observed during pillar compression in this study. Bulk Mg_2Si fabricated through powder metallurgy route (Wang et al. 2007; Muñoz-Palos, Cristina, and Adeva 1996), and through melting of the pure powders (Takeuchi, Hashimoto, and Suzuki 1996) showed completely different brittle to ductile transition temperatures of ~723 K and ~550 K respectively, indicating the dramatic effect of processing route on the mechanical properties of bulk Mg_2Si. This difference in mechanical properties might be attributed to the different microstructure in terms of grain size, defect concentration, and type (such as residual porosity) etc. Recently, several micropillar compression studies have shown that materials, which are brittle in bulk form, can be deformed plastically at small length scale (Östlund et al. 2009; Michler et al. 2007; Korte and Clegg 2011; Östlund et al. 2011). It was concluded that reducing the size of the samples suppresses cracking, so that only plastic deformation is observed if the test specimen is made sufficiently small (Östlund et al. 2011). The different processing route of Mg_2Si in Al 7075 alloy and use of the small size of the pillars (which nearly corresponds to average size of the particle found in this alloy) might be the possible reasons for the observed plastic deformation. The compressive strength of Mg_2Si has been reported to be 1640-1670 MPa (Wang et al. 2007; Xiong, Qin, and Wang 2007), slightly lower that the observed yield stress of about 1800 MPa in this study. Xiong et al. (Xiong, Qin, and Wang 2007) performed Vickers hardness testing on compacts with different densities, prepared using powder metallurgy route (hot-pressing sintering), and then extrapolated the obtained hardness data to 100% relative density to obtain the

hardness of Mg_2Si without porosity. They reported a compressive yield strength (σ_y) value of ~1670 MPa at room temperature assuming that the relation HV~$3\sigma_y$ was also valid for this material, where HV is the Vickers hardness. Oswald (Oswald 2003) measured the hardness and Young's modulus of these inclusions using nanoindentation and qualitatively plotted the stress-strain curves, where it was shown that Al_7Cu_2Fe had highest strength and modulus similar to what we have reported here. However, due to the similar hardness of Al matrix and Mg_2Si, it was concluded that both had similar yield strength, but the strain of Mg_2Si at a given stress would be higher due to lower modulus values of Mg_2Si than the Al matrix. However, studies (Patton et al. 1998) including ours in chapter 3 have shown that the hardness and modulus of Mg_2Si were higher than that of the matrix.

The effect of these inclusions on fatigue and tensile performance has been studied extensively. It was shown that Al_7Cu_2Fe are the only source of crack initiation and Mg_2Si particles don't really influence the crack initiation process (Payne et al. 2010; Xue et al. 2007). Gurbuz et al. (Gürbüz and Alpay 1994) also observed that the irregularly shaped Al_7Cu_2Fe particles were easily fractured with no evidence of plastic deformation, whereas, spherical shaped Mg_2Si particles were not fractured. The results here corroborate with this observations since Fe-bearing inclusions, being brittle in nature with low strain to failure value, will tend to fracture easily, whereas Si-bearing inclusions can bear some load due to their limited ductility.

It should be noted that we made sure that the base of all the pillars shown in Figures (28-30) were part of the inclusion and therefore the properties are that of the pure inclusions. This was confirmed by two methods: (a) after fabrication of the pillars, EDS

was performed at different points at the base of the pillars, and (b) by the observation of the shape of the stress-strain curves obtained by pillar compression. Figure 31 (a-d) shows the SEM images of pillars after deformation along with the stress-strain curves (Figure 31e) for Al_7Cu_2Fe inclusions with Al matrix at the base. It is evident that the deformation behavior of the pillars with matrix at the base is completely different than that of the pillars with only inclusions. Pillars with Al matrix either slipped at the boundary of the inclusion and the matrix or in the Al matrix itself. The stress-strain curves of these pillars show plastic deformation as opposed to the brittle failure of pillars with pure Al_7Cu_2Fe. The stress required for the same strain value decreased dramatically compared to pillars of pure inclusions, although the stress values are higher than that of the pure Al matrix due to the presence of higher strength Fe-bearing inclusions.

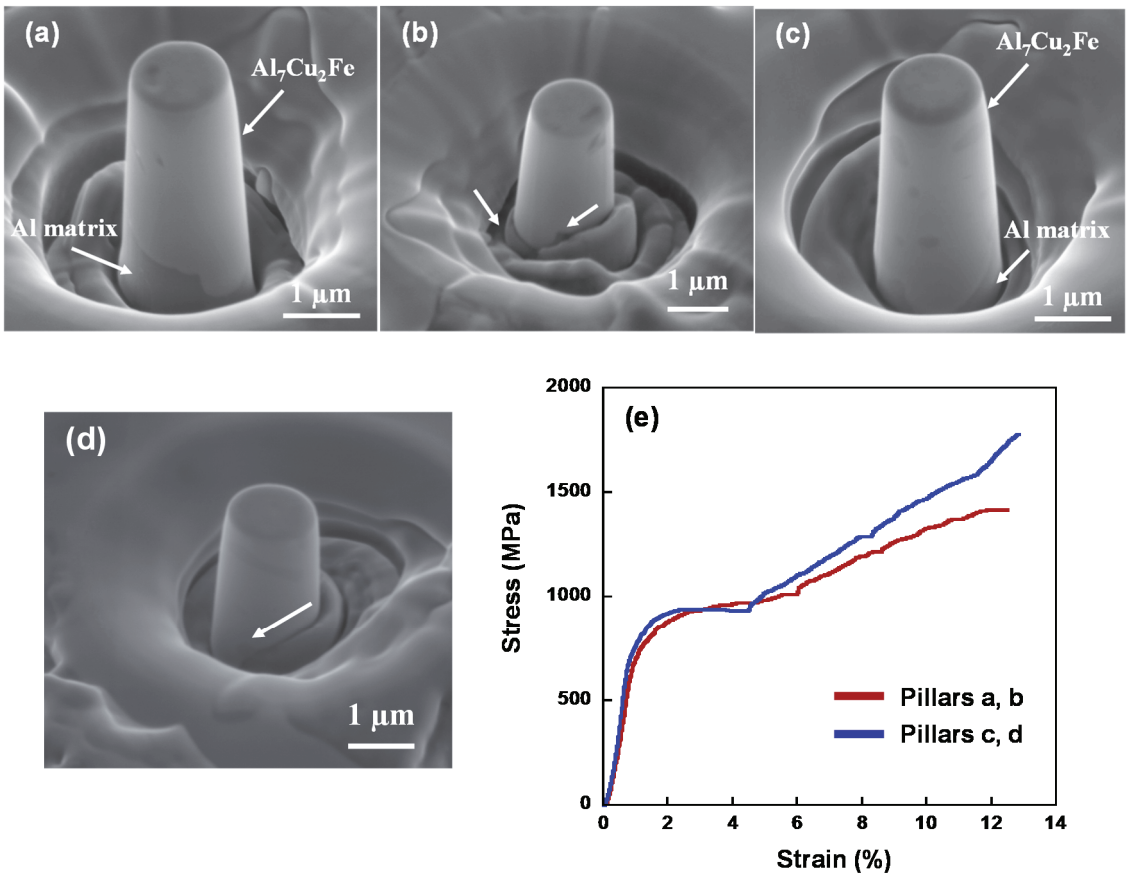

Figure 31. Deformation of Fe-bearing inclusion pillars with Al at the base. (a) and (c) are pillars before deformation. (b) and (d) are images after compression of pillars (a) and (c) respectively. Note that the pillars slipped at the interface or in the Al matrix at the base, (e) stress-strain curves showing the plasticity in the Fe-bearing inclusions due to presence of the Al matrix

Similarly, for Mg_2Si, the deformation is shown in Figure 32 (a-d) and stress-strain curve in Figure 32e. The yield stress values in these cases are also lower compared to the pillars of pure Mg_2Si, but higher than that of the matrix.

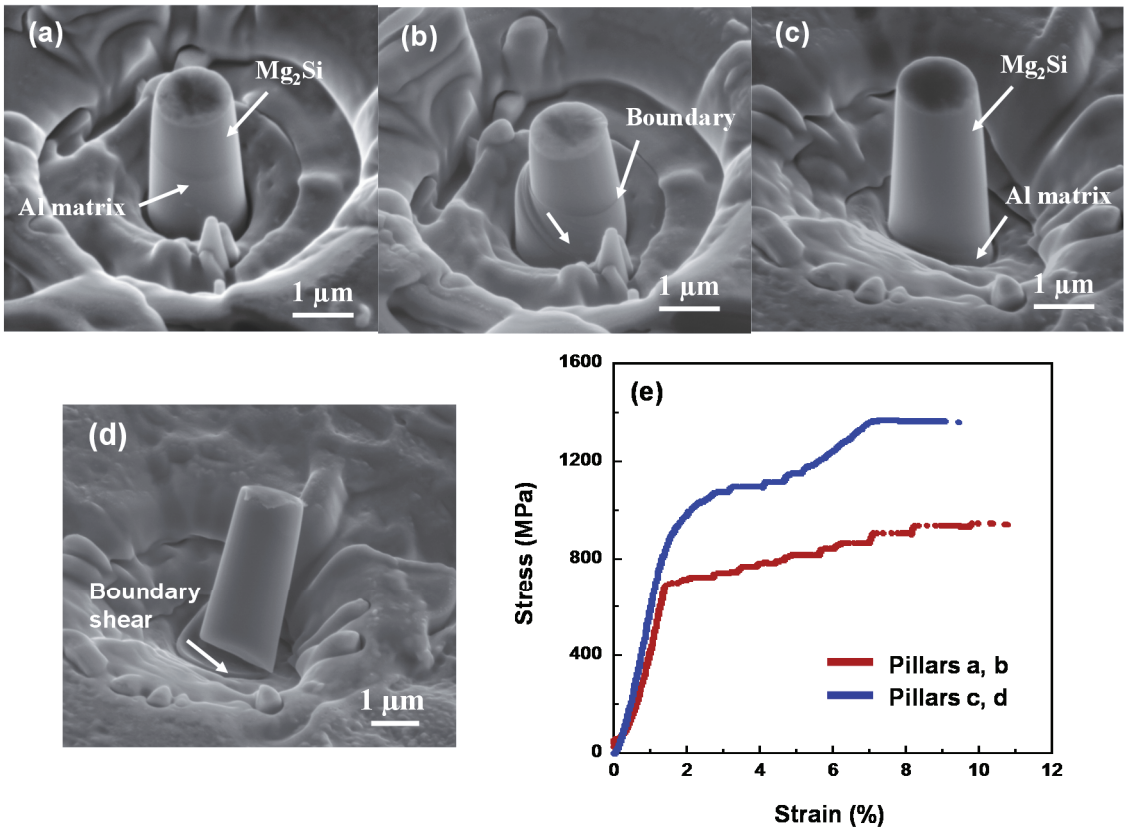

Figure 32. Deformation of Si-bearing inclusion (Mg_2Si) pillars with Al at the base. (a) and (c) are pillars before deformation. (b) and (d) are images after compression of pillars (a) and (c) respectively. Note that the pillars slipped at the interface or in the Al matrix at the base. (e) stress-strain curves showing the decrease in stress values of Si-bearing inclusions due to presence of the Al matrix

In chapter 3, using the X-ray synchrotron tomography, we showed that these inclusions are highly irregular in shape and around 85-90% of the inclusions have volume of less than 50 μm^3. For many materials, it has been shown that the increase in size of the pillars decreases the strength, showing the so called "size effect" phenomenon (Greer, Weinberger, and Cai 2008; Uchic et al. 2004). Due to the irregular shape and small size of the inclusions and also in order to maintain the aspect ratio of ~3, it was practically impossible to fabricate larger size pillars on the inclusions. Most of the pillar

compression studies in literature have been performed on pillars of aspect ratio of 2-4 (Hassan Ghassemi-Armaki et al. 2013; Gu and Ngan 2013), and sometimes even more than 4 (M. C. Liu et al. 2012; Shan et al. 2008). However, aspect ratio of ~3 has been suggested to be a good compromise between buckling and barreling (Hütsch and Lilleodden 2014). Many attempts were made to make large size pillars, however, the base of the inclusions were always the matrix. Even in ~1.3-1.5 μm diameter pillars fabricated in this study, the base of several pillars was of Al matrix, as mentioned above. Moreover, since most of the inclusions are of very small size (~90% of less than 50 μm^3); the results obtained in this study are representative of the size in the actual microstructure, and can be used for modeling purpose as a constitutive behavior of the inclusions.

4.4 Summary

The micropillar compression technique was used to study the mechanical properties of constituent particles (inclusions) in Al 7075 alloys, namely Al_7Cu_2Fe (Fe-bearing inclusions) and Mg_2Si (Si-bearing inclusions). The advantage of the micropillar compression was that the stress-strain curves can be obtained directly from the inclusions in Al alloys, which would not have been possible by conventional methods due to their small size. Iron bearing inclusions had the highest strength followed by Si-bearing inclusions, and then Al 7075 matrix. Al_7Cu_2Fe constituent particles were completely brittle in nature and had compressive failure strength of 2.5 ± 0.2 GPa. Si-bearing inclusions had yield strength of 1.8 ± 0.1 GPa. The knowledge of the mechanical properties of the constituent particles will allow better understanding of bulk deformation behavior of Al 7075 alloys.

CHAPTER 5

3D MICROSTRUCTURAL CHARACTERIZATION OF PRECIPITATES IN AL ALLOYS USING FOUCSED ION BEAM TOMOGRAPHY

5.1 Introduction

Al 7075 alloys are used extensively due to their high strength-to-weight ratio (AlHazaa, Khan, and Haq 2010; Starke and Staley 1996). The microstructure of the alloy at different length scale is shown in Figure 1. The microstructure contains grains, recrystallized grains, and second phase particles. Second phase particles can predominantly be divided into inclusions and precipitates, whose dimensions are on the order of micrometers and nanometers, respectively. These second phase particles are known to affect mechanical and corrosion properties of Al alloys (Speidel 1975; J.-F. Li et al. 2008). Inclusions are known to be formed during casting from impurities.

The nanoscale precipitates are formed when the alloy is either naturally aged or artificially aged following solution heat treatment. The precipitation in AA7075 occurs in the following sequence: supersaturated solid solution → GP zones → η' → η (Viana et al. 1999). Although, the yield strength is the highest for peak-aged temper, it is also more susceptible to stress corrosion cracking than over-aged temper (Goswami et al. 2013). The variation in mechanical and corrosion properties have been attributed to the size, shape, and distribution of precipitates in the alloy microstructure (Sun et al. 2013; Adler and DeIASI 1977). Therefore, in order to understand the mechanical and corrosion properties of the alloy, it is important to perform the three dimensional (3D) microstructural characterization of the precipitates in the alloy.

Several studies have been performed on size and distribution of precipitates in Al alloys (Goswami et al. 2013; Garcia-Garcia et al. 2014; Gjønnes and Simensen 1970; X. Z. Li et al. 1999; Ringer and Hono 2000; Deschamps and Brechet 1998; Engdahl et al. 2002; Stiller et al. 1999; Werenskiold, Deschamps, and Bréchet 2000). To the best of author's knowledge, till date the characterization of precipitates in AA7075 has been performed only in two dimensions (2D). Most of these studies have used transmission electron microscopy (TEM), which provides very high resolution images. However, due to small area considered, the results are not sufficient to be considered a statistically representative sampling. Birbills et al. (Birbilis et al. 2005) used 2D stereology along with TEM to characterize and quantify size of precipitates. Recently, other techniques, such as amplitude-modulated atomic force microscopy (AM-AFM) along with TEM have been used to quantify the precipitate structure (Garcia-Garcia et al. 2014), while differential scanning calorimetry (DSC) (Adler and DeIASI 1977; Zhao et al. 2004; Richard and Adler 1977) and X-ray scattering techniques (Totten and MacKenzie 2003) have been used to study the formation and dissolution of precipitates in Al 7075 alloys. The shape of η' precipitates has been thought to be platelike (Zhao et al. 2004; Au 1996; Feng, Chen, and Ma 2010; Porter, Easterling, and Sherif 2009) whereas, η is plate or rod (Goswami et al. 2013; Zhao et al. 2004; Au 1996; Feng, Chen, and Ma 2010). The size of η and η' precipitates from all these studies fall in the range of 10-270 nm.

Experimental techniques for 3D microstructural characterization include atom probe tomography (APT) (Miller and Kenik 2004), electron tomography (Midgley and Dunin-Borkowski 2009), focused ion beam (FIB) tomography (Bansal et al. 2006), serial sectioning followed by optical microscopy (Sidhu and Chawla 2004), and X-ray

tomography (Stock 1999). Serial sectioning followed by optical microscopy and X-ray tomography can be used to study large volumes of material, resulting in statistically significant information, but due to limited resolution, these techniques cannot be used for precipitates. 3D atom probe tomography and electron tomography provide very high resolution images, but only very small volumes can be analyzed. Although destructive in nature, focused ion beam (FIB) tomography is well suited to study the precipitates in Al alloys. It provides adequately high resolution images along with the sufficient volume to provide statistical information. FIB tomography has already been successfully utilized to characterize the microstructure in Al-SiC nanolaminates (D. R. P. Singh, Chawla, and Shen 2010), Pb-free solders (Dudek and Chawla 2010; Yazzie et al. 2012), and superalloys (Uchic et al. 2006; Holzapfel et al. 2007).

The present work is the follow up of our recent published work on correlative tomography (Merkel et al. 2014). It was shown that next generation of the Atlas software (Carl Zeiss) can extend navigation capabilities into the third dimension, enabling an array of correlative workflows across several length scales, modalities and instrumentation platforms. Non-destructive XRM (X-ray microscopy) data acquisition was used to identify inclusions (larger in size as shown in Figure 1) and associated pores, and then to inform and automate FIB-SEM (Focused ion beam-scanning electron microscopy) tomography at the same area to visualize precipitate structures (very small in size). This approach may be extended to multiple FIB-SEM tomography sites, greatly expanding FIB utilization via the navigation workflow of Atlas 5 and XRM data. Furthermore, the preceding non-destructive XRM analysis may, importantly, be extended to time-dependent (4D) or *in situ* conditions to quantify the evolution of a structure (processing,

aging, corrosion, etc.) prior to inspection by FIB-SEM tomography at defined locations. we have visualized and quantified the microstructure of inclusions and pores in 3D and have also obtained their mechanical properties from the same plate of AA7075 in chapter 3 and chapter 4, respectively. The aim of this work was to visualize and quantify the structure of precipitates in 3D in Al 7075 alloys which has not been attempted before.

5.2 Materials and Experimental Procedure

The material used in this study was a commercially available 7075-T651 aluminum alloy (5.63 Zn, 2.45 Mg, 1.55 Cu, 0.045 Si, 0.18 Fe, 0.0077 Mn, 0.19 Cr, 0.0037 Ni, 0.049 Ti, and rest Al) rolled to a 2.5 cm thickness (Alcan rolled product, supplied by Dix Metals Inc). A small specimen (~ 3 mm x 3 mm x 4 mm) was cut near surface of the rolled plate. The specimen was polished to a 1 μm diamond finish and then to a final finish of 0.05 μm colloidal silica.

Correlative tomography using a combination of X-ray microscopy (XRM) and FIB-tomography was performed on polished sample. The 3D XRM datasets were loaded into ZEISS Atlas 5 for alignment and registration with the 2D surface SEM images (online acquisition), upon which the XRM dataset was used to navigate the FIB-SEM to the precise region for FIB-tomography. The details of data acquisition using X-ray microscopy have been provided in recently published research (Merkel et al. 2014). Atlas FIB-SEM tomography was acquired on a ZEISS Crossbeam 540 utilizing 10 nm isotropic voxel size and an EsB detector with SEM voltage of 1.5kV. The collected FIB-SEM volume was approximately 18 μm x 8 μm x 7 μm. With the 3D Tomography option in ZEISS Atlas 5, the FIB was used to mill a geometric pattern of marks into the sample

surface before the FIB-SEM tomography run was executed. During the tomography run, the FIB exposed and milled a cross-section of the sample, perpendicular to the sample surface. Simultaneous with this milling, the SEM imaged the cross-section face, including a cross-section of the marks previously prepared on the sample surface. From the position and configuration of these marks, the software was able to accurately measure both the position of the sample, and the rate of erosion of the sample cross-section. This information was used to predictively correct the positions of the both the FIB mill and the SEM imaging to correct for sample drift and variability in the sample erosion rate. In this fashion, a sequence of well aligned cross-section images was produced, with consistent, measured, slice thicknesses.

After acquisition, the FIB-SEM image stack was aligned and cropped in ZEISS Atlas 5 before exporting for further 3D visualization and quantification. The fine alignment of the image stack was calculated by performing a cross-correlation between adjacent slices in the stack over a user defined sub-region. The information from this cross-correlation was used to produce small corrections in the X-Y position of each slice to improve the over-all alignment of the stack.

The stack of aligned grayscale images were analyzed and segmented using ImageJ (Bethesda, MD) and MIMICS (Materialise, Ann Arbor, MI). For the segmentation of grains, inclusion and pore, an anisotropic diffusion filter was first used to reduce the noise to signal ratio while preserving edges, followed by segmentation using a combination of livewire (MIMICS, Materialise, Ann Arbor, MI) and ImageJ.

To segment the precipitates, the stack of images was first filtered using both a bandpass filter and anisotropic diffusion filter, and then was segmented using

conventional thresholding in ImageJ. The details of segmented process is given in next section. The segmented images were imported into Avizo® Fire (VSG, Burlington, MA) for 3D reconstruction and visualization. Quantitative analysis of the size, shape and distribution was performed using Matlab and Avizo® Fire.

5.3 Results and Discussion

Figure 33 shows a back scattered electron (BSE) image of one of the 2D slices of AA7075 obtained using focused ion beam (FIB). Grains are clearly visible in the image due to channeling contrast. Also, visible is an Mg_2Si inclusion and pore associated with it, which is morphologically different from the surrounding grains (no faceting). The pores are believed to be formed during rolling (Eric Maire et al. 2006; B. J. Connolly et al., others 2006). The small bright features along the grain boundaries and inside grains are precipitates. Figure 34a shows 3D rendering of the studied volume and Figure 34b shows the cropped volume showing the pore associated with the inclusion.

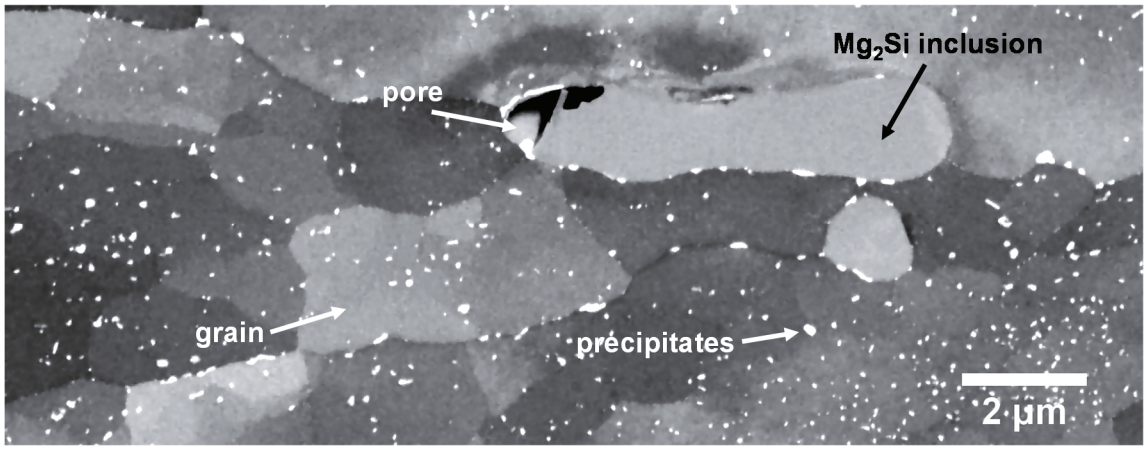

Figure 33. 2D slice of AA7075 obtained from FIB tomography showing grains, inclusion, pore associated with the inclusion, and precipitates

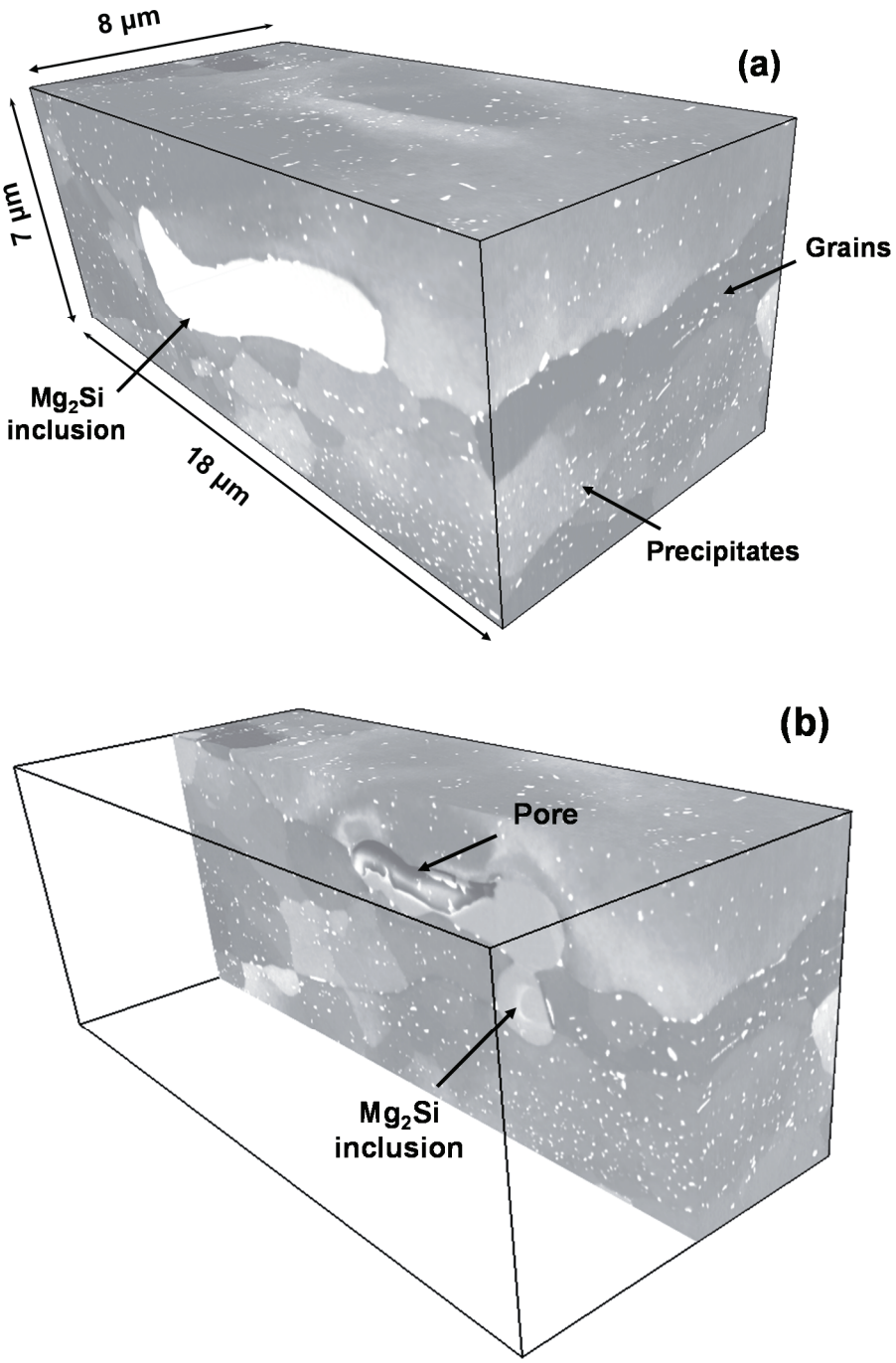

Figure 34. (a) Whole 3D volume showing grains, inclusion and precipitates, and (b) cropped 3D volume showing pore associated with the Mg_2Si inclusion

Figures 35 (a-e) shows the steps for segmentation of grains, inclusions and pore. Figure 35a is a 2D slice obtained from FIB tomography. Figure 35b shows the filtered image after application of anisotropic diffusion filter showing reduction in noise to signal ratio. Figures 35 (c-e) shows the use of livewire technique in MIMICS for segmentation. The mathematics behind the livewire technique have been described elsewhere (Padilla et al. 2012; J. J. Williams et al. 2010). This technique uses contour line (livewire line), which uses the sharp gradient in gray scale observed between two grains. The technique is semi-automatic since user selects the number of seed points on the livewire line and can also force the livewire line to pass through the boundaries where sharp gradient in gray scale is not observed (we also forced the livewire line in the cases where a very sharp gradient in gray scale was not observed between two grains). The contour is drawn on two orthogonal planes after which the software automatically contours the grain on the third orthogonal plane, as shown in Figure 35c. The magnified version of Figure 35c is shown in Figure 35e, where perpendicular lines, which are contour line along grain boundary in two orthogonal planes, can clearly be seen in the third orthogonal plane. The final result is the 3D mask of the grain, as shown in Figure 35d.

Figure 36 shows the steps to segment precipitates. Due to very small size of precipitates, the livewire technique was not suitable for segmentation and therefore conventional thresholding technique was used. The gray scale values of some of the grains were near to gray values of the precipitates creating problem in thresholding. Therefore, the stack of images was first imported into ImageJ and filtered using band pass filter. This operation increased the contrast of the precipitates and suppressed the background, as shown in Figure 36b. The stack of images was then filtered by an

anisotropic diffusion filter to reduce noise to signal ratio (Figure 36c). The combination of bandpass filter and anisotropic diffusion filter resulted in good gray scale images for thresholding and the result is shown in Figure 36d.

Figure 37 shows a 3D rendering obtained using Avizo® Fire of (a) grains, inclusion and pore, (b) Precipitates, and (c) all constituents. From the 3D rendering, it seems that grains are spherical in nature and the precipitates are uniformly distributed in the studied volume. Figure 38 shows the volume and sphericity distribution of the segmented grains and Table 7 shows the corresponding quantitative analysis. A total of 25 grains were segmented to obtain quantification on grains.

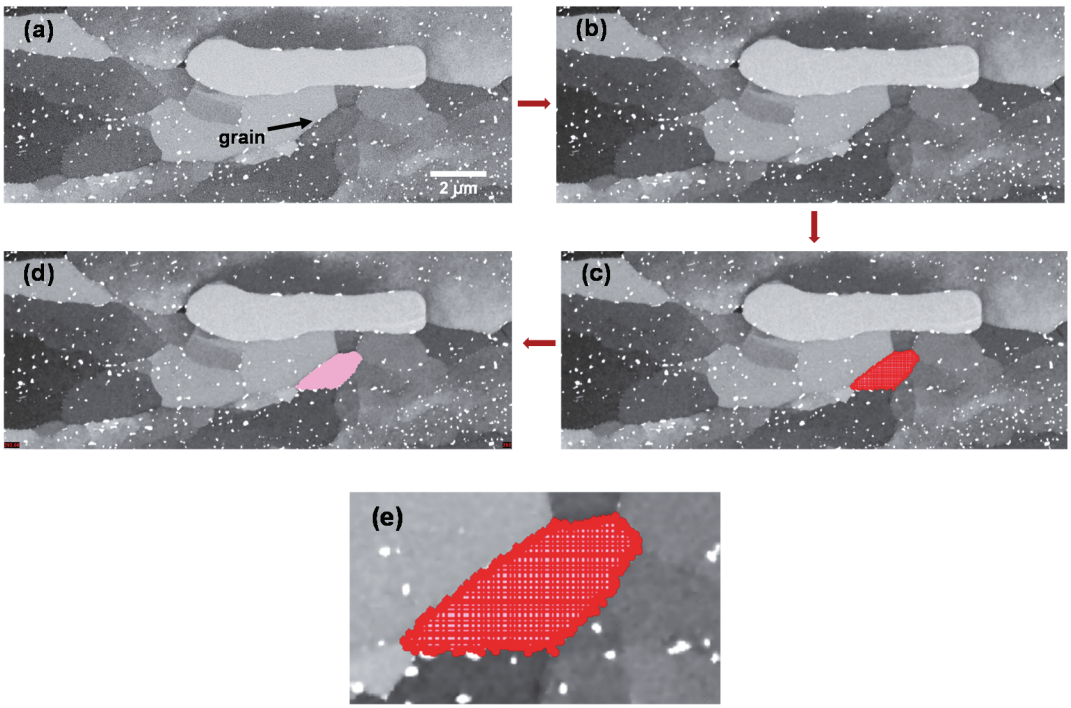

Figure 35. Step wise segmentation of grains, pore and inclusion (a) gray scale image, (b) gray scale image after anisotropic diffusion filter in ImageJ, (c) application of livewire technique to a grain in MIMICS, and (d) corresponding segmented grain. Figure (e) shows the magnified version of the grain in (c)

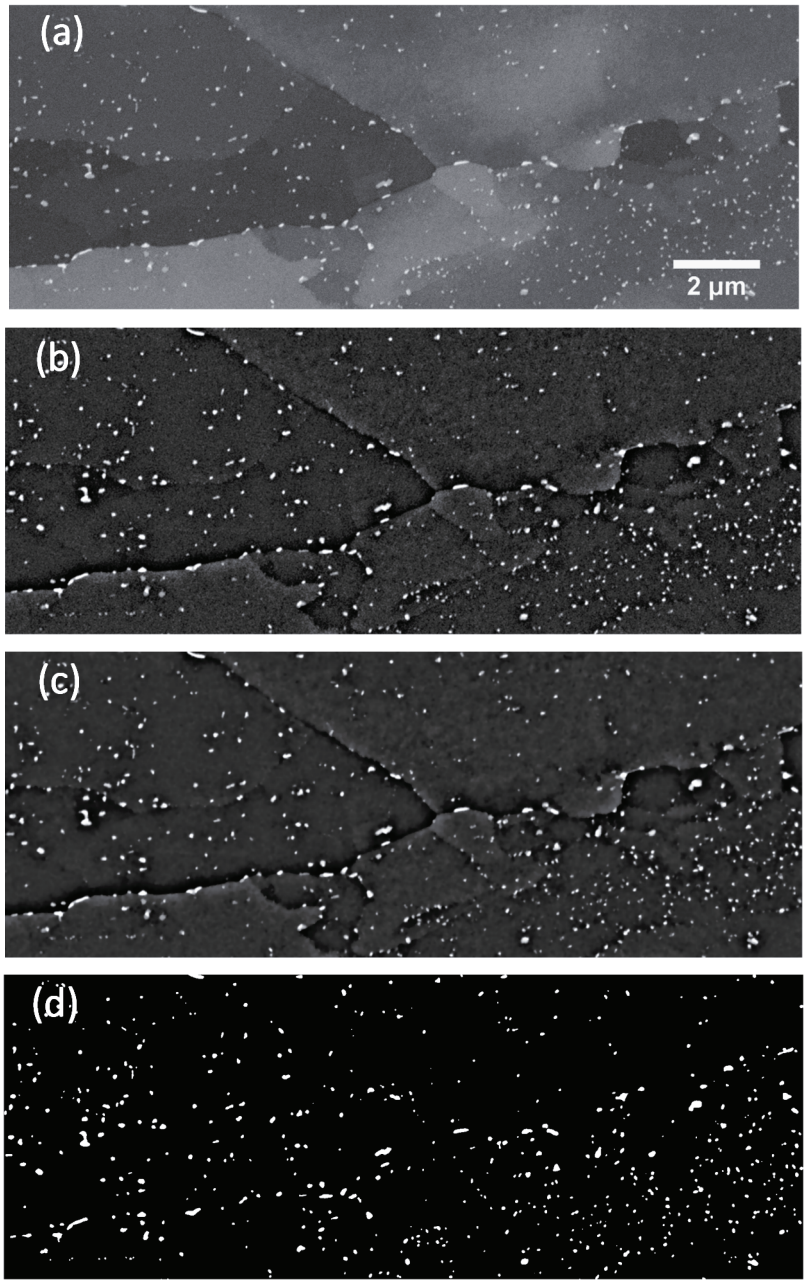

Figure 36. Segmentation of precipitates (a) gray scale image obtained from FIB tomography, (b) image after application of band-pass filter, (c) image with very low noise to signal ratio after anisotropic diffusion filter, and (d) binary white and black image from thresholding in ImageJ.

The sphericity (Ψ) of grain is defined as (Ling Jiang et al. 2011):

$$\Psi = \left(\frac{36\pi V_g^2}{A_g^3} \right)^{1/3} \quad (5)$$

Where, V_g and A_g are the volume and surface area of grains, respectively. The volume and surface area of the grains were calculated in Avizo® Fire. As the sphericity approaches a value of one, the shape of the grain approaches to a perfect sphere. The sphericity distribution and the average value of 0.73 indicate that the grains are not highly elongated as expected due to rolling indicating that these grains are recrystallized grains. It has been shown that the variation of solute concentration, deformation condition, solutionization temperature etc. leads to variation in recrystallization structure of hot rolled plate (Root 2010). It is known that the hot rolling process increases the energy of the system by increasing the stored strain energy and therefore original grains are replaced by low energy recrystallized grains (Root 2010). Although Cr is added in the alloy, which can form dispersoids ($Al_{12}Mg_2Cr$) (Starke and Staley 1996) and inhibit recrystallization, in our case we believe that the amount of rolling led to a high stored stain energy which was sufficient to overcome the effect from dispersoids and therefore grains recrystallized. The average grain size of the recrystallized grains is 2.9 µm. The volume distribution is skewed towards smaller volume and therefore skewness has been reported in the case of volume of grains. Skewness is a measure of the degree of asymmetry in a statistical distribution. Positive value of skewness indicates that the mean is higher than the median, while negative skewness value indicates the median is higher than the mean.

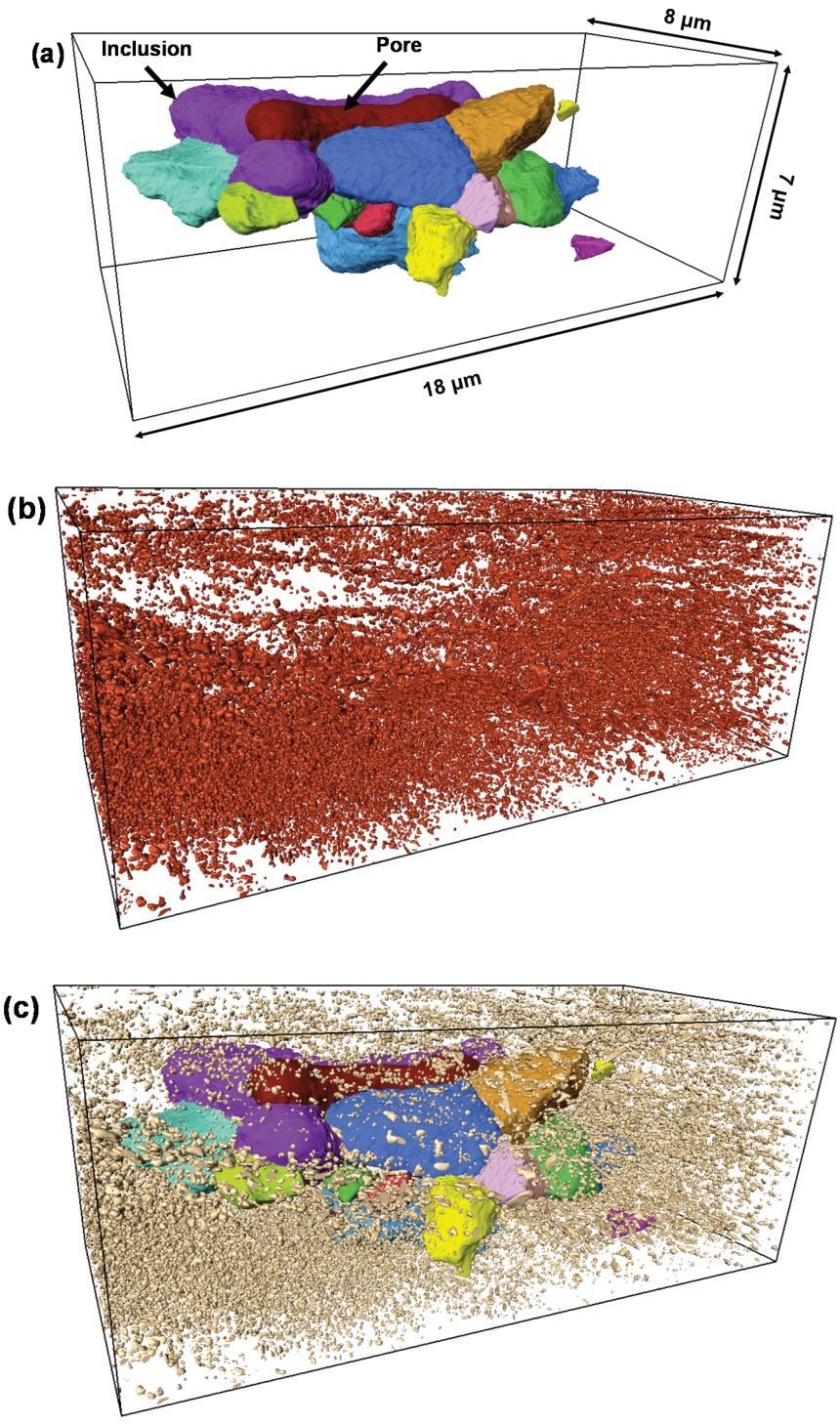

Figure 37. 3D rendering of (a) grains/inclusion/pore, (b) precipitates, and (c) combined grains and precipitates

Table 7. Quantitative analysis of grains in Al 7075 alloys

	Volume (μm^3)	Max. Feret Diameter (μm)	Sphericity
Mean	4.3 (Skewness: 1.5)	2.9 ± 1.38	0.73 ± 0.05
max	18.2	6.3	0.84

The volume fraction of precipitates was ~ 2.37%. To remove the noise, the precipitates having a volume greater than 1000 nm^3 (corresponding to 1x1x1 voxels) were taken into account for the measurements. Figure 39 shows the volume and size distribution of precipitates and Table 8 summarizes the quantitative analysis. The shape of the precipitates was given by maximum feret diameter and aspect ratio. Feret diameter is defined as the distance between two parallel tangents of the particle. Maximum feret diameter is the maximum of all feret diameters. Maximum and minimum feret diameters were obtained from Avizo® Fire. The aspect ratio is defined as the ratio of maximum feret diameter (length) to minimum feret diameter (width).

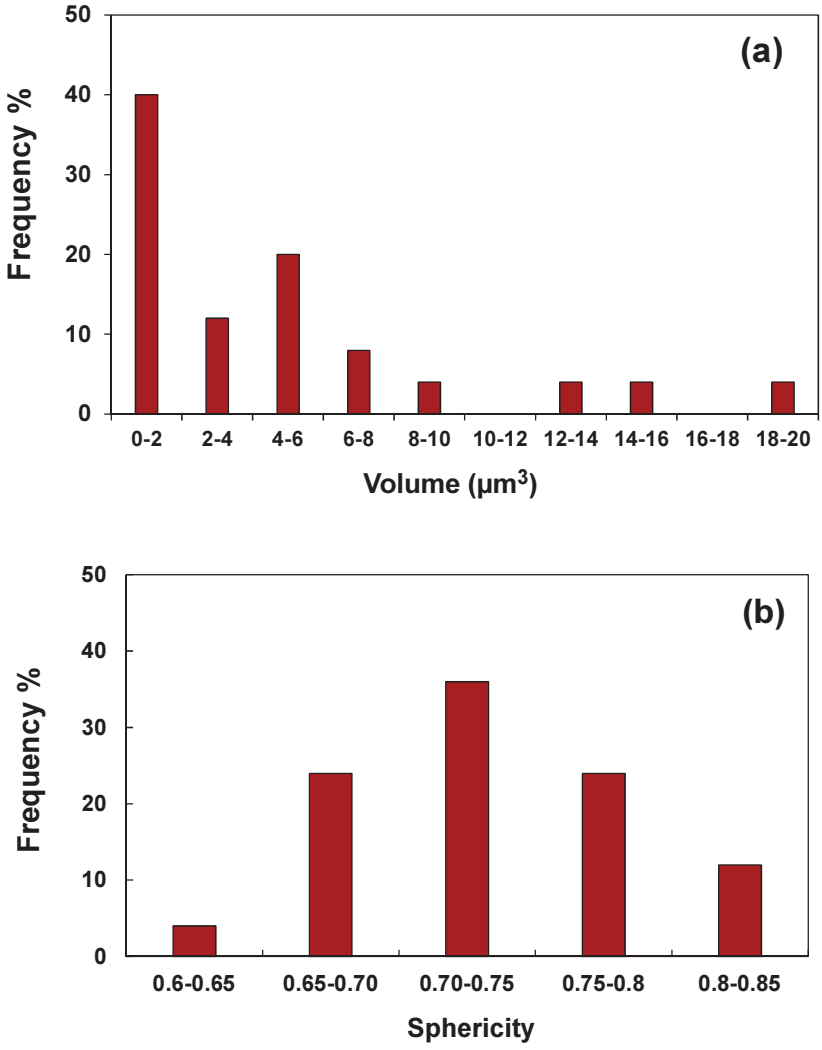

Figure 38. (a) Volume distribution of grains, and (b) sphericity distribution of grains

Figures 39(a-c) show that the frequency distributions of volume, aspect ratio, and maximum feret diameter are highly skewed with higher frequency being mostly associated with smaller values. The same type of skewed distribution for equivalent diameter was observed by Garcia et al. using TEM and AFM (Garcia-Garcia et al. 2014).

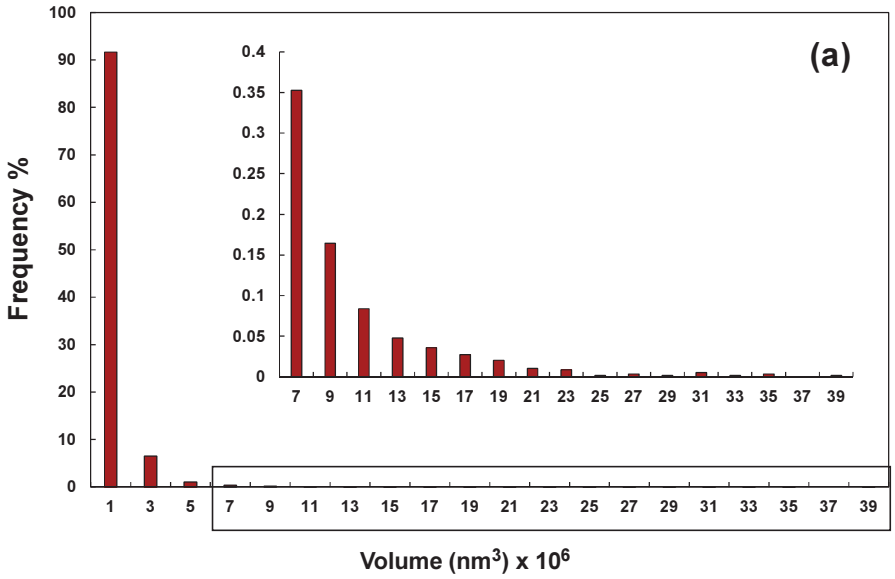
(a)
Frequency %
Volume (nm3) x 10^6

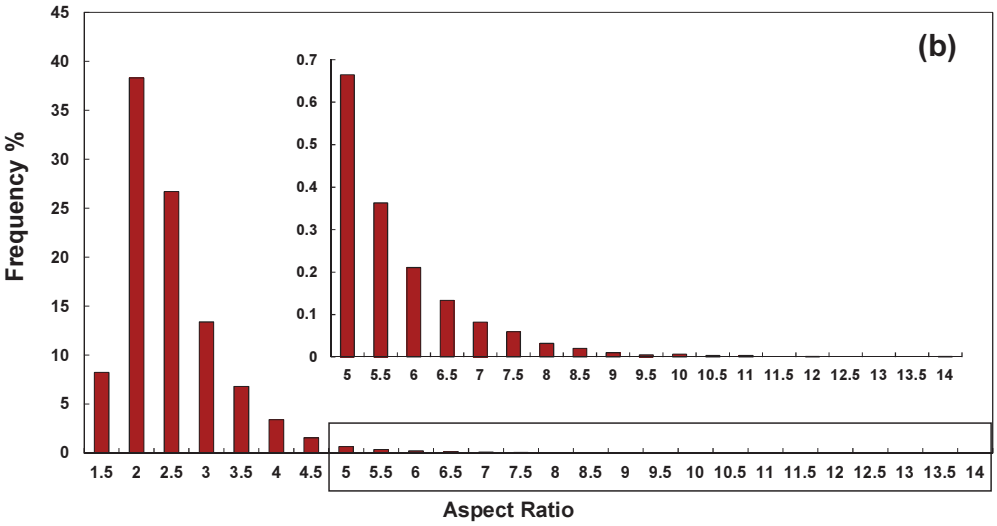
(b)
Frequency %
Aspect Ratio

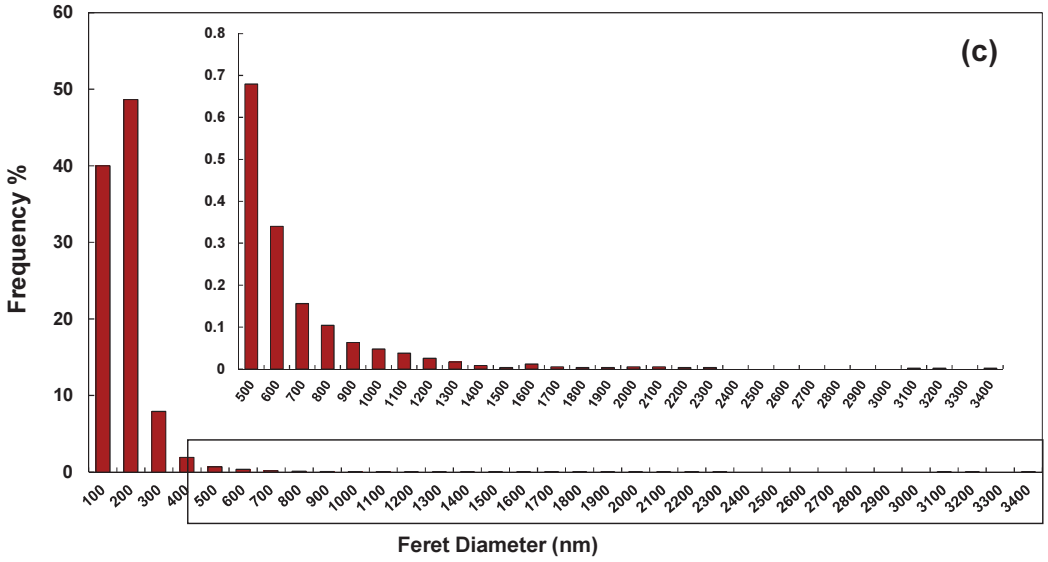

Figure 39. (a) Volume distribution, (b) aspect ratio, and (c) maximum feret diameter distributions of precipitates in AA7075. The insert plots are the boxed part of the axis

A closer look at 3D rendering of precipitates (Figure 37) indicated that the precipitates with higher feret diameter and volume might have been associated with grain boundaries and therefore the precipitates were separated into grain boundary precipitates and inside the grains, as shown in Figure 40. Figure 41 shows the magnified version of selected four grains showing the precipitates size and shape on the grain boundaries and inside the grains. It is clear from the figure that the grain boundaries precipitates are larger in size than the precipitates inside the grains. Precipitates with rod, plate and spherical shape can be seen in Figure 41. These precipitate morphologies have also been observed in other works (Zhao et al. 2004; Au 1996; Feng, Chen, and Ma 2010; Porter, Easterling, and Sherif 2009). Many precipitates appear to have other irregular shapes compared to the idealized shapes mentioned above. We believe that this might be due to

variation in the local growth conditions due to grain orientation and also due to their interaction during growth.

Table 8. Quantitative analysis of precipitates in AA 7075-T651

	Mean	Max	Skewness
Volume (nm^3)	$4.2x10^5$	$3.7x10^7$	11.61
Max. feret diameter (nm)	131.26	3356	7.50
Aspect ratio	2.24	13.58	2.19

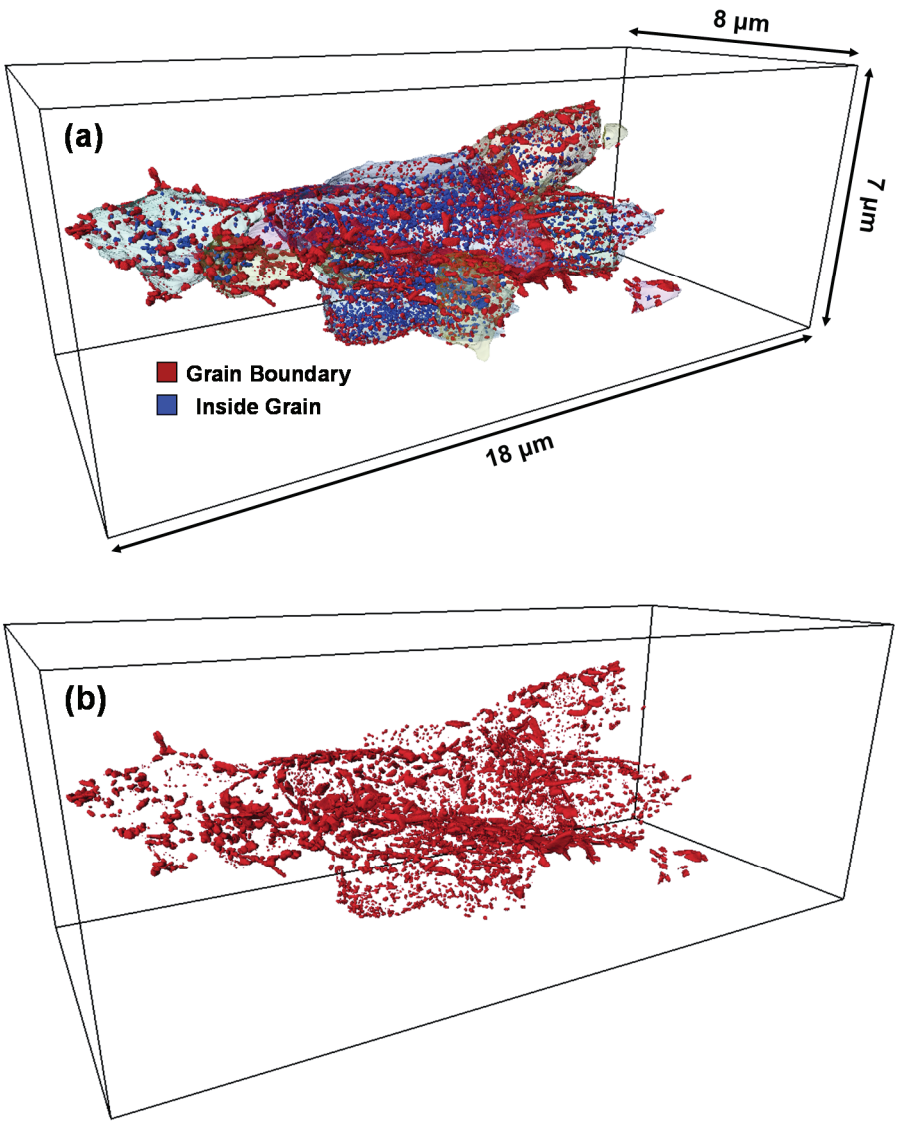
8 µm
(a)
7 µm
Grain Boundary
Inside Grain
18 µm
(b)

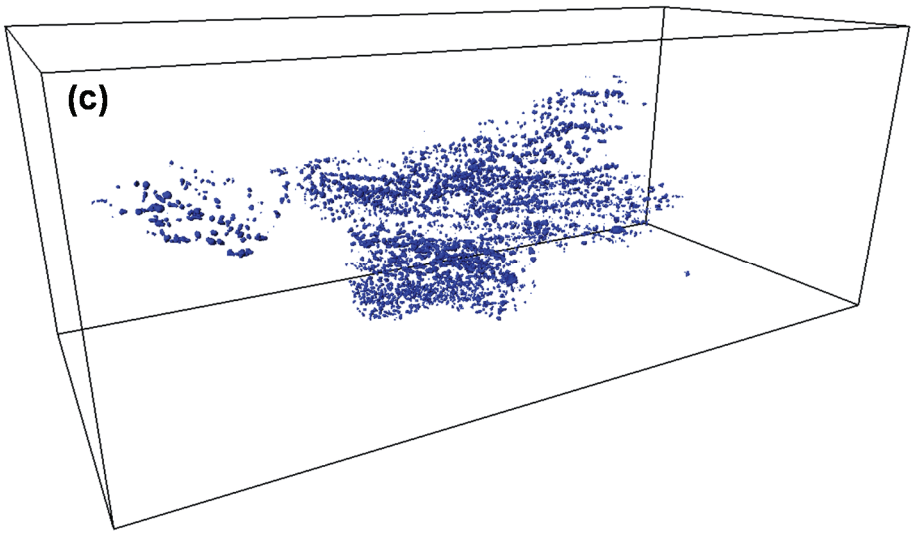

Figure 40. 3D rendering of (a) grains with precipitates, (b) precipitates on grain boundaries, and (c) precipitates inside grains

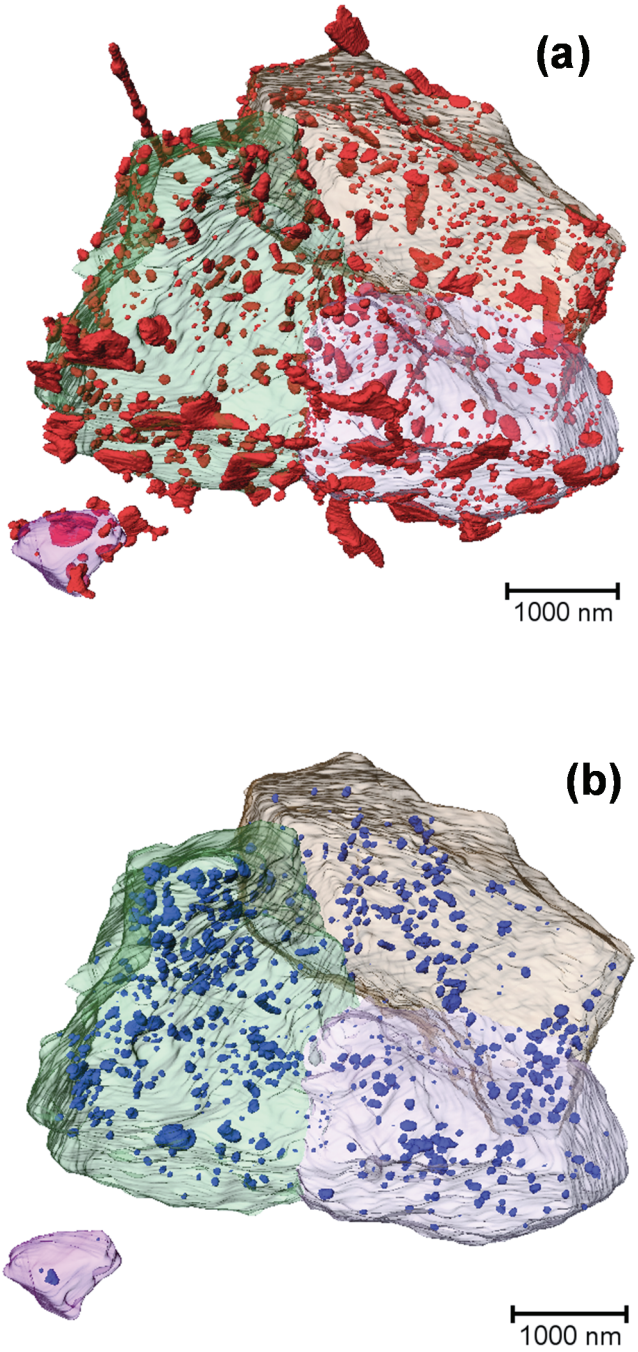

Figure 41. Magnified images of (a) grain boundary precipitates, and (b) precipitates inside the grains. Images showing that the size and volume of the grain boundary precipitates are higher than precipitates inside grains

Quantitative analysis was performed to characterize the size and shape of the precipitates on the grain boundaries and inside the grains, as in shown in Table 9. It should be mentioned here that the precipitates on the boundary between grains and the Mg_2Si inclusion have been included in grain boundary precipitates. The average volume of precipitates on the grain boundaries is about 2.5 times the average volume of precipitates inside the grains which is also evident from the Figure 41. Interestingly the skewness values for precipitates both inside and on grain boundaries are high i.e. ~ 6.9, indicating that the volume distribution is skewed (towards lower volume), as shown in Figure 42. It is well known that grain boundaries and interphase boundaries are one of the most preferable sites for heterogeneous nucleation in age-hardening aluminum alloys since they provide low activation energy barrier for nucleation of precipitates (Porter, Easterling, and Sherif 2009; Abbaschian and Reed-Hill 2008). Nucleation of precipitates can also occur on dislocations and vacancies present in the matrix, however, the activation energy barrier for these sites are higher than the grain/phase boundaries and therefore there is a time lag of aging response between grain boundaries and matrix. Due to early nucleation and faster growth (easy diffusion) at grain boundaries, the precipitates on the grain boundaries and on the phase boundaries are larger in size than the precipitates in the matrix.

Table 9. Comparison of size and shape of precipitates on grain boundaries and inside the grains

	Mean		Max		Skewness	
	Inside grains	GB	Inside grains	GB	Inside grains	GB
Volume (nm^3)	$2.9x10^5$	$7.7x10^5$	$9.5x10^6$	$3.7x10^7$	6.83	6.90
Max. feret diameter (nm)	114.4	145.6	923	3356	2.67	6.60
Aspect ratio	2.35	2.72	7.62	13.58	1.91	2.06

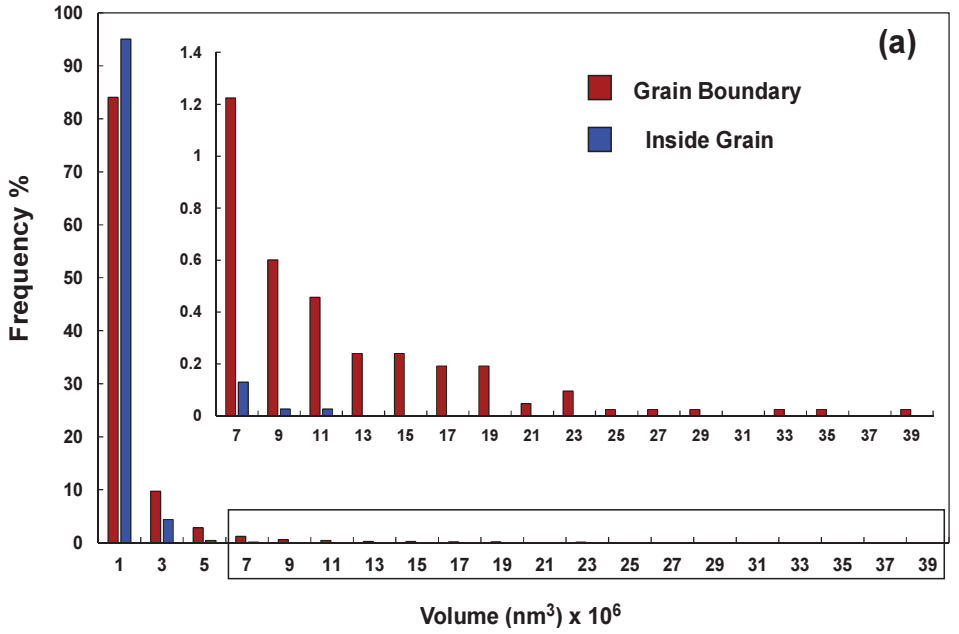
(a)
Grain Boundary
Inside Grain
Frequency %
Volume (nm3) x 10^6

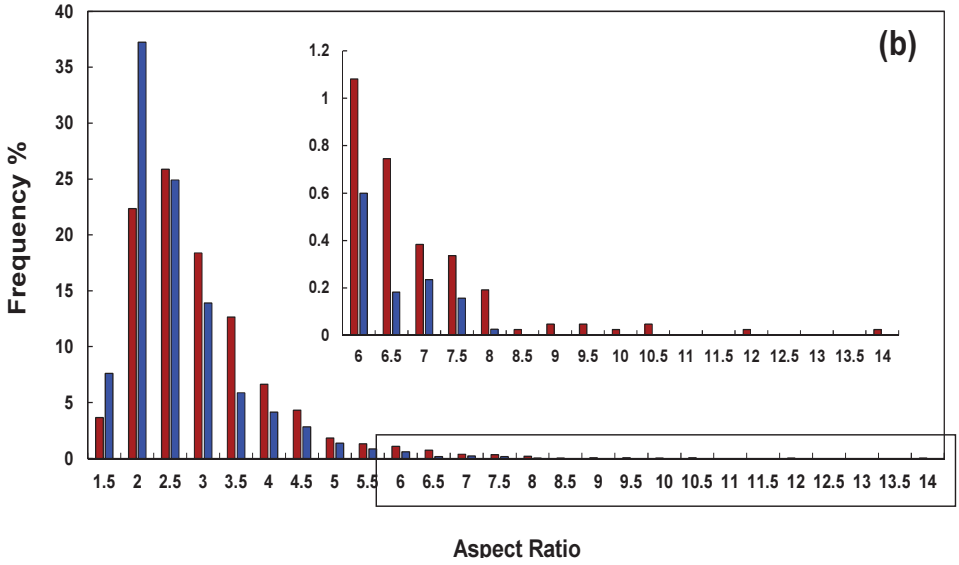
(b)
Frequency %
Aspect Ratio

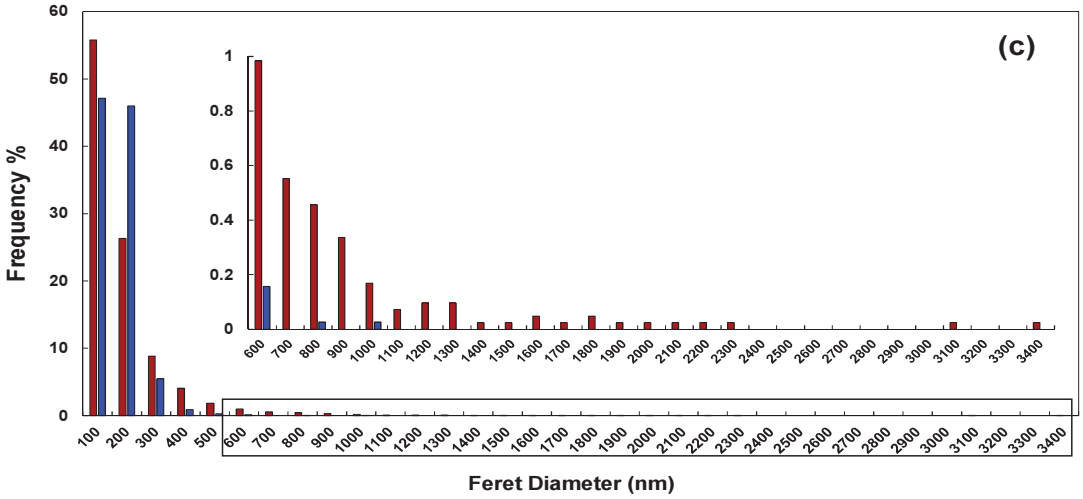

Figure 42. 3D Precipitates size and shape distribution on grain boundaries and inside the grains (a) volume distribution, (b) feret diameter, and (c) aspect ratio. The insert plots are the boxed part of the axis

The average values of feret diameter and aspect ratio of precipitates on grain boundaries are higher than the precipitates inside grains. Although the maximum value of feret diameter for the precipitates on the grain boundaries is much higher than the precipitates inside the grains (~ 3.5 times), the average values are slightly higher for grain boundary (145 nm vs 114 nm). This can be attributed to the higher skewed values of the distribution for grain boundary precipitates, in which about 55% of the precipitates have maximum feret diameter of less than 100 nm. Aspect ratio shows the same types of distribution, although the frequency of aspect ratio for GB precipitates for high aspect ratios are more than precipitates inside grains.

In peak-aged condition, the precipitates are mostly a combination of η and η' (Viana et al. 1999; Garcia-Garcia et al. 2014). Over the years there has been several studies on the composition and structure of precipitates. It was believed that the composition of precipitates is $MgZn_2$ (Garcia-Garcia et al. 2014; Birbilis et al. 2005;

Richard and Adler 1977; Totten and MacKenzie 2003). However, it has now been shown that although the crystal structure of precipitates in cu containing 7xxx series aluminum alloys is same as $MgZn_2$, the composition is not exactly the same. In fact, the substitution of Cu and Al with Zn atoms occur during aging leading to the composition as $Mg(ZnCu)_2$ and $Mg(Zn,Al,Cu)_2$ (Goswami et al. 2013; Marlaud et al. 2010). Without discussing the composition, we will denote precipitates as combination of η and η' in this paper.

As shown in Figure 43, the interface of Mg_2Si inclusion and grains were also preferred site for nucleation of precipitates. It should be noted here that a part of a single inclusion was taken into consideration for quantification because obtaining FIB tomography data of these large size inclusions is extremely time consuming. Therefore, the data set from this single inclusion may not be representative of all inclusions. Although the statistics of the precipitates at the interface is not complete, few points can be made from the limited data. The mean values of the volume, feret diameter and aspect ratio are 1.2×10^{-6} nm^3, 200 nm and 2.71, respectively. The distributions of volume, maximum feret diameter and aspect ratio are skewed, as shown in Figure 44. The volume and feret diameter values are higher than precipitates inside the grains and also precipitates on grain boundaries indicating that the interfaces are more preferential sites for nucleation of precipitates than GB and inside grains, however, more quantification is required to confirm the hypothesis.

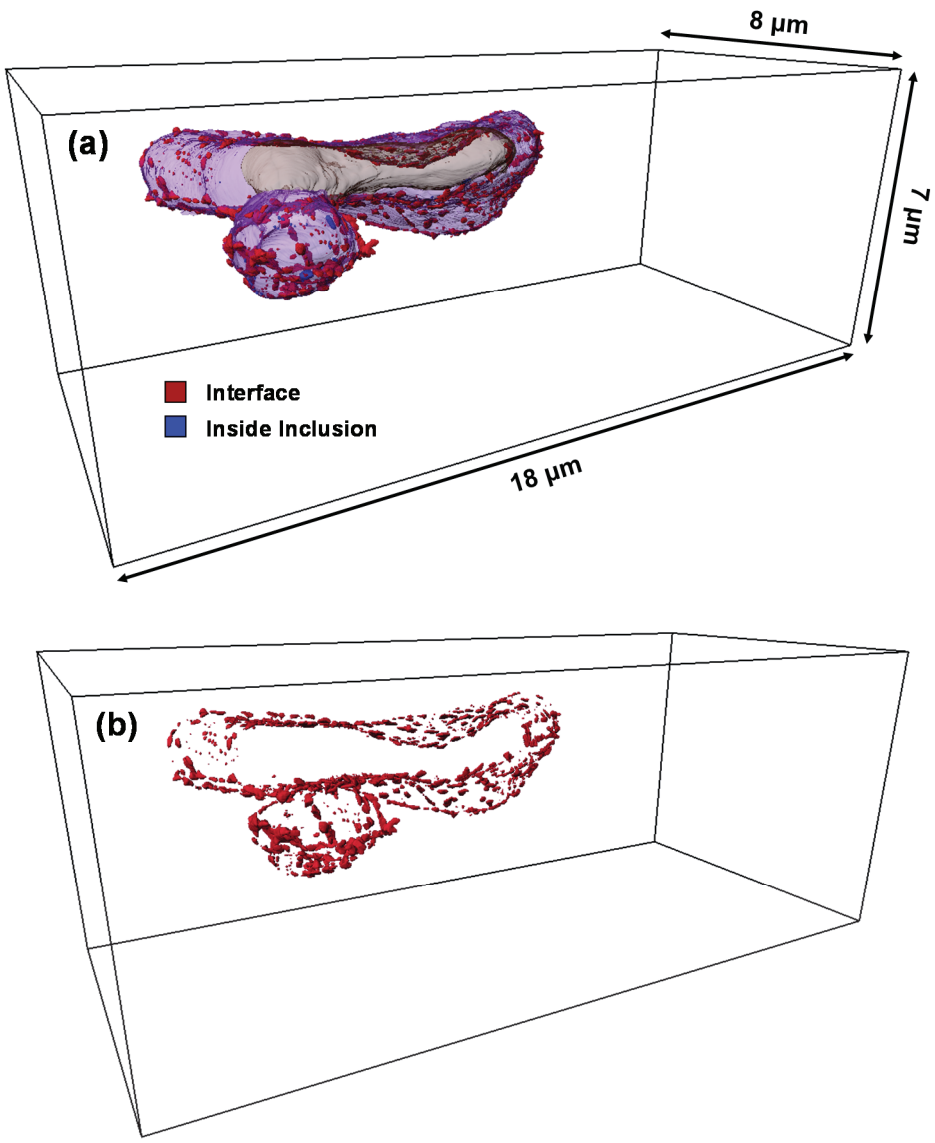

Figure 43. 3D rendering of (a) inclusion/pore with precipitates, (b) precipitates on inclusion boundary

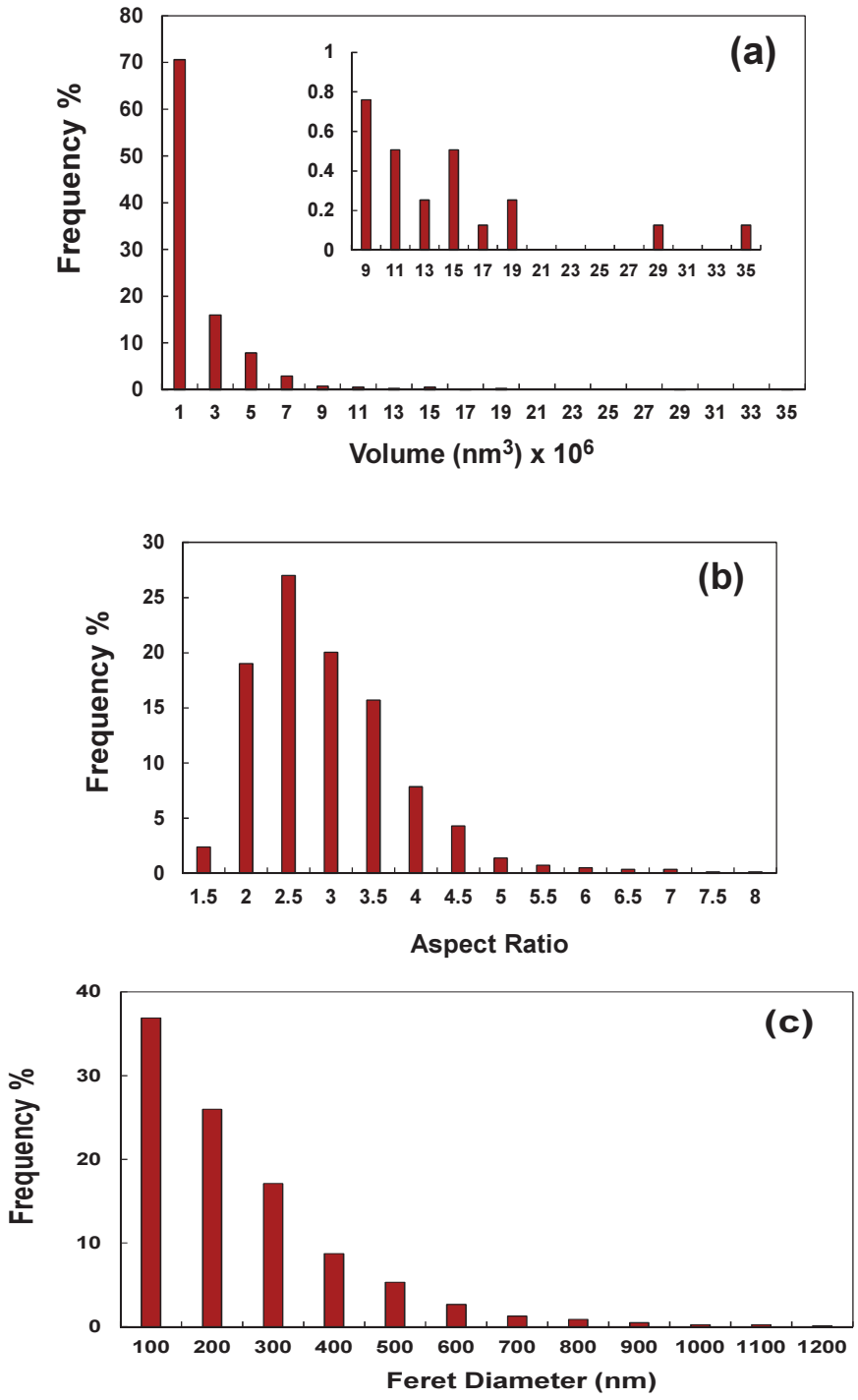

Figure 44. 3D Precipitates size and shape distribution on interface between grains and inclusion (a) volume distribution, (b) feret diameter, and (c) aspect ratio

5.4 Summary

FIB tomography was used to visualize and quantify the grains and precipitates in 7075-T651 aluminum alloys in 3D, after localization of a region of interest via XRM. The shape of the recrystallized grains was approximately spherical with sphericity and maximum feret diameter values of 0.73 ± 0.05 and 2.9 ± 1.38 μm, respectively. The volume fraction of the precipitates in 7075-T651 aluminum alloy was found to be ~ 2.37%. The visualization and quantification of the precipitates showed that the precipitates with large volume are associated with grain boundaries (average value ~ $7.7x10^5$ nm^3) and precipitates inside the grains have relatively small volume (average value ~ $2.9x10^5$ nm^3). The feret diameter and aspect ratios of precipitates on grain boundaries are also higher than precipitates inside the grains.

CHAPTER 6

IN SITU INVESTIGATION OF HIGH HUMIDITY STRESS CORROSION CRACKING OF 7075 ALUMINUM ALLOY BY THREE DIMENSIONAL (3D) X-RAY SYNCHROTRON TOMOGRAPHY

6.1 Introduction

Al 7075 alloys are used extensively due to their high strength-to-weight ratio (Starke and Staley 1996). However, they are susceptible to stress corrosion cracking (SCC) and show a significant increase in crack growth rate in the presence of moisture, especially in the peak-aged and under-aged condition (Speidel 1975; Holroyd and Scamans 2011). Hydrogen embrittlement has been attributed as a possible mechanism for this increase in crack growth rate (Holroyd and Scamans 2011; Burleigh 1991).

Several studies have looked at the crack growth behavior of aluminum alloys. Discontinuous surface cracks (crack jumps) were observed during stress corrosion cracking of aluminum alloys (J. Zhang et al. 2011). These discontinuous surface cracks have also been observed in steel during SCC (Masuda 2007; Qiao et al. 2011). It was suggested that the cracking is discontinuous where surface cracks nucleate in front of the main crack, grow separately and then combine with the main crack (J. Zhang et al. 2011; Qiao et al. 2011). Many studies have used surface measurements (using optical techniques, for example) to quantify SCC behavior (Dorward and Hasse 1979; Brain J. Connolly et al. 2003; Arnold et al. 2012). This approach may be inaccurate since the

crack growth behavior in the interior of the specimen and at the surface may be quite different due to difference in stress states (M. Meyers, K. K. Chawla 2008).

It is clear that a thorough understanding of the cracking behavior in SCC requires a quantification of the crack growth behavior in three dimensions. Furthermore, the experiments must be carried out *in situ* to verify whether the "crack jumps" are indeed jumps. X-ray tomography is an excellent technique to study the behavior of materials under mechanical loading in 3D and 4D (the fourth dimension here is time). In particular, *in situ* mechanical testing is more promising where visualization and quantification of the microstructure changes can be performed with time. *In situ* experiments under tension (J. J. Williams et al. 2011), cyclic loading (J. J. Williams, Yazzie, et al. 2013; Jason J. Williams et al. 2011), and SCC (L. Babout et al. 2006; Marrow et al. 2006; King, Ludwig, Engelberg, et al. 2011) have been conducted using X-ray tomography.

In this study, we have used X-ray synchrotron tomography to study the crack growth behavior of under-aged AA7075 in moisture. We were able to unequivocally determine whether the SCC cracks were discontinuous or simply a single tortuous crack. The SCC crack growth rates were measured and compared using the surface measurement (2D) and bulk measurement (3D). By using the *in situ* tomography approach it was possible to quantify the evolution of crack growth under SCC.

6.2 Materials and Experimental Procedure

X-ray synchrotron tomography was performed at the 2-BM beamline of the Advanced Photon Source (APS) at Argonne National Laboratory. The details of the tomography system at 2-BM have been described elsewhere (J. J. Williams et al. 2010;

De Carlo and Tieman 2004). A monochromatic beam with energy of 24.3 keV was focused on the specimen. A LuAG:Ce scintillator screen was used to convert the transmitted X-rays to visible light. This was coupled with a 5x objective lens and a PCO edge camera to achieve pixel sizes of 1.3 μm. 2D projections were collected at an angular increment of 0.12^{o} for a total of 1500 projections. These 2D projections were then reconstructed using the Gridrec Fast Fourier Transform (FFT)-based algorithm. The grayscale images obtained after reconstructions were segmented using conventional thresholding using image analysis software (ImageJ, Bethesda, MD). 3D rendering of these segmented SCC cracks was performed in Avizo® Fire (VSG, Burlington, MA) for visualization purposes.

A commercially available AA7075-T651 was solution heat treated at 475^{o}C for 2 hours followed by quenching in water and then aging for 80 minutes at 120^{o}C to obtain an under-aged condition (Vickers hardness of ~138 HV). Single edge-notch specimens (20 mm x 2.8 mm x 0.8 mm) were machined by electro-discharge machining (EDM) such that the loading direction was along the S-T orientation. The longest dimension (20 mm) is along the loading direction and the lowest dimension (0.8 mm) is the thickness. A width of 2.8 mm was chosen due to limited field of view (~ 3 mm, necessary to achieve a 2 μm resolution at the Advanced Photon Source). The thickness of 0.8 mm was chosen on the basis of two factors: the ability to easily nucleate a crack on the microforce testing system (MTS Tytron 250) having a maximum capacity of ~240 N, and the ability to observe the long growth of the crack while maintaining the diagonal dimension of the sample to be less than 3 mm. Fatigue precracking was performed *ex situ* on a microforce

testing system (MTS Tytron 250) in tension-tension fatigue (4 Hz, R=0.1). The precracking length was about 1 mm.

The stress corrosion cracking experiments were performed in the *in situ* loading stage as shown in Figure 45a. The stage was designed to be less than 2 kg due to the weight limit of the motion stages at the 2-BM beamline. The vertical range where the region of interest on the sample must intersect the X-ray beam is often restrictive and was between 15 mm to 40 mm. Thus, the distance from the bottom of our fixtures to the center of the sample was chosen to be 30 mm - a distance that included the base plate, sub-miniature load cell, bottom sample clamp and half the sample. The upper grip was attached to the stepper motor with a linear actuator, which imposes a displacement on the sample to achieve the desire load. A stepper motor was chosen because it could be easily integrated with motor drives already present at the beamline. The linear actuator was capable of 8 μm per step and a total stroke of 25 mm. The load cell had a capacity of 500 N. The load was transmitted from the top of the stage to the bottom through a polymer sleeve (Poly methyl methacrylate or PMMA). The PMMA material was chosen due to its transparency to X-rays. The actuator can be controlled automatically using feedback from the load cell. A few limitations of the loading stage include the maximum cyclic frequency of 2 Hz and the maximum load of only 500 N. Also, given that the fixture must rotate 180 degrees, and that it has a load bearing sleeve, 50 mm was the closest distance our samples could safely be from the scintillator without hitting it - a distance that yields significant phase contrast when using 24keV x-rays (produced by a bending magnet).

A schematic of the *in situ* loading stage to perform the SCC experiments in moisture is shown in Figure 45b. The PMMA sleeve has not been shown here for clear

visualization of the arrangements inside the stage. The sample was loaded on both sides using grips attached to the actuator on one side and the load cell on the other. To introduce moisture into the cell, an annular (ring shape) wet sponge was placed around the load cell at the base of the loading stage. Since stress corrosion cracking experiments require long exposures to moisture, maintaining a constant humidity inside the chamber is a big challenge as fluctuations can lead to variability in results. In order to minimize the loss of moisture and to maintain constant relative humidity, the top part of the loading stage was covered with a plastic wrap as shown in Figure 45b. A humidity sensor was placed in front of the notch to measure the relative humidity throughout the test. These arrangements led to the constant humidity of 95-96 % inside the system throughout the test, as shown in Figure 46. Samples were placed inside the deionized water for about a week before starting the SCC test in moisture at Argonne National Laboratory.

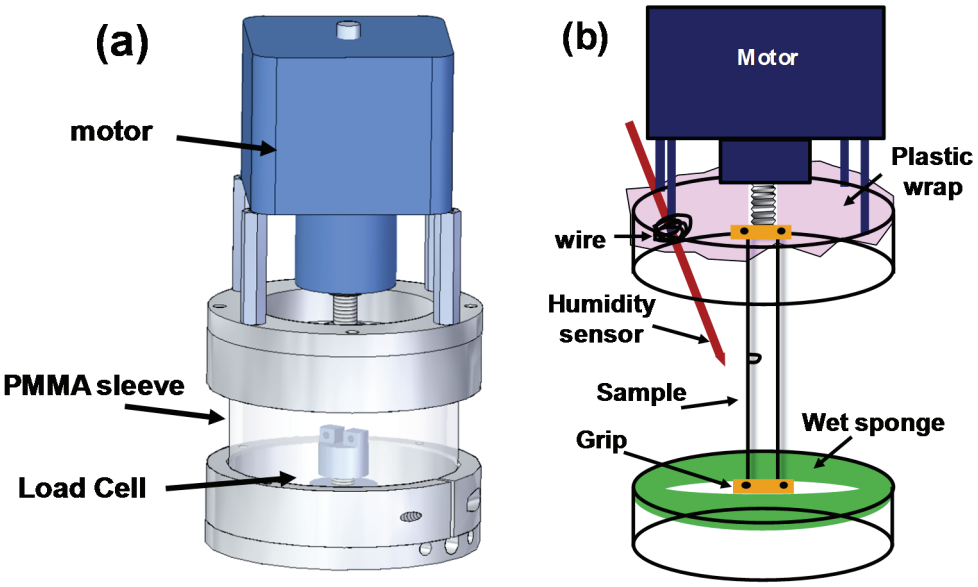

Figure 45. (a) *In situ* mechanical loading stage, and (b) schematic of *in situ* stage for stress corrosion cracking experiments in moisture. The PMMA sleeve is not shown in (b) to show the arrangements clearly

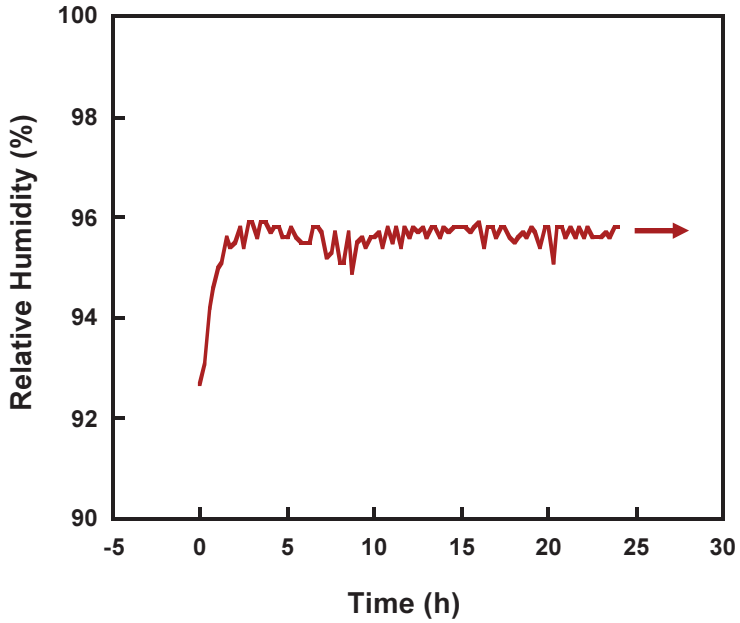

Figure 46. Relative humidity measurement throughout the SCC experiments showing constant value of ~ 95%

6.3 Results and Discussion

Figure 47 shows the steps to segment the SCC cracks. The original grayscale stack of images is first thresholed using ImageJ. This is followed by the use of 3D region grow in MIMICS and then few intersecting particles are manually removed. Figure 48 shows the 3D rendering of the SCC crack in moisture, where each color represents time (cumulative) during which the stress corrosion cracks grew at a constant load of 110 N. Two independent cracks (not connected in 3D) were observed, where the bottom crack almost covers the entire thickness. It is interesting to note that there is a significant variation in the crack length through the thickness and therefore variation in crack growth rate.

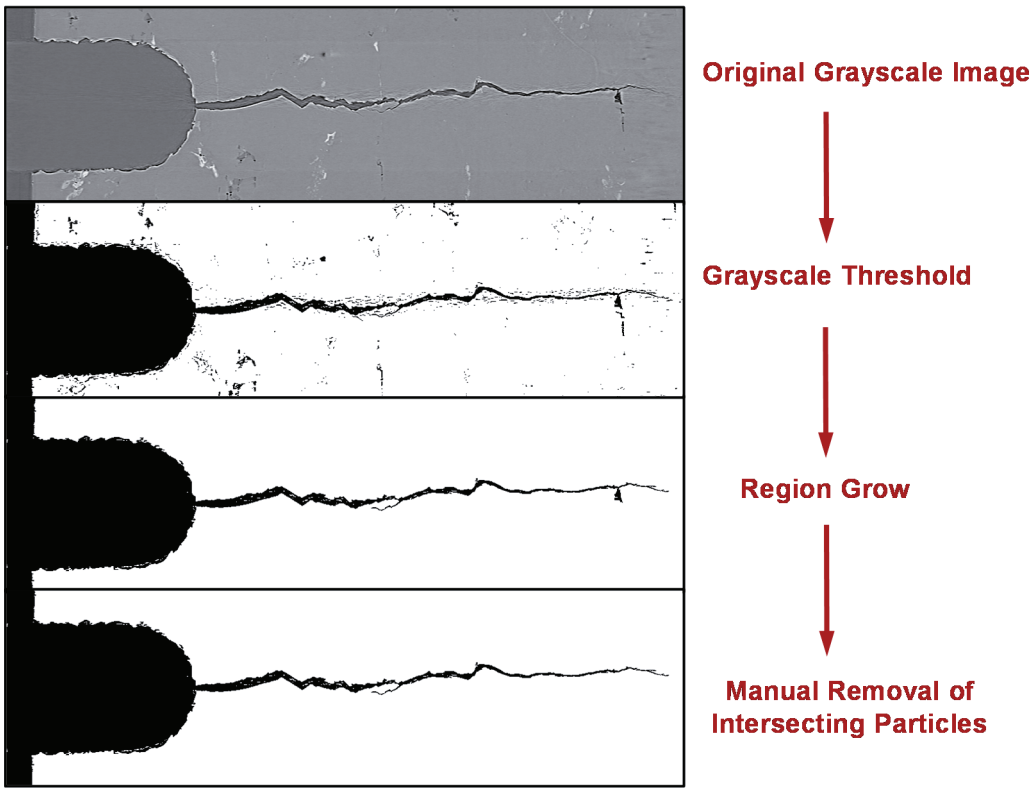

Figure 47. Steps to segment SCC cracks for 3D reconstructions

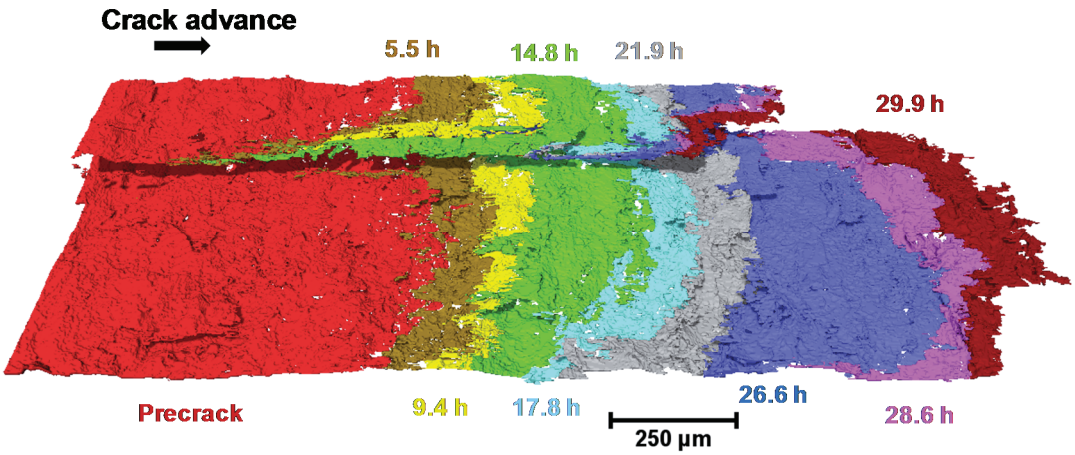

Figure 48. 3D SCC crack growth profile in moisture as a function of time. Significant variation of crack length through the thickness was observed

The discontinuous cracks on both sides of the specimen can clearly be seen from the 2D slices obtained from X-ray tomography after about 25 hours of stress corrosion cracking, as shown in Figures 49a and 49b. These 2D images indicate that the second crack might have initiated in front of the first crack and then grew separately. However, 3D rendering of the crack in Figures 49c and 49d actually show that these discontinuous surface cracks were connected in three dimensions. Figure 49 (e-i) shows the step wise growth of the crack and the appearance of discontinuous surface cracks, observed in Figure 49a. The time interval is shown in the legend. It can be seen that the main crack grew from inside towards the surface (Figure 49e and 3f) and finally appeared as a discontinuous crack on the surface (Figure 49g), and then continued to grow. The appearance of discontinuous surface cracks can clearly be seen in Figure 49j, which was not in Figure 49i. Both, Figures 49i and 49j are the top views of Figure 49f and 49g.

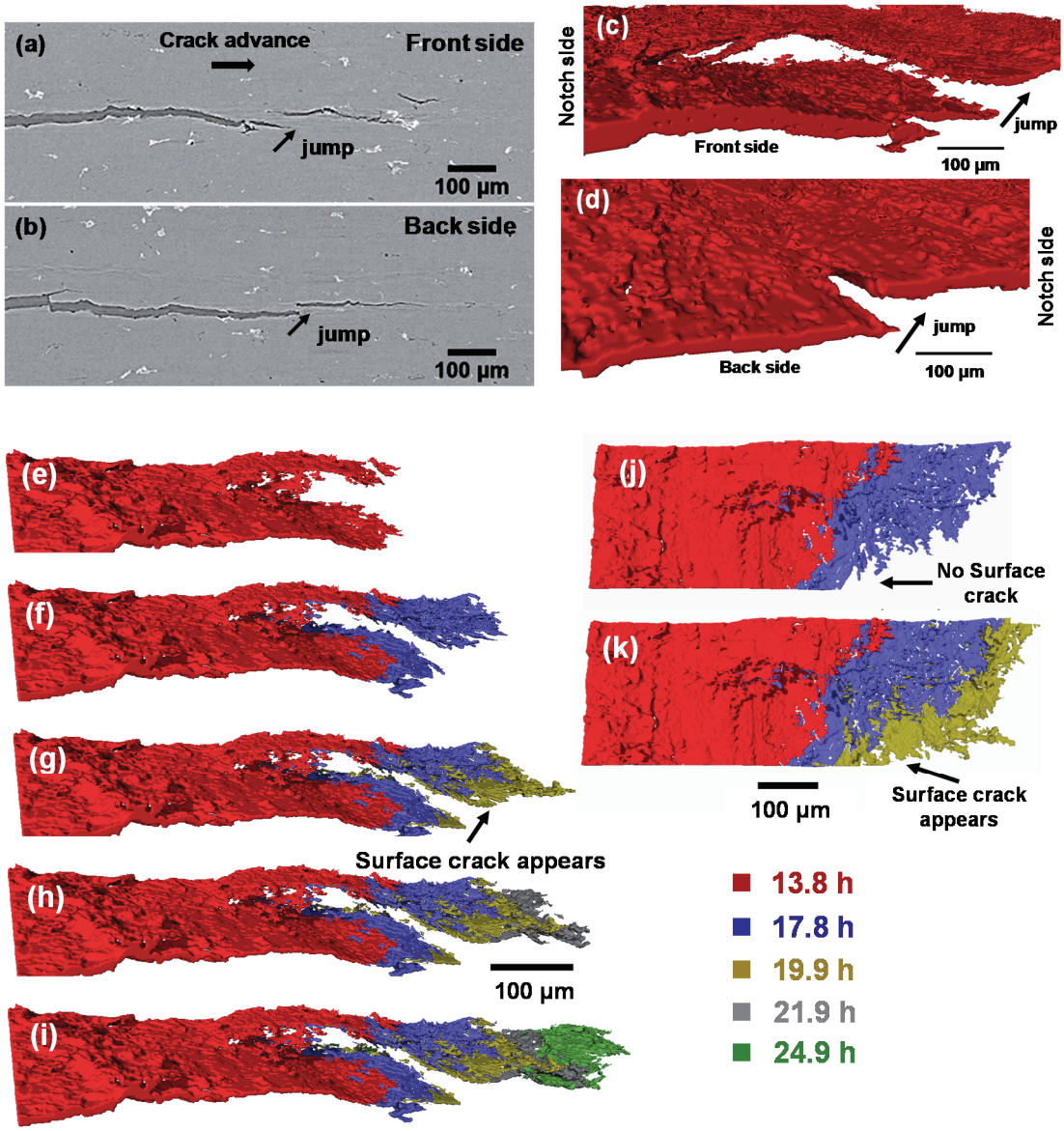

Figure 49. (a) and (b) are 2D slices of the sides of the specimen showing the discontinuous cracks (crack jump), (c) and (d) are the 3D reconstructions of part of the crack showing that the discontinuous crack at the surface are actually connected in 3D, (e-i) step wise growth of crack showing the appearance of the discontinuous crack (Fig. g) and then further growth, (j-k) top view of Fig. f and Fig. g showing that the surface crack doesn't appear in j but appears at k

The crack growth rates were measured using the average of the crack lengths at both sides (2D measurement) and also the average crack lengths though thickness (3D

measurement), as shown in Figure 50. Using 2D slices of the 3D crack, the crack length increment (da) was measured. This increment in crack length was then divided by the time increment (dt) to obtain the crack growth rate. The same time interval (dt) was used for both types of measurement. It can be seen that the crack growth rate has a significant amount of variability when surface crack lengths were used for the measurement (2D) compared to the growth rate when the average crack length through thickness was used (3D). Moreover, a large deviation in the surface crack lengths resulted in significant differences in stress intensity factor, as shown with error bars in Figure 50. These can be attributed to the highly non-uniform growth of the SCC crack at the surface which includes formation of discontinuous cracks and independent growth of the two cracks. The stress intensity factor (K) was calculated using the equations derived by Ahmad et al. for single edge notched specimens with fixed grip loading (Ahmad, Papaspyropoulos, and Hopper 1991). Since the stress corrosion cracking experiment was performed at constant load, the stress intensity factor increases with an increase in the crack length. For a particular crack growth rate value (da/dt), the stress intensity factor value (in Figure 50) was taken as the average of the stress intensity factor values corresponding to the initial and final crack length for that particular time interval.

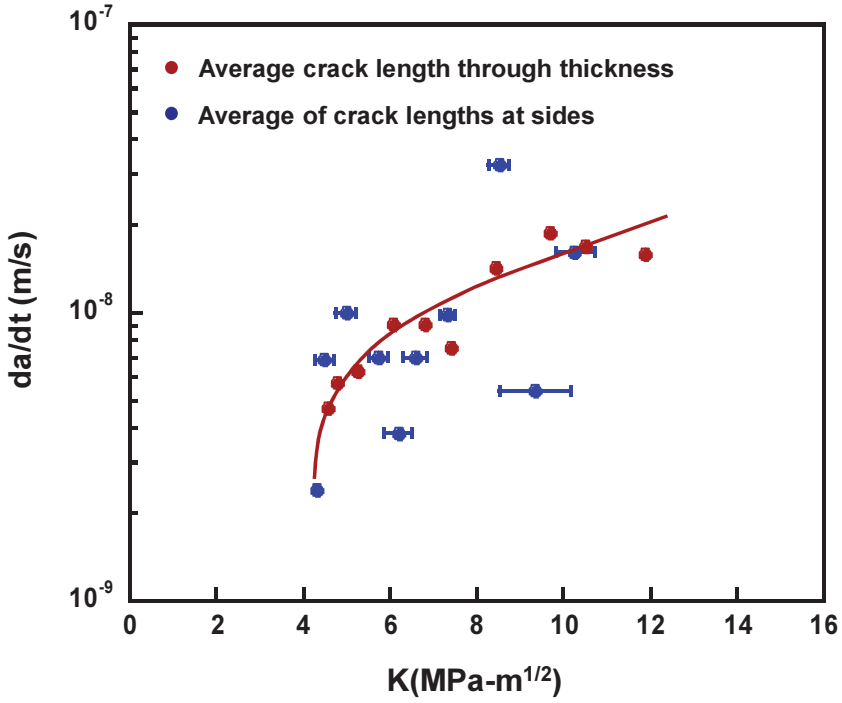

Figure 50. Crack growth rate measurement from average of the crack lengths (2D) and average of the crack length through thickness (3D). The 3D crack growth rate is quite uniform than of the measurement based on 2D

6.4 Summary

Using the X-ray synchrotron tomography, we have shown that the discontinuous surface cracks formed during SCC of AA7075 in moisture were actually a single crack connected in three dimensions. These discontinuous surface cracks were formed when the internal main crack grew from inside the specimen and appeared on the surface. The crack growth rates as determined by measured crack lengths at the surface (2D) led to highly variable crack growth rates than when measured using average crack lengths through thickness (3D). The results obtained here show the importance and necessity of

3D techniques, such as X-ray synchrotron tomography, to study the crack growth behavior during stress corrosion cracking.

CHAPTER 7

CORROSION BEHAVIOR OF ALUMINUM 7075 ALLOYS IN LIQUID ENVIRONMENT USING *IN SITU* X-RAY SYNCHROTRON TOMOGRAPHY

7.1 Introduction

Aluminum alloys are used in structural applications due to their high strength-to-weight ratio (Starke and Staley 1996), but they are susceptible to corrosion and show a significant decrease in strength when exposed to a corrosive environment. Several conventional techniques have been used to measure the corrosion rates of materials, such as weight loss measurement, hydrogen evolution technique, optical measurement, Tafel extrapolation of polarization curves, and electrochemical impedance spectroscopy (Davis 1999; Ezuber, El-Houd, and El-Shawesh 2008; Shi, Liu, and Atrens 2010; Hassan and Zaafarany 2013; Atrens et al. 2013). All of these methods are either 2D in nature or provide bulk measurement of corrosion.

Recently, X-ray tomography has emerged as an excellent technique to understand the localized corrosion behavior of materials in three dimensions (3D) (E. Maire and Withers 2014; Eckermann et al. 2008). The advantage of *in situ* X-ray tomography over other 3D techniques is that it is non-destructive in nature and therefore is suitable to study microstructure evolution with time (Buffiere et al. 2010; Stock 1999; Eric Maire et al. 2001). Knight et al. measured the intergranular corrosion rate of 2024 and 7050 aluminum alloys by measuring the depth of corrosion (Knight, Salagaras, and Trueman 2011; Knight et al. 2010). Liu et al. used X-ray radiography to measure the corrosion rate of AA2024 with and without application of stress by measuring the corrosion depth with

time (X. Liu et al. 2006). To the best of our knowledge, no studies have been performed to correlate the volume of hydrogen bubbles to the localized corrosion rate. The advantage of *in situ* X-ray tomography is that the localized corrosion rate of a material can be quantified by measuring the volume of the hydrogen bubble.

One of the constituent particles in 7075 aluminum alloys is Mg_2Si (Payne et al. 2010) and it has been shown that these particles are the initiation sites for pitting corrosion. Mg_2Si being more anodic to the matrix, tends to dissolve into solution (Birbilis and Buchheit 2008a; R. K. Gupta et al. 2012; Wloka, Bürklin, and Virtanen 2007) and hydrogen bubbles are produced due to cathodic reaction (Linardi, Haddad, and Lanzani 2012; R. K. Gupta et al. 2012).

In the presence of a corrosive fluid, fatigue crack growth rate increases significantly compared to crack growth rates in air (Pao et al. 1989; Mills 1997). X-ray tomography has been used to understand fatigue crack growth behavior in Al-Mg-Si (H. Zhang et al. 2009; Toda et al. 2008), Al7075 (J. J. Williams, Yazzie, et al. 2013; Jason J. Williams et al. 2011) and Mg alloy (King, Ludwig, Herbig, et al. 2011) in air. To the best of our knowledge, the *in situ* corrosion fatigue behavior of 7075 aluminum alloys has not been studied by X-ray tomography.

In this study we have used *in situ* X-ray synchrotron tomography to measure localized corrosion rate of Mg_2Si particles in deionized ultra-filtered water (DIUF) by measuring the volume of hydrogen bubbles. The effect of stress (in constant load-SCC) on the initiation of localized corrosion of Mg_2Si particles has also been discussed. Fatigue experiments were performed in EXCO solution (4M NaCl, 0.5 M KNO_3 and 0.1 M HNO_3). Furthermore, experiments were also performed in EXCO solution with and

without the application of load to understand the effect of applied stress on the exfoliation behavior of Al 7075 alloys. Preliminary results on the shape of bubbles, crack growth rate in fatigue along with the effect of inclusions on exfoliation were studied. More detailed analyses will be performed in future.

7.2 Materials and Experimental Procedure

AA7075-T651 in as received condition (LT orientation) was used for experiments in EXCO solution, whereas, 7075 aluminum alloys in under-aged condition (ST orientation) were used for SCC experiments in DIUF water. A commercially available 7075-T651 aluminum alloy was solution heat treated at 475^{o}C for 2 hours followed by quenching in water and then aging for 80 minutes at 120^{o}C to obtain an under-aged condition.

X-ray synchrotron tomography was performed at the 2-BM beamline of the Advanced Photon Source (APS) at Argonne National Laboratory. The details of the tomography system at 2-BM have been described elsewhere (De Carlo and Tieman 2004; J. J. Williams et al. 2010). Before scanning at APS, single edge-notch specimens (25 mm x 2.8 mm x 0.8 mm) were machined by electro-discharge machining (EDM), as shown in Figure 51. The specimens were polished and then fatigue precracked *ex situ* on a microforce testing system (MTS Tytron 250) in tension-tension fatigue (4 Hz, R=0.1). The loading direction was along the S-T orientation and L-T orientation for experiments in DIUF water and in EXCO solution, respectively. L, S and T refer to longitudinal, short-transverse and transverse direction, respectively.

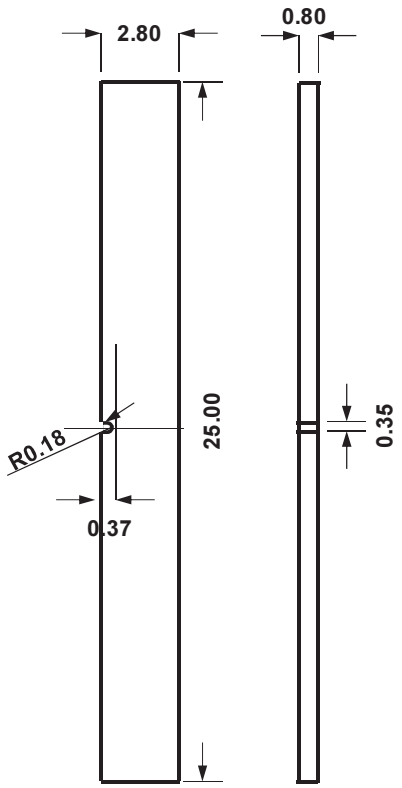

Figure 51. Single edge notch specimen used for *in situ* experiments (dimensions are in mm)

The load was applied on the sample using an *in situ* loading stage, as shown in Figure 52a. The details of the loading jig and alignment of the sample is given in the chapter 6. To perform the loading experiments in DIUF water/EXCO solution, a polymeric PEEK (Polyether ether ketone) cylindrical grip was chosen to replace the bottom steel grip and was fitted with the load cell, as shown in Figure 52b. The PEEK was chosen since it is chemical resistant to the EXCO solution and has good mechanical strength and therefore can sustain the applied load. A rectangular hole was made at the top part of the PEEK grip to accommodate the sample. A hole was made on the side wall of the cylindrical grip to accommodate the stainless steel pin which passes through the

hole made in the sample. Epoxy was added to make this a permanent and strong connection. Kapton tubing was attached to the PEEK cylinder with epoxy to hold the liquid around the sample during the test. Kapton tube is also chemical resistant to the EXCO solution. The height of the Kapton tube was chosen such that the notch of the specimen was immersed in the liquid. Figure 53 shows the schematic of the arrangements to perform the test without load. The motor and PMMA sleeve were removed during the test, since application of load was not required. Nail paint, which is non-reactive to the EXCO solution for the duration of experiment, was used in both the samples to maintain the volume to metal surface area ratio of 10-30 ml/cm^2 for exfoliation corrosion, as per ASTM standard.

"Pink beam", which is a polychromatic beam with low and high energies removed from the white beam spectrum, was used during corrosion experiments. Pink beam provides higher photon flux compared to a monochromatic beam and allows for significantly faster data acquisition. Thus the progression of corrosion could be documented with a higher frequency, which is required to capture the evolution of bubbles. A 5x objective lens and a PCO Dimax camera were used to achieve a pixel size of 2.2 μm. A total of 1500 2D projections were obtained and then reconstructed using the Gridrec Fast Fourier Transform (FFT)-based algorithm.

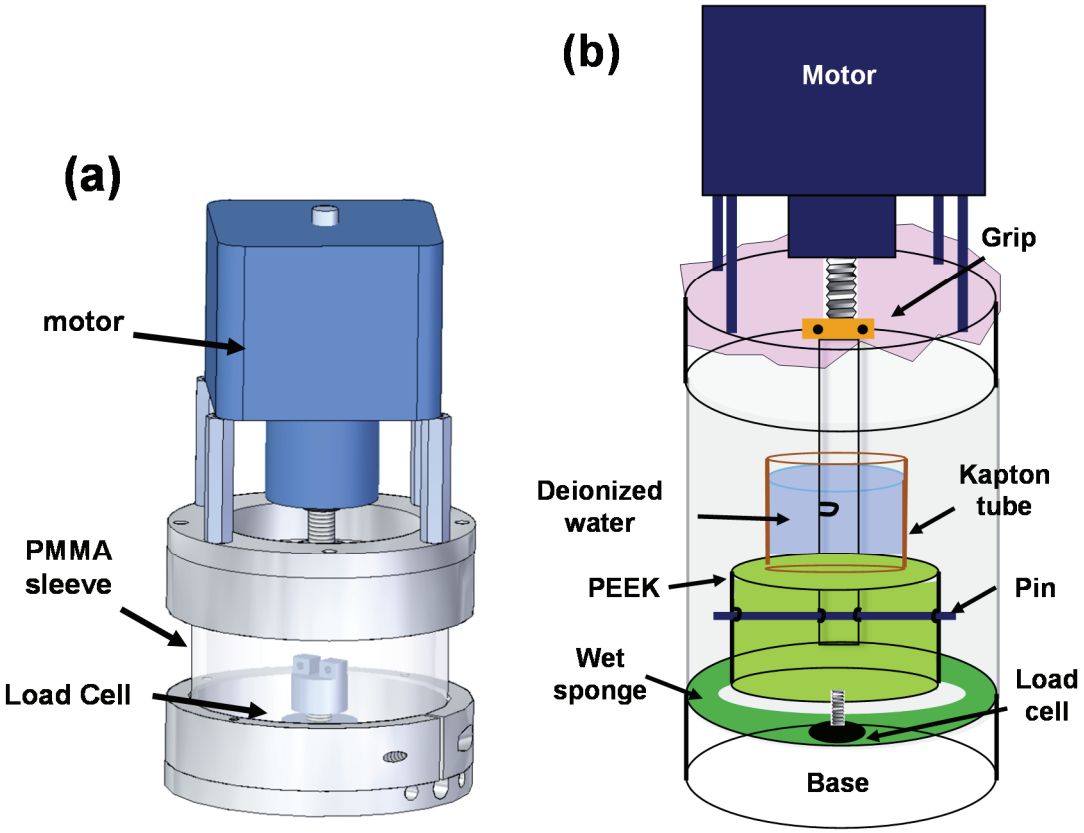

Figure 52. (a) *In situ* mechanical loading stage, and (b) schematic of *in situ* stage testing in de-ionized water/EXCO solution

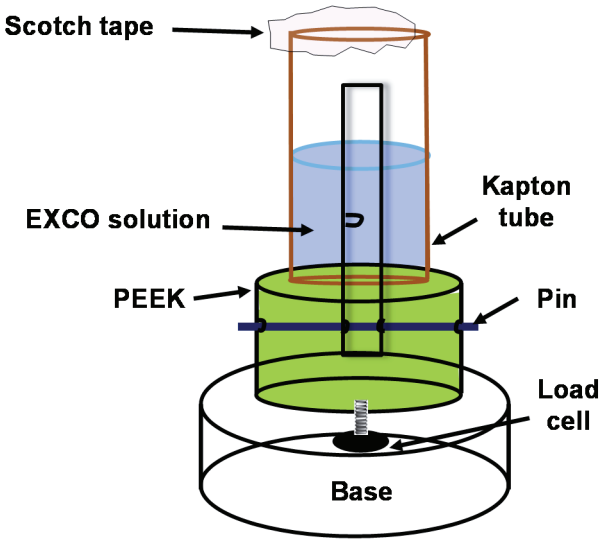

Figure 53. Schematic to perform exfoliation corrosion experiments without load

The grayscale images obtained after reconstructions were analyzed and segmented using image analysis software (ImageJ, Bethesda, MD). 3D rendering and quantification of the segmented hydrogen bubbles/cracks were performed in Avizo® Fire (VSG, Burlington, MA) and MIMICS (Ann Arbor, MI).

7.3 Results and Discussion

7.3.1 SCC Experiments in DIUF Water

Figure 54a shows the microstructure of Al7075 alloys obtained from X-ray synchrotron tomography, where Mg_2Si (black phases) and Fe-bearing particle (white phases) can be seen in the aluminum matrix. Attenuation of the incident X-rays is proportional to mass density; and therefore, Fe-bearing particles (high mass density) appear bright and Mg_2Si (low mass density) appear dark in the reconstructed images.

Figures 54(a-c) show the evolution of a hydrogen bubble with an increase in corrosion of an Mg_2Si particle with time. The start time (t = 0 minutes) here is the time when a constant load was applied just after *in situ* fatigue precracking in DIUF water was completed. The pH of the DIUF water at the beginning of the test was ~5.5, which is slightly acidic. Recently, it has been shown that Mg_2Si is less noble than 7075 aluminum matrix in acidic and neutral solution and therefore will preferentially dissolve into the solution (R. K. Gupta et al. 2012). It has also been argued by many authors that the dissolution process of Mg_2Si is a dealloying process, where magnesium selectively dissolves into the solution and the particle gets enriched in silicon (ZENG et al. 2011; Linardi, Haddad, and Lanzani 2012; R. K. Gupta et al. 2012). Figures 55a and 55b show

the 3D rendering of the hydrogen bubbles produced due to the corrosion of Mg_2Si particles at t = 50 minutes (Figure 1b) and t = 56 minutes (Figure 1c), respectively.

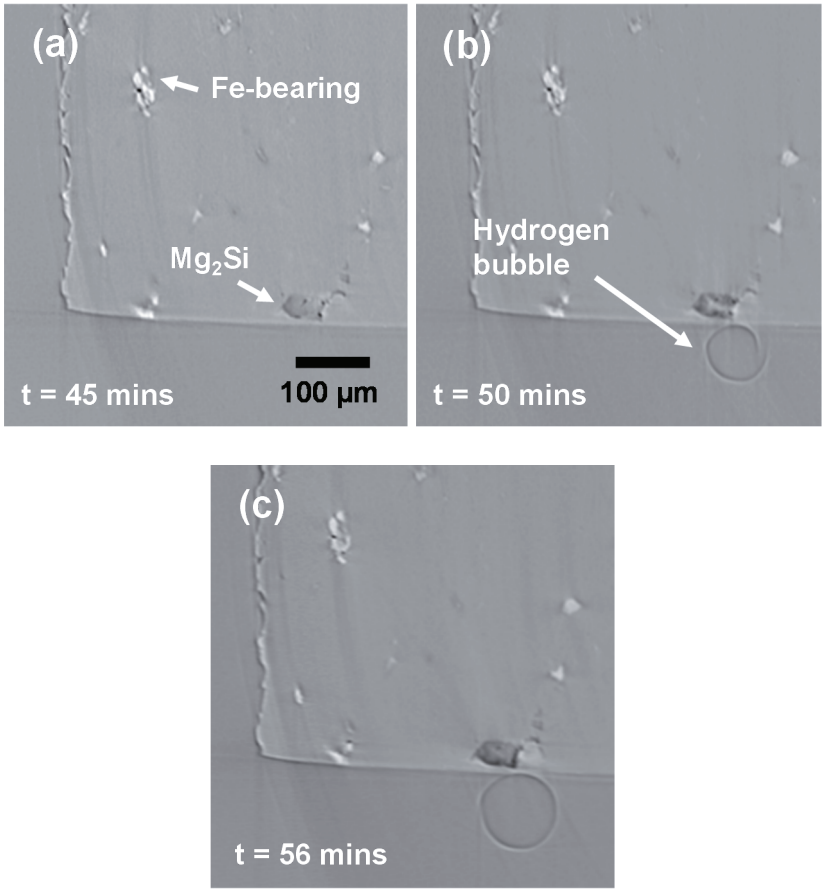

Figure 54. Evolution of corrosion of Mg_2Si and increase in size of hydrogen bubble with time.

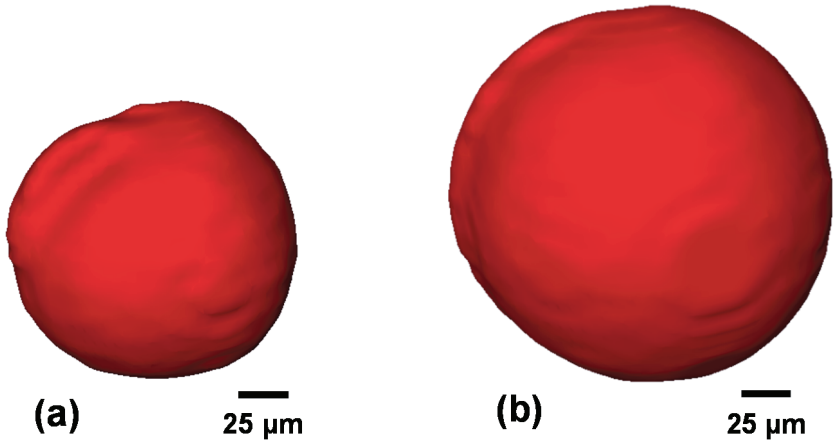

Figure 55. 3D rendering of hydrogen bubbles (a) at t = 50 minutes, and (b) at t = 56 minutes

Since the exact time of initiation of evolution of hydrogen bubble is not known, the corrosion rate of the Mg_2Si particle was calculated from the volume of hydrogen bubbles between 50 minutes and 56 minutes (time difference of 6 minutes). The volume of hydrogen bubble is converted to the weight loss due to magnesium dissolution since one mole of magnesium produces one mole of hydrogen gas. This weight was used to calculate the corrosion rate of Mg_2Si particles. Two Mg_2Si particles were located where bubbles didn't move with time and were used for calculation purpose. The calculated corrosion rates were very close to each other and were ~ 177 x 10^{-7}gm/cm^2/min and ~ 255 x 10^{-7}gm/cm^2/min, respectively. Few assumptions have been made for the calculation of corrosion rate of Mg_2Si particles. Firstly, STP condition has been assumed. Second, the reduction due to the presence of dissolved oxygen has been neglected. It should also be noted that the initial surface area of the particles has been taken into account. The results here indicates that the localized corrosion rate of a material can be obtained using X-ray tomography provided the scans are taken very fast.

In aluminum alloys, pitting corrosion are generally observed in the presence of halide (chloride) ions since they help in breaking the passive film (Ghosh 2008). Figure 56 shows the effect of crack tip stress on the initiation of corrosion of Mg_2Si particles in the absence of chloride ions (or negligible) in DIUF water. The images in Figure 56 are 2D slices obtained from tomography and are ~ 8.8-11 μm away from one face of the sample where the notch and the crack are somewhat visible. It should be noted that after about 12 hours from the start of *in situ* experiment, the crack didn't grow at constant load (SCC) and therefore *in situ* fatigue precraking was again performed in the DIUF water to grow the crack further and generate sharp crack tip to facilitate the crack growth during SCC. For the initial 12 hours before *in situ* fatigue precracking was performed, no bubbles were observed in the scans. Even after 40 minutes of SCC at constant load of 130 N, no bubbles were observed near Mg_2Si particles, as shown in Figure 56b. However, as the crack grew longer during SCC, bubbles were observed but only on one side (left side) of the sample. The region where bubbles were observed is marked as "bubble region" in Figures 56c and 56d. The opposite face of the sample showed approximately the same trend with bubbles appearing only after 35 minutes of SCC. This might be attributed to the high stress intensity factor at the crack tip as crack grows. We believe that the plastic zone ahead of the crack tip might have led to decohesion of boundaries or fracture of the particles to produce the hydrogen bubbles. The Irwin's equation for plane stress (M. Meyers, K. K. Chawla 2008) predicts that plastic zone size for the face shown in Figure 56 should be ~ 485 μm and the particles producing the hydrogen bubbles were within this range which also supports our hypothesis.

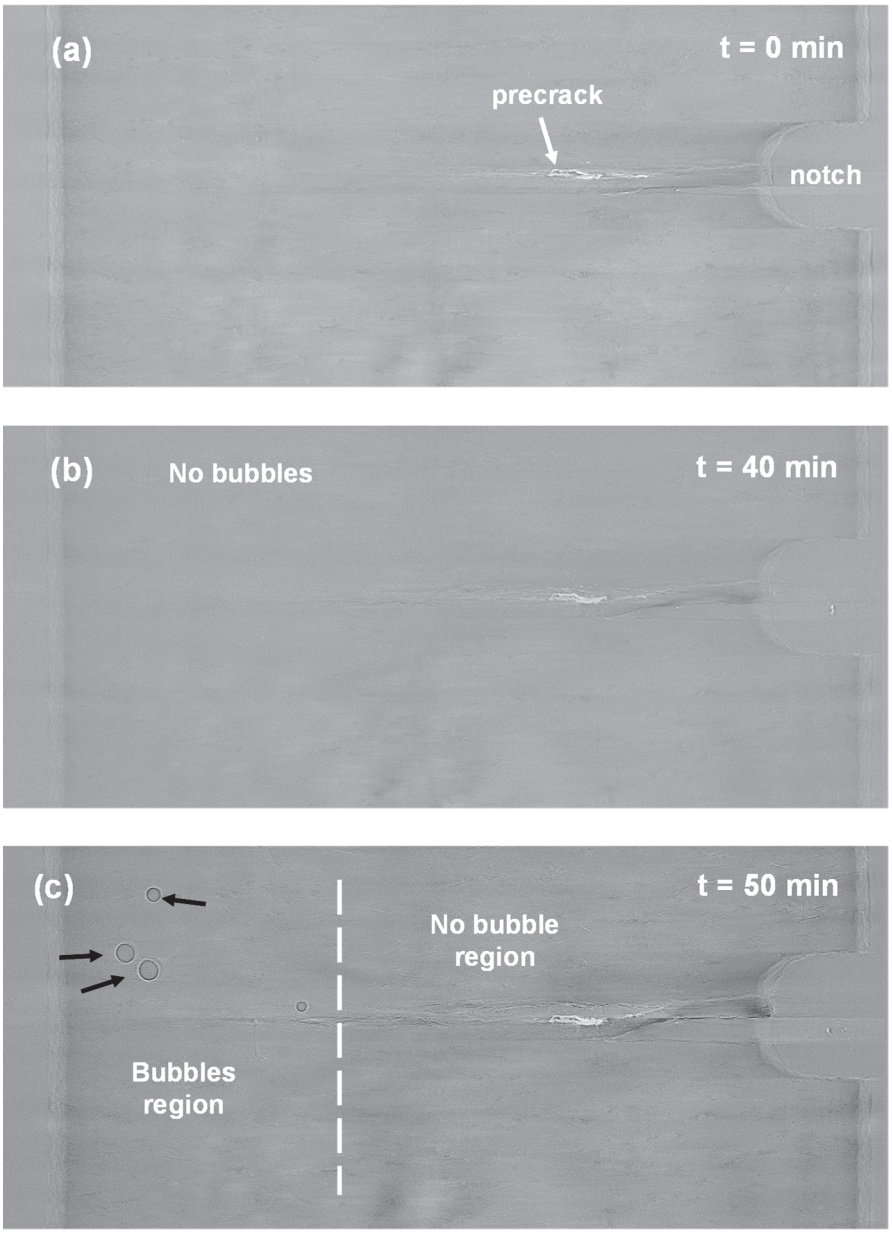
(a)
t = 0 min
precrack
notch
(b)
No bubbles
t = 40 min
(c)
t = 50 min
No bubble region
Bubbles region

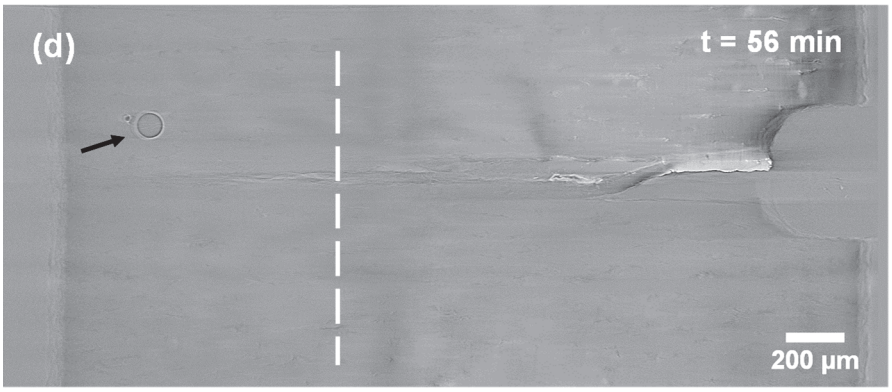

Figure 56. Effect of crack tip stress on bubble formation from Mg_2Si particles. No bubbles were observed till 35 minutes after *in situ* precracking. Bubbles were observed only on the left side of the sample, marked as bubbles region

7.3.2 Experiments in EXCO Solution

Experiments were performed in EXCO solution with and without load (cyclic and static). Preliminary results will be presented here and more detailed analyses will be performed in future work. Fatigue experiments in EXCO solution were conducted in the Paris law regime at a frequency of 0.5 Hz and R-ratio of 0.1. Figure 57 shows the comparison of fatigue crack growth rate (da/dN), versus stress intensity factor range (ΔK) of Al7075-T651 in EXCO solution and in air. The data for fatigue crack growth in air are from a previous study (J. J. Williams, Yazzie, et al. 2013). It is evident that the crack growth rate is significantly higher in corrosive fluid than in air for stress intensity levels between 5 MPa$\sqrt{m}$ and 10 MPa$\sqrt{m}$.

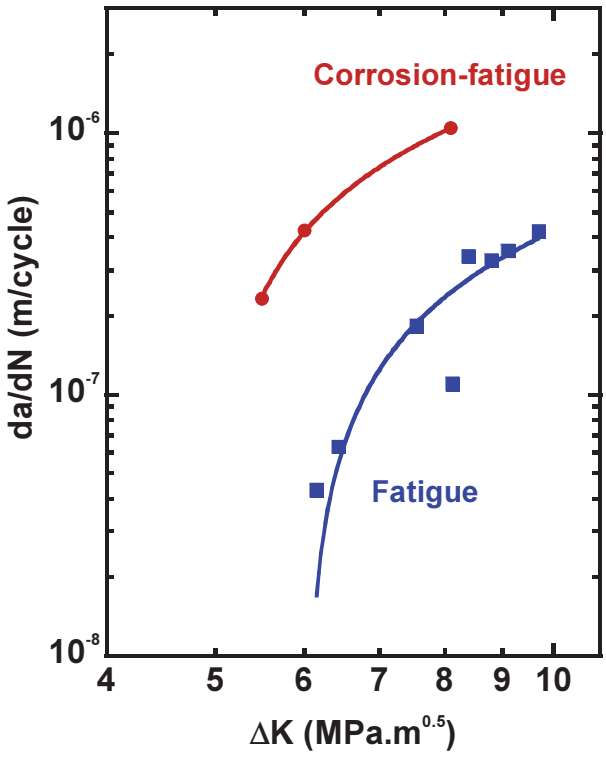

Figure 57. Comparison of fatigue crack growth rate in EXCO solution and in ambient air by *in situ* X-ray tomography. FCG rate increases significantly in EXCO solution

Figure 58 shows the side view of 2D slices with and without EXCO solution (142 minutes after addition of the solution). The pixel size in these experiments was 1.46 μm. In Figure 58b, bubbles and corrosive fluid inside the crack, and corrosion product surrounding the crack are visible which were not present before addition of fluid (Fig. 58a). The EDM notch is in the left side of the image. These bubbles in Figure 58b are mostly hydrogen bubbles produced during the reaction between corrosive fluid and Al alloys.

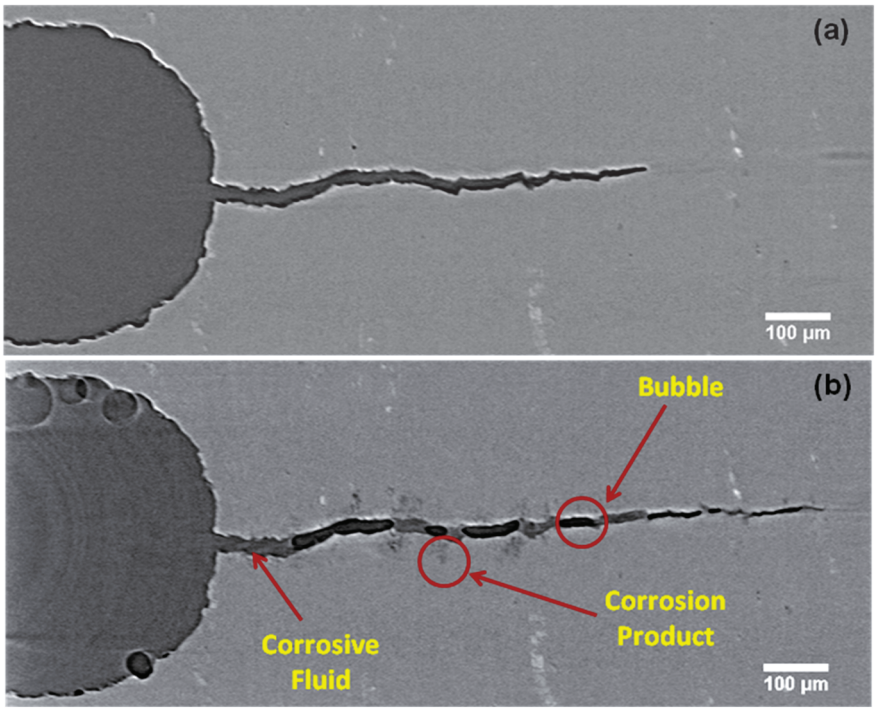

Figure 58. Side view of X-ray tomography slices (a) without EXCO solution and (b) with EXCO solution after 142 minutes showing hydrogen bubbles, corrosive fluid, and corrosion products

A part of crack (150 out of about 490 2D slices) and bubbles inside it were segmented using thresholding in image analysis software (ImageJ, Bethesda, MD). Since the crack consists of bubbles and corrosive fluid, segmented bubbles were subtracted from the segmented crack to obtain corrosive fluid. The 3D reconstruction of a 2D stack of segmented images was performed using commercially available software (MIMICS, Ann Arbor, MI). Figure 59 shows the 3D reconstruction of the crack, bubbles and corrosive fluid. The volume of bubbles inside the crack was around 32% of the total crack volume.

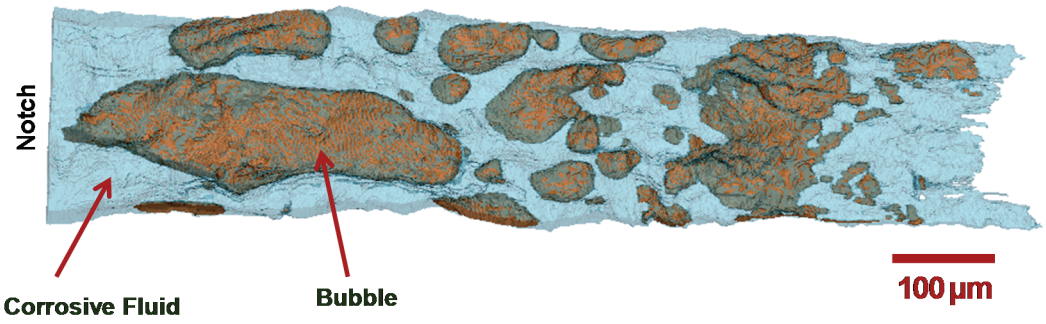

Figure 59. 3D reconstruction of crack (bubble + corrosive fluid) after 142 minutes in EXCO solution

Corrosion products were also segmented using thresholding in ImageJ on a few slices (from the part of crack) as shown in Figure 60. The corrosion products growing away from the crack are visible (also in Figure 58b). The average height of the corrosion products from around 30 different measurements on 2D slices was found to be 35 µm.

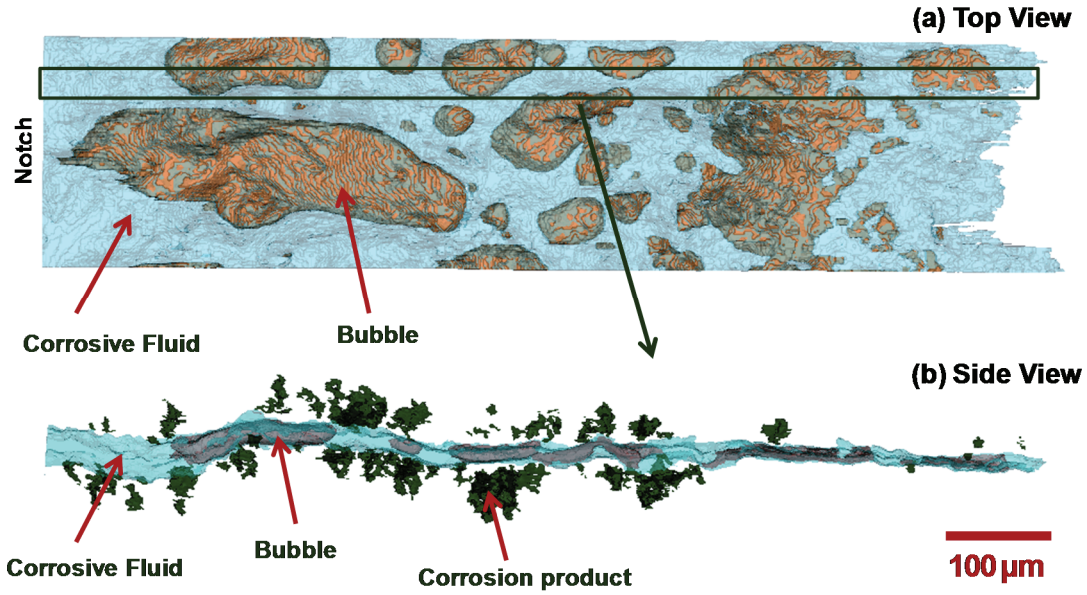

Figure 60. 3D reconstruction of (a) top view of the fatigue crack (bubble + fluid) and (b) corrosion products from selected area of the segmented crack after 142 minutes of addition of EXCO solution

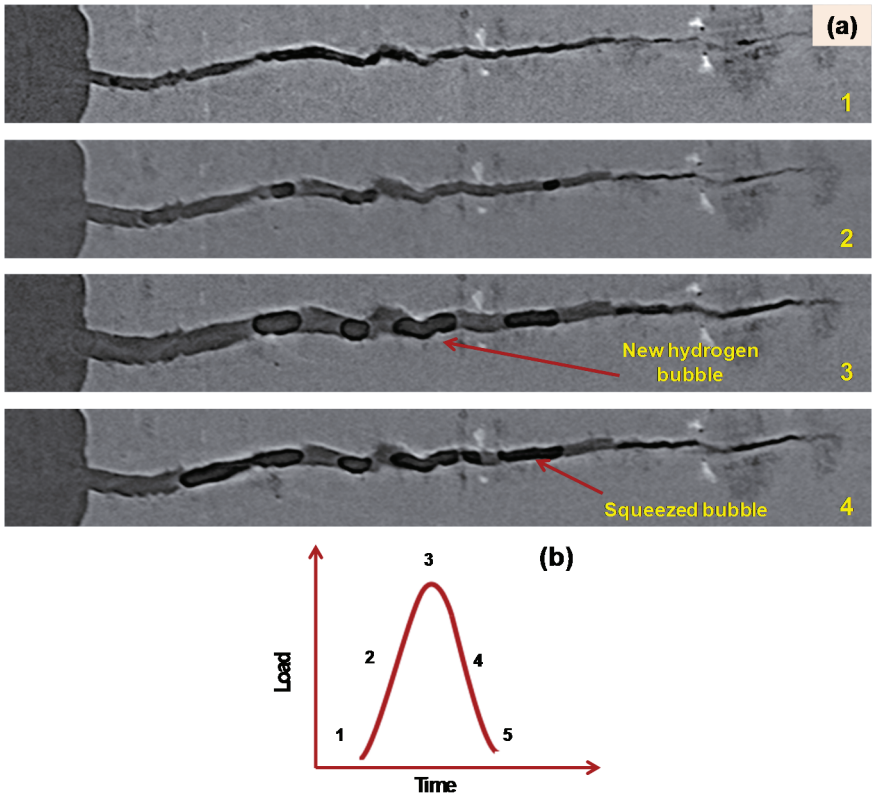

Figure 61. (a) 2D X-ray tomography images showing hydrogen bubble formation and change in morphology of bubbles in one fatigue cycle (b) corresponding fatigue cycle

Figure 61 shows the changes in bubbles shape and formation of a new bubble during one fatigue cycle. A bubble formed at position 3 in a fatigue cycle (it is not present at position 2). All bubbles get squeezed as the crack closes during unloading at position 4.

Figure 62 shows the z-projections of the specimen without and with EXCO solution, when load is not applied. Hydrogen bubbles produced from the reaction of the alloy with the solution can be seen all around the sample in Figure 62b. After 16.5 hours of exposure, the extent of corrosion was very high. Figure 63 shows the evolution of exfoliation with time.

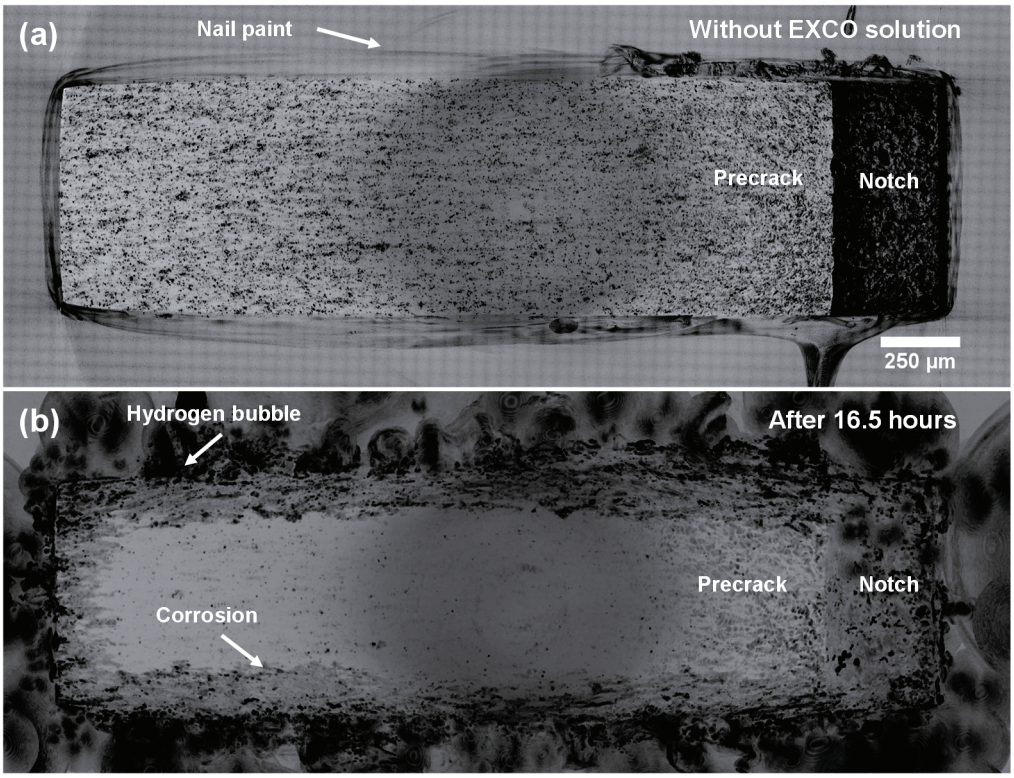

Figure 62. Z-projection showing the extent of corrosion (a) without EXCO solution, and (b) 16.5 hours after EXCO solution was put inside the Kapton tube

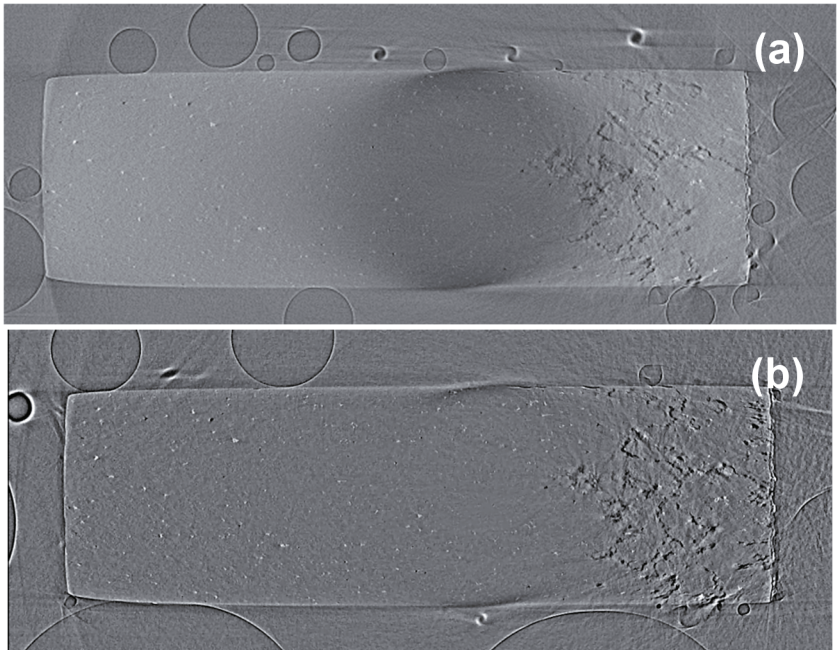

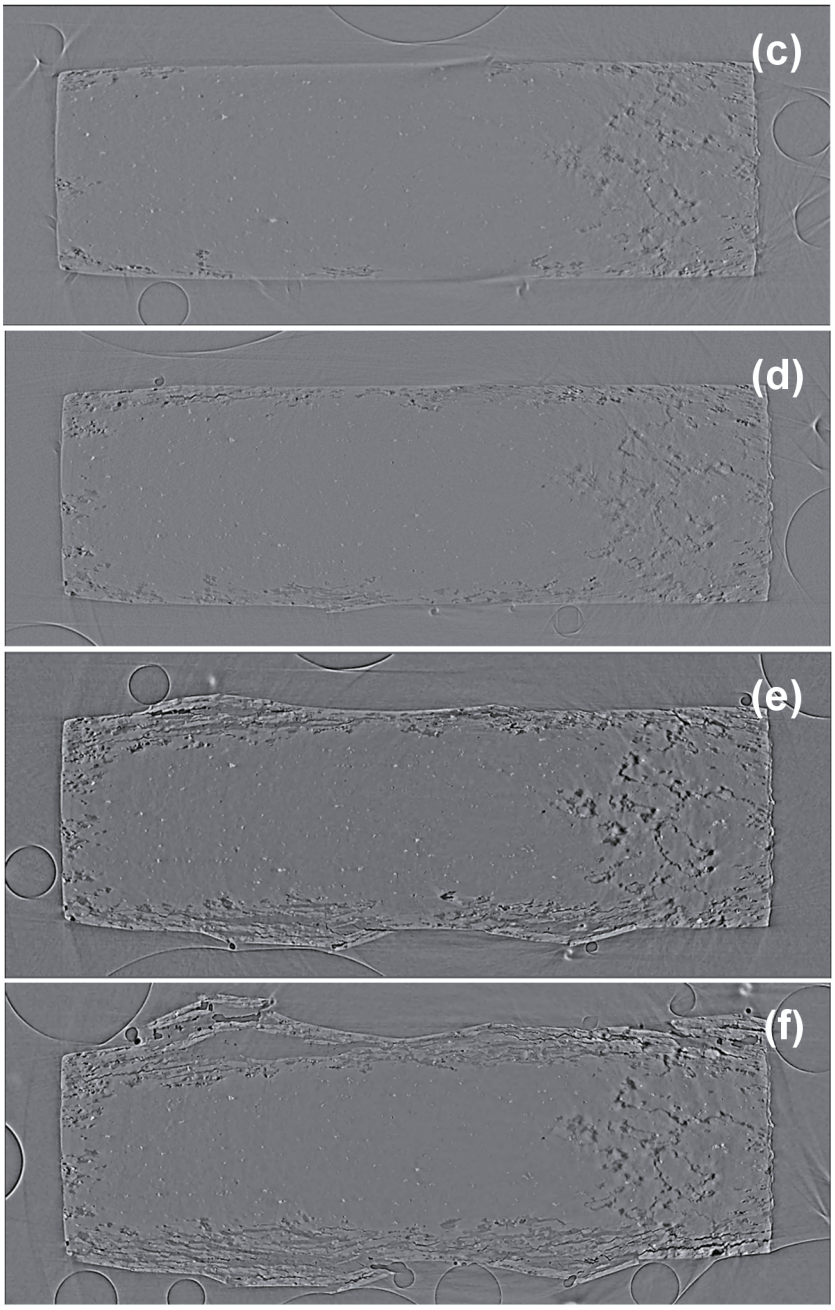

Figure 63. 2D X-ray tomography slices showing evolution of exfoliation with time. The exfoliation increases with time. (a) 14 mins, (b) 67 mins, (c) 177 mins, (d) 372 mins, (e) 675 mins, and (f) 913 mins. The sample with is ~ 2.8 mm

Effect of inclusions on the exfoliation corrosion of the alloy was also studied. Preliminary study indicates that initiation is a stochastic process and exfoliation initiates in Fe-bearing inclusions (Al_7Cu_2Fe), as shown in Figure 64. Fe-bearing inclusions are cathodic compared to the matrix, therefore matrix around the inclusions tend to dissolve, initiating exfoliation corrosion.

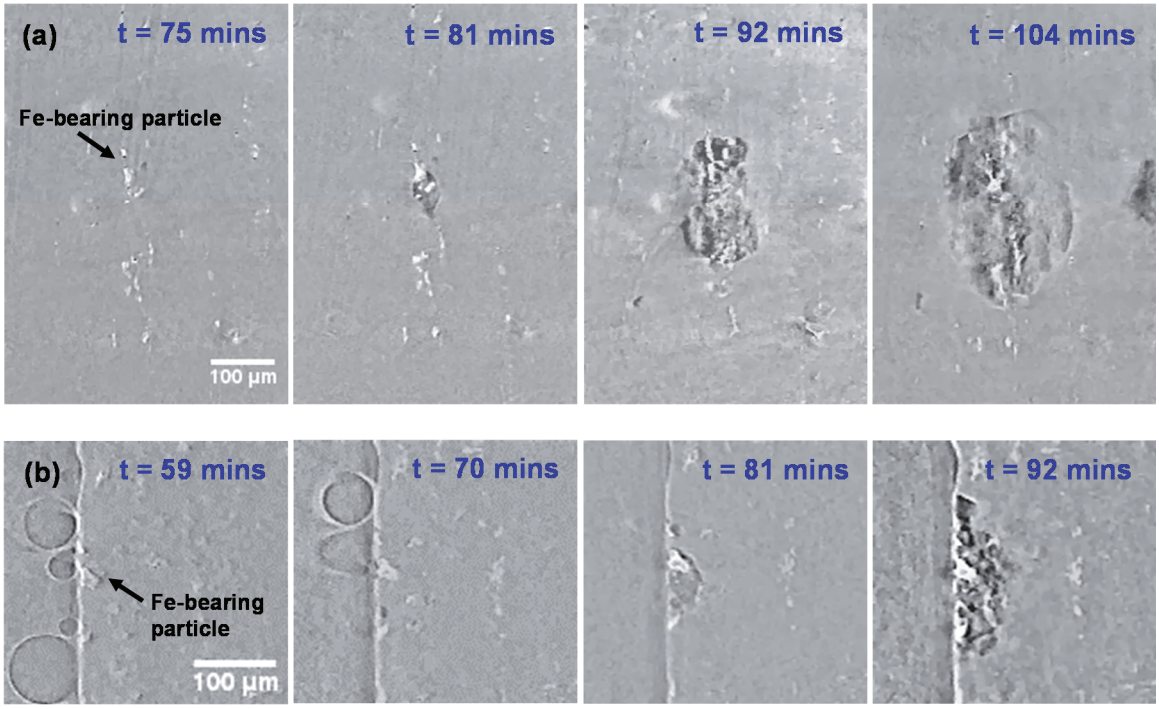

Figure 64. Initiation of exfoliation corrosion on Fe-bearing inclusions. Exfoliation initiates due to dissolution of the matrix surrounding Al_7Cu_2Fe

7.4 Summary

In situ X-ray synchrotron tomography is an excellent technique to understand the corrosion properties in liquid environments. The following conclusions can be made from the study:

(1) The evolution of hydrogen bubbles was captured in 3D. This allowed the measurement of localized corrosion rate of Mg_2Si particles. The corrosion rates of two particles were ~ 177 x 10^{-7}gm/cm^2/min and ~ 255 x 10^{-7}gm/cm^2/min. It was shown that stress was required to start the initiation of corrosion of the particle in DIUF water. These results demonstrate that *in situ* X-ray synchrotron tomography can be used to measure localized corrosion rate of a material.

(2) The fatigue crack growth rate from 2D slices in corrosive fluid (EXCO solution) was compared with the growth rate in ambient air. The fatigue crack growth rate was found to be significantly higher in EXCO solution than in ambient air. Hydrogen bubbles form due to reaction between Al alloys and corrosive fluid and their morphology inside the crack changes with time.

(3) Preliminary results suggest that the initiation of exfoliation occurs at Fe-bearing inclusions.

CHAPTER 8

CONCLUSIONS

8.1 Summary of Research Findings

1) The 3D microstructure of the constituent particles present in Al 7075 alloys was obtained using X-ray synchrotron tomography. 3D visualization showed that the constituent particles and pores are uniformly distributed and all pores are associated with the inclusions. The total volume fraction of the inclusions was much higher (1.63%) than that of the porosity (0.06%). Of the inclusions, the highest volume fraction of particles were composite inclusions of Al_7Cu_2Fe and $Al_{23}Fe_4Cu$ (0.58%). Quantitative analysis showed that the inclusions with small volume were spherical in nature. However, as the volume of the inclusions increased, the lengths along L and T increased much more than along the S direction.
2) FIB tomography was used to visualize and quantify the grains and precipitates in 7075-T651 aluminum alloys in 3D, after localization of a region of interest via XRM. The shape of the recrystallized grains was approximately spherical with sphericity and maximum feret diameter values of 0.73 ± 0.05 and 2.9 ± 1.38 μm, respectively. The volume fraction of the precipitates in 7075-T651 aluminum alloy was found to be ~ 2.37%. The visualization and quantification of the precipitates showed that the precipitates with large volume are associated with grain boundaries (average value ~ 7.7x105 nm3) and precipitates inside the grains have relatively small volume (average value ~ 2.9x105 nm3). The feret diameter and aspect ratios of precipitates on grain boundaries are also higher than precipitates inside the grains.

3) Nanoindentation with continuous stiffness measurement (CSM) was used to accurately measure the Young's modulus and hardness values of inclusions in the Al 7075 alloy. The Young's modulus values of Al_7Cu_2Fe, $Al_{23}Fe_4Cu$, and Mg_2Si were measured to be 160.2 ± 10.9, 139.5 ± 3.7, and 94.8 ± 7.5 GPa respectively. Values of hardness of Al_7Cu_2Fe, $Al_{23}Fe_4Cu$, and Mg_2Si were 8.8 ± 0.9, 7.5 ± 0.8, and 5.2 ± 0.5 GPa respectively.
4) Iron bearing inclusions had the highest strength followed by Si-bearing inclusions, and then Al 7075 matrix. Al_7Cu_2Fe constituent particles were completely brittle in nature and had compressive failure strength of 2.5 ± 0.2 GPa. Si-bearing inclusions had yield strength of 1.8 ± 0.1 GPa.
5) Using the X-ray synchrotron tomography, it was found that the discontinuous surface cracks formed during SCC of AA7075 in moisture were actually a single crack connected in three dimensions. The crack growth rates as determined by measured crack lengths at the surface (2D) led to highly variable crack growth rates than when measured using average crack lengths through thickness (3D). The results obtained here show the importance and necessity of 3D techniques, such as X-ray synchrotron tomography, to study the crack growth behavior during SCC.
6) *In situ* SCC experiments were performed using X-ray synchrotron tomography in DIUF water. The localized corrosion rates of Mg_2Si were measured using the volume of produced hydrogen bubbles due to the cathodic reaction. It was shown that stress is necessary to initiate the corrosion of Mg_2Si particles in DIUF water.
7) *In situ* X-ray tomography was performed with and without application of load in the EXCO solution. The fatigue crack growth rate was found to be significantly higher in

EXCO solution than in ambient air. During fatigue, hydrogen bubbles inside the crack were found to change shape. Preliminary results show that the initiation of exfoliation is stochastic process and Fe-bearing inclusions are the initiation sites for exfoliation.

8.2 Future Work

1) Visualization and quantification of precipitates in the over-aged condition is to be performed. This will provide information on changes in shape and size of precipitates both inside grains and on grain boundaries, as a result of aging. EDS analysis can also be performed to better understand the change in precipitate composition associated with aging.
2) Analysis of the X-ray tomography data on the effect of stress on exfoliation corrosion behavior of aluminum alloys needs to performed. A detailed analysis on the role of inclusions on initiation and propagation needs to be carried out. The exfoliation rate of AA7075 needs to be measured in three dimensions by measuring the exfoliated volume and then compared to corresponding 2D measurements. The role of hydrogen bubbles also needs to be investigated in detail.

REFERENCES

Abbaschian, Reza, and Robert Reed-Hill. 2008. *Physical Metallurgy Principles*. Cengage Learning.

Adler, Philip N., and Richard DeIASI. 1977. "Calorimetric Studies of 7000 Series Aluminum Alloys: II. Comparison of 7075, 7050 and RX720 Alloys." *Metallurgical Transactions A* 8 (7): 1185–90.

Ahmad, Jalees, Victoria Papaspyropoulos, and Allen T. Hopper. 1991. "Elastic-Plastic Analysis of Edge-Notched Panels Subjected to Fixed Grip Loading." *Engineering Fracture Mechanics* 38 (4): 283–94.

AlHazaa, A., T. I. Khan, and I. Haq. 2010. "Transient Liquid Phase (TLP) Bonding of Al7075 to Ti–6Al–4V Alloy." *Materials Characterization* 61 (3): 312–17.

Andreatta, F., H. Terryn, and J. H. W. De Wit. 2004. "Corrosion Behaviour of Different Tempers of AA7075 Aluminium Alloy." *Electrochimica Acta* 49 (17): 2851–62.

Arnold, Eric M., Joel J. Schubbe, Patrick J. Moran, and Robert A. Bayles. 2012. "Comparison of SCC Thresholds and Environmentally Assisted Cracking in 7050-T7451 Aluminum Plate." *Journal of Materials Engineering and Performance* 21 (11): 2480–86.

Asano, Kazunori, and Hiroyuki Yoneda. 2008. "High Temperature Properties of AZ91D Magnesium Alloy Composite Reinforced with Short Alumina Fiber and Mg_2Si Particle." *Materials Transactions* 49 (7): 1688–93.

Atrens, Andrej, Guang-Ling Song, Fuyong Cao, Zhiming Shi, and Patrick K. Bowen. 2013. "Advances in Mg Corrosion and Research Suggestions." *Journal of Magnesium and Alloys* 1 (3): 177–200.

Au, Hiu. 1996. "Pitting and Crack Initiation in High Strength Aluminum Alloys for Aircraft Applications." Massachusetts Institute of Technology. http://dspace.mit.edu/handle/1721.1/11240.

Babout, Laurent, Eric Maire, Jean-Yves Buffière, and Roger Fougeres. 2001. "Characterization by X-Ray Computed Tomography of Decohesion, Porosity Growth and Coalescence in Model Metal Matrix Composites." *Acta Materialia* 49 (11): 2055–63.

Babout, L., T. J. Marrow, D. Engelberg, and P. J. Withers. 2006. "X-Ray Microtomographic Observation of Intergranular Stress Corrosion Cracking in Sensitised Austenitic Stainless Steel." *Materials Science and Technology* 22 (9): 1068–75.

Bansal, R. K., A. Kubis, R. Hull, and J. M. Fitz-Gerald. 2006. “High-Resolution Three-Dimensional Reconstruction: A Combined Scanning Electron Microscope and Focused Ion-Beam Approach.” *Journal of Vacuum Science & Technology B* 24 (2): 554–61.

Birbilis, N., and R. G. Buchheit. 2008a. “Investigation and Discussion of Characteristics for Intermetallic Phases Common to Aluminum Alloys as a Function of Solution pH.” *Journal of The Electrochemical Society* 155 (3): C117–26.

Birbilis, N., and R. G. Buchheit. 2008b. “Investigation and Discussion of Characteristics for Intermetallic Phases Common to Aluminum Alloys as a Function of Solution pH.” *Journal of The Electrochemical Society* 155 (3): C117–26.

Birbilis, N., M. K. Cavanaugh, R. G. Buchheit, D. G. Harlow, and R. P. Wei. 2005. “Understanding Damage Accumulation upon AA7075-T651 Used in Airframes from a Microstructural Point of View.” *MATERIALS SCIENCE AND TECHNOLOGY-ASSOCIATION FOR IRON AND STEEL TECHNOLOGY*- 1: 1.

Birnbaum, Howard K., and Petros Sofronis. 1994. “Hydrogen-Enhanced Localized Plasticity-a Mechanism for Hydrogen-Related Fracture.” *Materials Science and Engineering: A* 176 (1): 191–202.

Boettinger, Wiiliam J., U. R. Kattner, K. W. Moon, and J. H. Perepezko. 2006. *DTA and Heat-Flux DSC Measurements of Alloy Melting and Freezing*.

Bonakdar, A., F. Wang, J. J. Williams, and N. Chawla. 2012. “Environmental Effects on Fatigue Crack Growth in 7075 Aluminum Alloy.” *Metallurgical and Materials Transactions A* 43 (8): 2799–2809.

Bozek, J. E., J. D. Hochhalter, M. G. Veilleux, M. Liu, G. Heber, S. D. Sintay, A. D. Rollett, D. J. Littlewood, A. M. Maniatty, and H. Weiland, others. 2008. “A Geometric Approach to Modeling Microstructurally Small Fatigue Crack Formation: I. Probabilistic Simulation of Constituent Particle Cracking in AA 7075-T651.” *Modelling and Simulation in Materials Science and Engineering* 16 (6): 065007.

Braun, R. 2007. “Environmentally Assisted Cracking of Aluminium Alloys.” *Materialwissenschaft Und Werkstofftechnik* 38 (9): 674–89.

Bucci, R. J., C. J. Warren, and E. A. Starke. 2000. “Need for New Materials in Aging Aircraft Structures.” *Journal of Aircraft* 37 (1): 122–29.

Buffiere, J.-Y., E. Maire, J. Adrien, J.-P. Masse, and E. Boller. 2010. “*In Situ* Experiments with X Ray Tomography: An Attractive Tool for Experimental Mechanics.” *Experimental Mechanics* 50 (3): 289–305.

Burleigh, T. D. 1991. “The Postulated Mechanisms for Stress Corrosion Cracking of Aluminum Alloys: A Review of the Literature 1980-1989.” *Corrosion* 47 (2): 89–98.

Cepeda-Jiménez, C. M., J. M. García-Infanta, Oscar Antonio Ruano, and Fernando Carreño. 2011. “Mechanical Properties at Room Temperature of an Al–Zn–Mg–Cu Alloy Processed by Equal Channel Angular Pressing.” *Journal of Alloys and Compounds* 509 (35): 8649–56.

Chawla, Nikhilesh, Jason J. Williams, Xin Deng, Casey McClimon, Luke Hunter, and S. H. Lau. 2009. “Three-Dimensional Characterization and Modeling of Porosity in PM Steels.” *International Journal of Powder Metallurgy* 45 (2): 19–27.

Chawla, N., R. S. Sidhu, and V. V. Ganesh. 2006. “Three-Dimensional Visualization and Microstructure-Based Modeling of Deformation in Particle-Reinforced Composites.” *Acta Materialia* 54 (6): 1541–48.

Connolly, B. J., D. A. Horner, S. J. Fox, A. J. Davenport, C. Padovani, S. Zhou, A. Turnbull, M. Preuss, N. P. Stevens, and T. J. Marrow, others. 2006. “X-Ray Microtomography Studies of Localised Corrosion and Transitions to Stress Corrosion Cracking.” *Materials Science and Technology* 22 (9): 1076–85.

Connolly, Brain J., Kristen L. Deffenbaugh, Angela L. Moran, and Michelle G. Koul. 2003. “Environmentally Assisted Crack Growth Rates of High-Strength Aluminum Alloys.” *JOM* 55 (1): 49–52.

Davis, Joseph R. 1999. *Corrosion of Aluminum and Aluminum Alloys*. Asm International.

De Andrade Silva, Flávio, Jason J. Williams, Bernd R. Müller, Manfred P. Hentschel, Pedro D. Portella, and Nikhilesh Chawla. 2010. “Three-Dimensional Microstructure Visualization of Porosity and Fe-Rich Inclusions in SiC Particle-Reinforced Al Alloy Matrix Composites by X-Ray Synchrotron Tomography.” *Metallurgical and Materials Transactions A* 41 (8): 2121–28.

De Carlo, Francesco, and Brian Tieman. 2004. “High-Throughput X-Ray Microtomography System at the Advanced Photon Source Beamline 2-BM.” In *Optical Science and Technology, the SPIE 49th Annual Meeting*, 644–51. International Society for Optics and Photonics.

Deng, X., M. Koopman, N. Chawla, and K. K. Chawla. 2004. “Young’s Modulus of (Cu, Ag)–Sn Intermetallics Measured by Nanoindentation.” *Materials Science and Engineering: A* 364 (1): 240–43.

Deschamps, A., and Y. Brechet. 1998. “Nature and Distribution of Quench-Induced Precipitation in an Al-Zn-Mg-Cu Alloy.” *Scripta Materialia* 39 (11): 1517–22.

Dix, E. H. 1940. “Acceleration of the Rate of Corrosion by High Constant Stresses.” *AIME TRANS* 137: 11–40.

Dorward, R. C., and K. R. Hasse. 1979. “Incubation Effects in Precracked Stress Corrosion Specimens from Al-Zn-Mg-Cu Alloy 7075.” *Corrosion Science* 19 (2): 131–40.

Dowd, Betsy A., Graham H. Campbell, Robert B. Marr, Vivek V. Nagarkar, Sameer V. Tipnis, Lisa Axe, and D. Peter Siddons. 1999. “Developments in Synchrotron X-Ray Computed Microtomography at the National Synchrotron Light Source.” In *SPIE’s International Symposium on Optical Science, Engineering, and Instrumentation*, 224–36. International Society for Optics and Photonics.

Dubach, A., R. Raghavan, J. F. Löffler, J. Michler, and U. Ramamurty. 2009. “Micropillar Compression Studies on a Bulk Metallic Glass in Different Structural States.” *Scripta Materialia* 60 (7): 567–70.

Dudek, M. A., and N. Chawla. 2010. “Nanoindentation of Rare earth–Sn Intermetallics in Pb-Free Solders.” *Intermetallics* 18 (5): 1016–20.

Eckermann, Fabian, Thomas Suter, Peter J. Uggowitzer, Andreas Afseth, and Patrik Schmutz. 2008. “Investigation of the Exfoliation-like Attack Mechanism in Relation to Al–Mg–Si Alloy Microstructure.” *Corrosion Science* 50 (7): 2085–93.

Engdahl, T., V. Hansen, P. J. Warren, and K. Stiller. 2002. “Investigation of Fine Scale Precipitates in Al–Zn–Mg Alloys after Various Heat Treatments.” *Materials Science and Engineering: A* 327 (1): 59–64.

Ezuber, Hosni, A. El-Houd, and F. El-Shawesh. 2008. “A Study on the Corrosion Behavior of Aluminum Alloys in Seawater.” *Materials & Design* 29 (4): 801–5.

Fei, Huiyang, Amit Abraham, Nikhilesh Chawla, and Hanqing Jiang. 2012. “Evaluation of Micro-Pillar Compression Tests for Accurate Determination of Elastic-Plastic Constitutive Relations.” *Journal of Applied Mechanics* 79 (6): 061011.

Feng, A. H., D. L. Chen, and Z. Y. Ma. 2010. “Microstructure and Cyclic Deformation Behavior of a Friction-Stir-Welded 7075 Al Alloy.” *Metallurgical and Materials Transactions A* 41 (4): 957–71.

Fischer-Cripps, A. C. 2004. “Nanoindentation Springer.” *New York*.

Frick, C. P., B. G. Clark, S. Orso, A. S. Schneider, and E. Arzt. 2008. “Size Effect on Strength and Strain Hardening of Small-Scale [111] Nickel Compression Pillars.” *Materials Science and Engineering: A* 489 (1): 319–29.

Gao, Jie. 2011. “Experiments to Explore the Mechanisms of Stress Corrosion Cracking.” University of Rochester.

Gao, Ming, C. R. Feng, and Robert P. Wei. 1998. “An Analytical Electron Microscopy Study of Constituent Particles in Commercial 7075-T6 and 2024-T3 Alloys.” *Metallurgical and Materials Transactions A* 29 (4): 1145–51.

Garcia-Garcia, Adrian Luis, Ivan Dominguez-Lopez, Luis Lopez-Jimenez, and JD Oscar Barceinas-Sanchez. 2014. “Comparative Quantification and Statistical Analysis of H′ and H Precipitates in Aluminum Alloy AA7075-T651 by TEM and AFM.” *Materials Characterization* 87: 116–24.

Ghassemi-Armaki, Hassan, Peng Chen, Shrikant Bhat, Sriram Sadagopan, Sharvan Kumar, and Allan Bower. 2013. “Microscale-Calibrated Modeling of the Deformation Response of Low-Carbon Martensite.” *Acta Materialia* 61 (10): 3640–52.

Ghassemi-Armaki, H., R. Maa\s s, S. P. Bhat, S. Sriram, J. R. Greer, and K. S. Kumar. 2014. “Deformation Response of Ferrite and Martensite in a Dual-Phase Steel.” *Acta Materialia* 62: 197–211.

Ghosh, Sukanta. 2008. “Effect of Stress on Initiation and Propagation of Localized Corrosion in Alumninium Alloys.” University of Birmingham.

Gjønnes, J., and CHR J. Simensen. 1970. “An Electron Microscope Investigation of the Microstructure in an Aluminium-Zinc-Magnesium Alloy.” *Acta Metallurgica* 18 (8): 881–90.

Goswami, Ramasis, Stanley Lynch, NJ Henry Holroyd, Steven P. Knight, and Ronald L. Holtz. 2013. “Evolution of Grain Boundary Precipitates in Al 7075 upon Aging and Correlation with Stress Corrosion Cracking Behavior.” *Metallurgical and Materials Transactions A* 44 (3): 1268–78.

Greer, Julia R., and Jeff Th M. De Hosson. 2011. “Plasticity in Small-Sized Metallic Systems: Intrinsic versus Extrinsic Size Effect.” *Progress in Materials Science* 56 (6): 654–724.

Greer, Julia R., Warren C. Oliver, and William D. Nix. 2005. “Size Dependence of Mechanical Properties of Gold at the Micron Scale in the Absence of Strain Gradients.” *Acta Materialia* 53 (6): 1821–30.

Greer, Julia R., Christopher R. Weinberger, and Wei Cai. 2008. “Comparing the Strength of Fcc and Bcc Sub-Micrometer Pillars: Compression Experiments and Dislocation Dynamics Simulations.” *Materials Science and Engineering: A* 493 (1): 21–25.

Guo, En-Yu, Sudhanshu S. Singh, Hu-xiao Xie, Jason J. Williams, Tao Jing, and Nikhilesh Chawla. 2014. “Microstructure-Based Modeling of Deformation in Steels Based on Constitutive Relationships from Micropillar Compression.” *Steel Research International* 85 (6): 946–53.

Guo, En-Yu, Hu-Xiao Xie, Sudhanshu S. Singh, Antony Kirubanandham, Tao Jing, and Nikhilesh Chawla. 2014. “Mechanical Characterization of Microconstituents in a Cast Duplex Stainless Steel by Micropillar Compression.” *Materials Science and Engineering: A* 598: 98–105.

Gupta, R. K., N. L. Sukiman, K. M. Fleming, M. A. Gibson, and Nick Birbilis. 2012. “Electrochemical Behavior and Localized Corrosion Associated with Mg_2Si Particles in Al and Mg Alloys.” *ECS Electrochemistry Letters* 1 (1): C1–3.

Gupta, Vipul K., and Sean R. Agnew. 2011. “Fatigue Crack Surface Crystallography near Crack Initiating Particle Clusters in Precipitation Hardened Legacy and Modern Al–Zn–Mg–Cu Alloys.” *International Journal of Fatigue* 33 (9): 1159–74.

Gürbüz, R., and S. P. Alpay. 1994. “The Effect of Coarse Second Phase Particles on Fatigue Crack Propagation of an Al□ Zn□ Mg□ Cu Alloy.” *Scripta Metallurgica et Materialia* 30 (11): 1373–76.

Gu, R., and A. H. W. Ngan. 2013. “Size Effect on the Deformation Behavior of Duralumin Micropillars.” *Scripta Materialia* 68 (11): 861–64.

Hänninen, H. E. 2003. “Stress Corrosion Cracking.” *Comprehensive Structural Integrity* 6: 1–29.

Harlow, D. G., J. Nardiello, and J. Payne. 2010. “The Effect of Constituent Particles in Aluminum Alloys on Fatigue Damage Evolution: Statistical Observations.” *International Journal of Fatigue* 32 (3): 505–11.

Harris, James Joel. 2005. “Particle Cracking Damage Evolution in 7075 Wrought Aluminum Alloy under Monotonic and Cyclic Loading Conditions.” https://smartech.gatech.edu/handle/1853/7534.

Hassan, Refat M., and Ishaq A. Zaafarany. 2013. “Kinetics of Corrosion Inhibition of Aluminum in Acidic Media by Water-Soluble Natural Polymeric Pectates as Anionic Polyelectrolyte Inhibitors.” *Materials* 6 (6): 2436–51.

Hay, J. 2009. “Introduction to Instrumented Indentation Testing.” *Experimental Techniques* 33 (6): 66–72.

Hay, J., P. Agee, and E. Herbert. 2010. “Continuous Stiffness Measurement during Instrumented Indentation Testing.” *Experimental Techniques* 34 (3): 86–94.

Holroyd, NJ Henry, and G. M. Scamans. 2011. “Crack Propagation during Sustained-Load Cracking of Al-Zn-Mg-Cu Aluminum Alloys Exposed to Moist Air or Distilled Water.” *Metallurgical and Materials Transactions A* 42 (13): 3979–98.

Holzapfel, C., W. Schäf, M. Marx, H. Vehoff, and F. Mücklich. 2007. “Interaction of Cracks with Precipitates and Grain Boundaries: Understanding Crack Growth

Mechanisms through Focused Ion Beam Tomography." *Scripta Materialia* 56 (8): 697–700.

Horner, D. A., B. J. Connolly, S. Zhou, L. Crocker, and A. Turnbull. 2011. "Novel Images of the Evolution of Stress Corrosion Cracks from Corrosion Pits." *Corrosion Science* 53 (11): 3466–85.

Howie, Philip R., Sandra Korte, and William J. Clegg. 2012. "Fracture Modes in Micropillar Compression of Brittle Crystals." *Journal of Materials Research* 27 (01): 141–51.

Hruby, Peter, Sudhanshu S. Singh, Jason J. Williams, Xianghui Xiao, Francesco De Carlo, and Nikhilesh Chawla. 2014. "Fatigue Crack Growth in SiC Particle Reinforced Al Alloy Matrix Composites at High and Low R-Ratios by *In Situ* X-Ray Synchrotron Tomography." *International Journal of Fatigue* 68: 136–43.

Hütsch, Julia, and Erica T. Lilleodden. 2014. "The Influence of Focused-Ion Beam Preparation Technique on Microcompression Investigations: Lathe vs. Annular Milling." *Scripta Materialia* 77: 49–51.

J.C. Grosskreutz, G.G. Shaw. 1969. "Critical Mechanisms in the Development of Fatigue Cracks in Aluminium 2024." In *Proceedings of the Second International Conference on Fracture*, 620–29. Chapman and Hall Ltd.

Jiang, L., and N. Chawla. 2010. "Mechanical Properties of Cu 6 Sn 5 Intermetallic by Micropillar Compression Testing." *Scripta Materialia* 63 (5): 480–83.

Jiang, Ling, Nikhilesh Chawla, Mario Pacheco, and Vladimir Noveski. 2011. "Three-Dimensional (3D) Microstructural Characterization and Quantification of Reflow Porosity in Sn-Rich Alloy/copper Joints by X-Ray Tomography." *Materials Characterization* 62 (10): 970–75.

Jiang, Ling, Hanqing Jiang, and Nikhilesh Chawla. 2012. "The Effect of Crystallographic Orientation on the Mechanical Behavior of Cu6Sn5 by Micropillar Compression Testing." *Journal of Electronic Materials* 41 (8): 2083–88.

Joshi, A., C. R. Shastry, and M. Levy. 1981. "Effect of Heat Treatment on Solute Concentration at Grain Boundaries in 7075 Aluminum Alloy." *Metallurgical Transactions A* 12 (6): 1081–88.

Kastner, Johann, Bernhard Harrer, and H. Peter Degischer. 2011. "High Resolution Cone Beam X-Ray Computed Tomography of 3D-Microstructures of Cast Al-Alloys." *Materials Characterization* 62 (1): 99–107.

Keddam, M., C. Kuntz, H. Takenouti, D. Schustert, and D. Zuili. 1997. "Exfoliation Corrosion of Aluminium Alloys Examined by Electrode Impedance." *Electrochimica Acta* 42 (1): 87–97.

Kiener, Daniel, Christian Motz, and Gerhard Dehm. 2009. “Micro-Compression Testing: A Critical Discussion of Experimental Constraints.” *Materials Science and Engineering: A* 505 (1): 79–87.

King, A., W. Ludwig, D. Engelberg, and T. J. Marrow. 2011. “Diffraction Contrast Tomography for the Study of Polycrystalline Stainless Steel Microstructures and Stress Corrosion Cracking.” *Revue de Métallurgie* 108 (01): 47–50.

King, A., Wolfgang Ludwig, Michael Herbig, J.-Y. Buffière, A. A. Khan, N. Stevens, and T. J. Marrow. 2011. “Three-Dimensional *In Situ* Observations of Short Fatigue Crack Growth in Magnesium.” *Acta Materialia* 59 (17): 6761–71.

Knight, S. P., M. Salagaras, and A. R. Trueman. 2011. “The Study of Intergranular Corrosion in Aircraft Aluminium Alloys Using X-Ray Tomography.” *Corrosion Science* 53 (2): 727–34.

Knight, S. P., M. Salagaras, A. M. Wythe, F. De Carlo, A. J. Davenport, and A. R. Trueman. 2010. “*In Situ* X-Ray Tomography of Intergranular Corrosion of 2024 and 7050 Aluminium Alloys.” *Corrosion Science* 52 (12): 3855–60.

Korte, S., and W. J. Clegg. 2011. “Discussion of the Dependence of the Effect of Size on the Yield Stress in Hard Materials Studied by Microcompression of MgO.” *Philosophical Magazine* 91 (7-9): 1150–62.

Kumar, GB Veeresh, C. S. P. Rao, and N. Selvaraj. 2011. “Mechanical and Dry Sliding Wear Behaviour of Al7075 Alloy-Reinforced with SiC Particles.” *Journal of Composite Materials*, 0021998311414948.

Laplanche, G., J. Bonneville, A. Joulain, V. Gauthier-Brunet, and S. Dubois. 2014. “Mechanical Properties of Al–Cu–Fe Quasicrystalline and Crystalline Phases: An Analogy.” *Intermetallics* 50: 54–58.

L. Guillaume. 2011. “Synthesis and Characterization of Ω-Phase and Composite Al_7Cu_2Fe Al / Fe-Al-Cu.” University of Poitiers.

Li, Jin-Feng, Zhuo-wei Peng, Chao-Xing Li, Zhi-Qiang Jia, Wen-jing Chen, and Zi-Qiao Zheng. 2008. “Mechanical Properties, Corrosion Behaviors and Microstructures of 7075 Aluminium Alloy with Various Aging Treatments.” *Transactions of Nonferrous Metals Society of China* 18 (4): 755–62.

Linardi, E., R. Haddad, and L. Lanzani. 2012. “Stability Analysis of the Mg_2Si Phase in AA 6061 Aluminum Alloy.” *Procedia Materials Science* 1: 550–57.

Liu, M. C., J. C. Huang, K. W. Chen, J. F. Lin, W. D. Li, Y. F. Gao, and T. G. Nieh. 2012. “Is the Compression of Tapered Micro-and Nanopillar Samples a Legitimate Technique for the Identification of Deformation Mode Change in Metallic Glasses?” *Scripta Materialia* 66 (10): 817–20.

Liu, Xiaodong, G. S. Frankel, B. Zoofan, and S. I. Rokhlin. 2006. “Transition from Intergranular Corrosion to Intergranular Stress Corrosion Cracking in AA2024-T3.” *Journal of The Electrochemical Society* 153 (2): B42–51.

Li, Xiaodong, and Bharat Bhushan. 2002. “A Review of Nanoindentation Continuous Stiffness Measurement Technique and Its Applications.” *Materials Characterization* 48 (1): 11–36.

Li, X. Z., V. Hansen, J. Gjønnes, and L. R. Wallenberg. 1999. “HREM Study and Structure Modeling of the H′ Phase, the Hardening Precipitates in Commercial Al–Zn–Mg Alloys.” *Acta Materialia* 47 (9): 2651–59.

Ludwig, W., Jean-Yves Buffière, Stéphane Savelli, and P. Cloetens. 2003. “Study of the Interaction of a Short Fatigue Crack with Grain Boundaries in a Cast Al Alloy Using X-Ray Microtomography.” *Acta Materialia* 51 (3): 585–98.

Lugo, Marcos, J. B. Jordon, M. F. Horstemeyer, M. A. Tschopp, J. Harris, and A. M. Gokhale. 2011. “Quantification of Damage Evolution in a 7075 Aluminum Alloy Using an Acoustic Emission Technique.” *Materials Science and Engineering: A* 528 (22): 6708–14.

Lynch, S. P. 1988. “Environmentally Assisted Cracking: Overview of Evidence for an Adsorption-Induced Localised-Slip Process.” *Acta Metallurgica* 36 (10): 2639–61.

Lynch, S. P. 2013. “Mechanisms and Kinetics of Environmentally Assisted Cracking: Current Status, Issues, and Suggestions for Further Work.” *Metallurgical and Materials Transactions A* 44 (3): 1209–29.

Maire, E., L. Babout, J.-Y. Buffiere, and R. Fougeres. 2001. “Recent Results on 3D Characterisation of Microstructure and Damage of Metal Matrix Composites and a Metallic Foam Using X-Ray Tomography.” *Materials Science and Engineering: A* 319: 216–19.

Maire, Eric, Jean-Yves Buffiere, Luc Salvo, Jean Jacques Blandin, Wolfgang Ludwig, and J. M. Letang. 2001. “On the Application of X-Ray Microtomography in the Field of Materials Science.” *Advanced Engineering Materials* 3 (8): 539–46.

Maire, Eric, Jean-Christophe Grenier, D. Daniel, A. Baldacci, H. Klöcker, and A. Bigot. 2006. “Quantitative 3D Characterization of Intermetallic Phases in an Al–Mg Industrial Alloy by X-Ray Microtomography.” *Scripta Materialia* 55 (2): 123–26.

Maire, Eric, Suxia Zhou, Jerome Adrien, and Marco Dimichiel. 2011. “Damage Quantification in Aluminium Alloys Using *In Situ* Tensile Tests in X-Ray Tomography.” *Engineering Fracture Mechanics* 78 (15): 2679–90.

Maire, E., and P. J. Withers. 2014. “Quantitative X-Ray Tomography.” *International Materials Reviews* 59 (1): 1–43.

Marlaud, T., A. Deschamps, F. Bley, W. Lefebvre, and B. Baroux. 2010. “Influence of Alloy Composition and Heat Treatment on Precipitate Composition in Al–Zn–Mg–Cu Alloys.” *Acta Materialia* 58 (1): 248–60.

Marlaud, T., B. Malki, C. Henon, A. Deschamps, and B. Baroux. 2011. “Relationship between Alloy Composition, Microstructure and Exfoliation Corrosion in Al–Zn–Mg–Cu Alloys.” *Corrosion Science* 53 (10): 3139–49.

Marone, F., and M. Stampanoni. 2012. “Regridding Reconstruction Algorithm for Real-Time Tomographic Imaging.” *Journal of Synchrotron Radiation* 19 (6): 1029–37.

Marrow, T. J., L. Babout, B. J. Connolly, D. Engelberg, G. Johnson, J. Y. Buffiere, P. J. Withers, and R. C. Newman. 2004. “High-Resolution, *In-Situ*, Tomographic Observations of Stress Corrosion Cracking.” *EICM 2, Prediction, Industrial Developments and Evaluation*.

Marrow, T. J., L. Babout, A. P. Jivkov, Paul Wood, Dirk Engelberg, Nicholas Stevens, Philip J. Withers, and R. C. Newman. 2006. “Three Dimensional Observations and Modelling of Intergranular Stress Corrosion Cracking in Austenitic Stainless Steel.” *Journal of Nuclear Materials* 352 (1): 62–74.

Masuda, Hiroyuki. 2007. “SKFM Observation of SCC on SUS304 Stainless Steel.” *Corrosion Science* 49 (1): 120–29.

McNaughtan, D., M. Worsfold, and M. J. Robinson. 2003. “Corrosion Product Force Measurements in the Study of Exfoliation and Stress Corrosion Cracking in High Strength Aluminium Alloys.” *Corrosion Science* 45 (10): 2377–89.

Merkel, Arno, Lorenz Lechner, Andy Steinbach, Jeff Gelb, Martin Kienle, Michael W. Phaneuf, David Unrau, Sudhanshu S. Singh, and Nikhilesh Chawla. 2014. “Automated Correlative Tomography Using Xrm and FIB-SEM to Span Length Scales and Modalities in 3D Materials” 28: S10–13.

Michler, Johann, Kilian Wasmer, Stephan Meier, Fredrik Ostlund, and Klaus Leifer. 2007. “Plastic Deformation of Gallium Arsenide Micropillars under Uniaxial Compression at Room Temperature.” *Applied Physics Letters* 90 (4): 043123–043123.

Midgley, Paul A., and Rafal E. Dunin-Borkowski. 2009. “Electron Tomography and Holography in Materials Science.” *Nature Materials* 8 (4): 271–80.

Miller, M. K., and E. A. Kenik. 2004. “Atom Probe Tomography: A Technique for Nanoscale Characterization.” *Microscopy and Microanalysis* 10 (03): 336–41.

Mills, Thomas Brian. 1997. *The Combined Effects of Prior-Corrosion and Aggressive Chemical Environments on Fatigue Crack Growth Behavior in Aluminum Alloy 7075-T651*.

M. Meyers, K. K. Chawla. 2008. *Mechanical Behavior of Materials*. Second. Cambridge University Press.

Moulin, Nicolas, Estelle Parra-Denis, Dominique Jeulin, Christophe Ducottet, Annabelle Bigot, Elodie Boller, Éric Maire, Cecile Barat, and Helmut Klöcker. 2010. "Constituent Particle Break-Up During Hot Rolling of AA 5182." *Advanced Engineering Materials* 12 (1-2): 20–29.

Muñoz-Palos, Jose Manuel, M. a del Carmen Cristina, and Paloma Adeva. 1996. "Synthesis of Mg 2 Si Powder by Mechanical Alloying and Its Consolidation." *Materials Transactions, JIM* 37 (10): 1602–6.

Okamoto, Norihiko L., Masahiro Inomoto, Hiroki Adachi, Hiroshi Takebayashi, and Haruyuki Inui. 2014. "Micropillar Compression Deformation of Single Crystals of the Intermetallic Compound Z-FeZn 13." *Acta Materialia* 65: 229–39.

Okamoto, Norihiko L., Daisuke Kashioka, Masahiro Inomoto, Haruyuki Inui, Hiroshi Takebayashi, and Shu Yamaguchi. 2013. "Compression Deformability of Γ and Z Fe–Zn Intermetallics to Mitigate Detachment of Brittle Intermetallic Coating of Galvannealed Steels." *Scripta Materialia* 69 (4): 307–10.

Oliver, Warren Carl, and George Mathews Pharr. 1992. "An Improved Technique for Determining Hardness and Elastic Modulus Using Load and Displacement Sensing Indentation Experiments." *Journal of Materials Research* 7 (06): 1564–83.

Oliver, Warren C., and Georges M. Pharr. 2004. "Measurement of Hardness and Elastic Modulus by Instrumented Indentation: Advances in Understanding and Refinements to Methodology." *Journal of Materials Research* 19 (01): 3–20.

Oriani, R. A. 1972. "A Mechanistic Theory of Hydrogen Embrittlement of Steels." *Berichte Der Bunsengesellschaft Für Physikalische Chemie* 76 (8): 848–57.

Östlund, Fredrik, Philip R. Howie, Rudy Ghisleni, Sandra Korte, Klaus Leifer, William J. Clegg, and Johann Michler. 2011. "Ductile–brittle Transition in Micropillar Compression of GaAs at Room Temperature." *Philosophical Magazine* 91 (7-9): 1190–99.

Östlund, Fredrik, Karolina Rzepiejewska-Malyska, Klaus Leifer, Lucas M. Hale, Yuye Tang, Roberto Ballarini, William W. Gerberich, and Johann Michler. 2009. "Brittle-to-Ductile Transition in Uniaxial Compression of Silicon Pillars at Room Temperature." *Advanced Functional Materials* 19 (15): 2439–44.

Oswald, L. 2003. “Effects of Microstructure on High-Cycle Fatigue of an AL-ZN-MG-CU Alloy.” *Master’s Thesis, University of Pittsburgh, PA*.

Padilla, E., V. Jakkali, L. Jiang, and N. Chawla. 2012. “Quantifying the Effect of Porosity on the Evolution of Deformation and Damage in Sn-Based Solder Joints by X-Ray Microtomography and Microstructure-Based Finite Element Modeling.” *Acta Materialia* 60 (9): 4017–26.

Pao, P. S., M. A. Imam, L. A. Cooley, and G. R. Yoder. 1989. “Comparison of Corrosion-Fatigue Cracking of Al-Li Alloy AA 2090-T8E41 and Alloy AA 7075-T651 in Salt Water.” *Corrosion* 45 (7): 530–35.

Parra-Denis, Estelle, Christophe Ducottet, and Dominique Jeulin. 2009. “A 3D Image Analysis of Intermetallic Inclusions.” *International Journal of Microstructure and Materials Properties* 4 (2): 217–30.

Patton, G., C. Rinaldi, Y. Brechet, G. Lormand, and R. Fougeres. 1998. “Study of Fatigue Damage in 7010 Aluminum Alloy.” *Materials Science and Engineering: A* 254 (1): 207–18.

Payne, Joel, Greg Welsh, Robert J. Christ, Jerrell Nardiello, and John M. Papazian. 2010. “Observations of Fatigue Crack Initiation in 7075-T651.” *International Journal of Fatigue* 32 (2): 247–55.

Pearson, S. 1975. “Initiation of Fatigue Cracks in Commercial Aluminium Alloys and the Subsequent Propagation of Very Short Cracks.” *Engineering Fracture Mechanics* 7 (2): 235–47.

Porter, David A., Kenneth E. Easterling, and Mohamed Sherif. 2009. *Phase Transformations in Metals and Alloys, (Revised Reprint)*. CRC press.

Qiao, L. J., K. W. Gao, Alex A. Volinsky, and X. Y. Li. 2011. “Discontinuous Surface Cracks during Stress Corrosion Cracking of Stainless Steel Single Crystal.” *Corrosion Science* 53 (11): 3509–14.

Richard, DeIasi, and Philip N. Adler. 1977. “Calorimetric Studies of 7000 Series Aluminum Alloys: I. Matrix Precipitate Characterization of 7075.” *Metallurgical Transactions A* 8 (7): 1177–83.

Ringer, S. P., and K. Hono. 2000. “Microstructural Evolution and Age Hardening in Aluminium Alloys: Atom Probe Field-Ion Microscopy and Transmission Electron Microscopy Studies.” *Materials Characterization* 44 (1): 101–31.

Rivers, Mark L. 2012. “tomoRecon: High-Speed Tomography Reconstruction on Workstations Using Multi-Threading.” In *SPIE Optical Engineering+ Applications*, 85060U – 85060U. International Society for Optics and Photonics.

Robertson, I. M. 2001. “The Effect of Hydrogen on Dislocation Dynamics.” *Engineering Fracture Mechanics* 68 (6): 671–92.

Robinson, M. J., and N. C. Jackson. 1999. “The Influence of Grain Structure and Intergranularcorrosion Rate on Exfoliation and Stress Corrosion Crackingof High Strength Al–Cu–Mg Alloys.” *Corrosion Science* 41 (5): 1013–28.

Rollett, Anthony D., Robert Campman, and David Saylor. 2006. “Three Dimensional Microstructures: Statistical Analysis of Second Phase Particles in AA7075-T651.” In *Materials Science Forum*, 519:1–10. Trans Tech Publ.

Root, Jameson Martin Moore. 2010. “Structure Evolution and Recrystallization in 7XXX Series Aluminum Alloys.” Washington State University.

Salvo, L., P. Cloetens, Eric Maire, S. Zabler, J. J. Blandin, Jean-Yves Buffière, W. Ludwig, E. Boller, D. Bellet, and C. Josserond. 2003. “X-Ray Micro-Tomography an Attractive Characterisation Technique in Materials Science.” *Nuclear Instruments and Methods in Physics Research Section B: Beam Interactions with Materials and Atoms* 200: 273–86.

Shan, Z. W., Raja K. Mishra, SA Syed Asif, Oden L. Warren, and Andrew M. Minor. 2008. “Mechanical Annealing and Source-Limited Deformation in Submicrometre-Diameter Ni Crystals.” *Nature Materials* 7 (2): 115–19.

Shin, Chansun, Hyung-Ha Jin, Weon-Ju Kim, and Ji-Yeon Park. 2012. “Mechanical Properties and Deformation of Cubic Silicon Carbide Micropillars in Compression at Room Temperature.” *Journal of the American Ceramic Society* 95 (9): 2944–50.

Shi, Zhiming, Ming Liu, and Andrej Atrens. 2010. “Measurement of the Corrosion Rate of Magnesium Alloys Using Tafel Extrapolation.” *Corrosion Science* 52 (2): 579–88.

Sidhu, R. S., and N. Chawla. 2004. “Three-Dimensional Microstructure Characterization of Ag 3 Sn Intermetallics in Sn-Rich Solder by Serial Sectioning.” *Materials Characterization* 52 (3): 225–30.

Sidhu, R. S., and N. Chawla. 2006. “Three-Dimensional (3D) Visualization and Microstructure-Based Modeling of Deformation in a Sn-Rich Solder.” *Scripta Materialia* 54 (9): 1627–31.

Singh, D. R. P., N. Chawla, and Y.-L. Shen. 2010. “Focused Ion Beam (FIB) Tomography of Nanoindentation Damage in Nanoscale Metal/ceramic Multilayers.” *Materials Characterization* 61 (4): 481–88.

Soler, R., Jon M. Molina-Aldareguia, J. Segurado, J. Llorca, R. I. Merino, and V. M. Orera. 2012. “Micropillar Compression of LiF [111] Single Crystals: Effect of

Size, Ion Irradiation and Misorientation." *International Journal of Plasticity* 36: 50–63.

Speidel, Markus O. 1975. "Stress Corrosion Cracking of Aluminum Alloys." *Metallurgical Transactions A* 6 (4): 631–51.

Starke, E. A., and J. T. Staley. 1996. "Application of Modern Aluminum Alloys to Aircraft." *Progress in Aerospace Sciences* 32 (2): 131–72.

Stewart, J. L., L. Jiang, J. J. Williams, and N. Chawla. 2012. "Prediction of Bulk Tensile Behavior of Dual Phase Stainless Steels Using Constituent Behavior from Micropillar Compression Experiments." *Materials Science and Engineering: A* 534: 220–27.

Stiller, Krystyna, P. J. Warren, Vidar Hansen, Johan Angenete, and J. Gjønnes. 1999. "Investigation of Precipitation in an Al–Zn–Mg Alloy after Two-Step Ageing Treatment at 100 and 150 C." *Materials Science and Engineering: A* 270 (1): 55–63.

Stock, S. R. 1999. "X-Ray Microtomography of Materials." *International Materials Reviews* 44 (4): 141–64.

Sun, X. Y., B. Zhang, H. Q. Lin, Y. Zhou, L. Sun, J. Q. Wang, E.-H. Han, and W. Ke. 2013. "Correlations between Stress Corrosion Cracking Susceptibility and Grain Boundary Microstructures for an Al–Zn–Mg Alloy." *Corrosion Science* 77: 103–12.

Suresh, Subra. 1998. *Fatigue of Materials*. Cambridge university press.

Takeuchi, S., T. Hashimoto, and K. Suzuki. 1996. "Plastic Deformation of Mg2Si with the C1 Structure." *Intermetallics* 4: S147–50.

Terzi, S., L. Salvo, M. Suéry, N. Limodin, J. Adrien, E. Maire, Y. Pannier, M. Bornert, Dominique Bernard, and M. Felberbaum, others. 2009. "*In Situ* X-Ray Tomography Observation of Inhomogeneous Deformation in Semi-Solid Aluminium Alloys." *Scripta Materialia* 61 (5): 449–52.

Toda, H., S. Yamamoto, M. Kobayashi, K. Uesugi, and H. Zhang. 2008. "Direct Measurement Procedure for Three-Dimensional Local Crack Driving Force Using Synchrotron X-Ray Microtomography." *Acta Materialia* 56 (20): 6027–39.

Totten, G. E., and Scott MacKenzie. 2003. *D. Handbook of Aluminum: Alloy Production and Materials Manufacturing*. Dekker: New York, NY, USA.

Uchic, Michael D., Dennis M. Dimiduk, Jeffrey N. Florando, and William D. Nix. 2004. "Sample Dimensions Influence Strength and Crystal Plasticity." *Science* 305 (5686): 986–89.

Uchic, Michael D., Michael A. Groeber, Dennis M. Dimiduk, and J. P. Simmons. 2006. "3D Microstructural Characterization of Nickel Superalloys via Serial-Sectioning Using a Dual Beam FIB-SEM." *Scripta Materialia* 55 (1): 23–28.

Uchic, Michael D., Paul A. Shade, and Dennis M. Dimiduk. 2009a. "Micro-Compression Testing of Fcc Metals: A Selected Overview of Experiments and Simulations." *JOM* 61 (3): 36–41.

Uchic, Michael D., Paul A. Shade, and Dennis M. Dimiduk. 2009b. "Plasticity of Micrometer-Scale Single Crystals in Compression." *Annual Review of Materials Research* 39: 361–86.

Uvaraja, V. C., and N. Natarajan. 2012. *Comparison on Al6061 and Al7075 Alloy with Sic and B4C Reinforcement Hybrid Metal Matrix Composites*. IJART.

Vargel, Christian. 2004. *Corrosion of Aluminium*. Elsevier.

Viana, Filomena, A. M. P. Pinto, H. M. C. Santos, and A. B. Lopes. 1999. "Retrogression and Re-Ageing of 7075 Aluminium Alloy: Microstructural Characterization." *Journal of Materials Processing Technology* 92: 54–59.

V.S. Zolotorevsky, N.A. Belov, M.V. Glazoff,. 2007. *Casting Aluminum Alloys*. 1st ed. Elsevier Ltd.

Wang, L., X. Y. Qin, W. Xiong, and X. G. Zhu. 2007. "Fabrication and Mechanical Properties of Bulk Nanocrystalline Intermetallic Mg 2 Si." *Materials Science and Engineering: A* 459 (1): 216–22.

Weiland, H., J. Nardiello, S. Zaefferer, S. Cheong, J. Papazian, and Dierk Raabe. 2009. "Microstructural Aspects of Crack Nucleation during Cyclic Loading of AA7075-T651." *Engineering Fracture Mechanics* 76 (5): 709–14.

Werenskiold, J. C., A. Deschamps, and Y. Bréchet. 2000. "Characterization and Modeling of Precipitation Kinetics in an Al–Zn–Mg Alloy." *Materials Science and Engineering: A* 293 (1): 267–74.

Williams, Jason J., Kyle E. Yazzie, N. Connor Phillips, Nikhilesh Chawla, Xinghui Xiao, Francesco De Carlo, Nagaraja Iyyer, and Maddan Kittur. 2011. "On the Correlation between Fatigue Striation Spacing and Crack Growth Rate: A Three-Dimensional (3-D) X-Ray Synchrotron Tomography Study." *Metallurgical and Materials Transactions A* 42 (13): 3845–48.

Williams, J. J., N. C. Chapman, V. Jakkali, V. A. Tanna, N. Chawla, X. Xiao, and F. De Carlo. 2011. "Characterization of Damage Evolution in SiC Particle Reinforced Al Alloy Matrix Composites by *In-Situ* X-Ray Synchrotron Tomography." *Metallurgical and Materials Transactions A* 42 (10): 2999–3005.

Williams, J. J., Z. Flom, A. A. Amell, N. Chawla, X. Xiao, and F. De Carlo. 2010. "Damage Evolution in SiC Particle Reinforced Al Alloy Matrix Composites by X-Ray Synchrotron Tomography." *Acta Materialia* 58 (18): 6194–6205.

Williams, J. J., J. L. Walters, M. Y. Wang, N. Chawla, and Aashish Rohatgi. 2013. "Extracting Constitutive Stress–Strain Behavior of Microscopic Phases by Micropillar Compression." *JOM* 65 (2): 226–33.

Williams, J. J., K. E. Yazzie, E. Padilla, N. Chawla, X. Xiao, and F. De Carlo. 2013. "Understanding Fatigue Crack Growth in Aluminum Alloys by *In Situ* X-Ray Synchrotron Tomography." *International Journal of Fatigue* 57: 79–85.

Wloka, Joachim, Gotthold Bürklin, and Sannakaisa Virtanen. 2007. "Influence of Second Phase Particles on Initial Electrochemical Properties of AA7010-T76." *Electrochimica Acta* 53 (4): 2055–59.

Xie, H. X., and N. Chawla. 2013. "Enhancing the Ductility of Sn-Ag-Cu Lead-Free Solder Joints by Addition of Compliant Intermetallics." *Journal of Electronic Materials* 42 (3): 527–36.

Xiong, Wei, Xiaoying Qin, and Li Wang. 2007. "Densification Behavior of Nanocrystalline Mg_2Si Compact in Hot-Pressing." *Journal of Materials Science & Technology* 23 (5): 595–98.

Xue, Y., H. El Kadiri, M. F. Horstemeyer, J. B. Jordon, and H. Weiland. 2007. "Micromechanisms of Multistage Fatigue Crack Growth in a High-Strength Aluminum Alloy." *Acta Materialia* 55 (6): 1975–84.

Yazzie, K. E., J. J. Williams, N. C. Phillips, F. De Carlo, and N. Chawla. 2012. "Multiscale Microstructural Characterization of Sn-Rich Alloys by Three Dimensional (3D) X-Ray Synchrotron Tomography and Focused Ion Beam (FIB) Tomography." *Materials Characterization* 70: 33–41.

Yue, T. M., L. J. Yan, C. F. Dong, and C. P. Chan. 2005. "Stress Corrosion Cracking Behaviour of Laser Treated Aluminium Alloy 7075 Using a Slow Strain Rate Test." *Materials Science and Technology* 21 (8): 961–66.

ZENG, Feng-li, Zhong-ling WEI, Jin-feng LI, Chao-xing LI, T. A. N. Xing, Zhao ZHANG, and Zi-qiao ZHENG. 2011. "Corrosion Mechanism Associated with Mg 2 Si and Si Particles in Al–Mg–Si Alloys." *Transactions of Nonferrous Metals Society of China* 21 (12): 2559–67.

Zhang, Haitao, Brian E. Schuster, Qiuming Wei, and Kaliat T. Ramesh. 2006. "The Design of Accurate Micro-Compression Experiments." *Scripta Materialia* 54 (2): 181–86.

Zhang, H., H. Toda, P. C. Qu, Y. Sakaguchi, M. Kobayashi, K. Uesugi, and Y. Suzuki. 2009. “Three-Dimensional Fatigue Crack Growth Behavior in an Aluminum Alloy Investigated with *In Situ* High-Resolution Synchrotron X-Ray Microtomography.” *Acta Materialia* 57 (11): 3287–3300.

Zhang, Jixi, Sergiy Kalnaus, Majid Behrooz, and Yanyao Jiang. 2011. “Effect of Loading History on Stress Corrosion Cracking of 7075-T651 Aluminum Alloy in Saline Aqueous Environment.” *Metallurgical and Materials Transactions A* 42 (2): 448–60.

Zhang, P., S. X. Li, and Z. F. Zhang. 2011. “General Relationship between Strength and Hardness.” *Materials Science and Engineering: A* 529: 62–73.

Zhao, Y. H., X. Z. Liao, Z. Jin, R. Z. Valiev, and Y. T. Zhu. 2004. “Microstructures and Mechanical Properties of Ultrafine Grained 7075 Al Alloy Processed by ECAP and Their Evolutions during Annealing.” *Acta Materialia* 52 (15): 4589–99.